POLITECNICO DI MILANO
Dipartimento di fisica

Study of primary mechanisms of Photosynthesis in green algae by Ultrafast Vis-NIR spectroscopy

PhD candidate:
Gabriel José de la Cruz Valbuena

Supervisor: Dr. Cosimo D'Andrea
Tutor: Prof. Paola Taroni

Academic year 2019/2020 - Cycle XXXII

Contents

List of Figures

List of Tables

Chapter 1

Introduction

Chapter 1 is dedicated to do a general overview on the biophysical aspects related to photosynthesis. In section 1.1, I expose the purpose of this thesis. In section 1.2, I focus on the photosynthesis process itself. Pigments and photosystems involved in photosynthesis are explained in sections 1.3 and 1.4, respectively. Photoinhibition and photoprotection mechanisms are shown in section 1.5 while a description of the protein involved in a certain photoprotection mechanism is found in section 1.6. Finally, section 1.7 consists in a description of the different spectroscopic techniques we will use in following chapters.

1.1 Motivation

Two of the most important problems humanity has to face nowadays are the global energetic crisis and climate change. To deal with both issues, the development of green and sustainable energies that replace the use of fossil fuels sources has increased exponentially since the 70s. More specifically, solar energy importance has grown considerably due to the fact that it is the most abundant renewable energy source in our planet.

Throughout Earth's history, a wide range of organisms have been able to transform solar energy into biomass through photosynthesis, making photosynthesis the main solar energy conversion process happening on our planet. In fact, photosynthetic organisms such as plants and algae can constitute an energy source as they can be used for biomass production or even for biofuel production, in particular bio-diesel, bio-hydrogen and bio-ethanol. In addition, these organisms are interesting as a source of high value products such as antioxidants or oil.

Among these organisms, algae show more photosynthetic efficiency than plants, due to the fact that algae can use their whole surface to collect light as opposed to plants, in which not all the surface is used for light collection, i.e, the roots. Additionally, algae have more advantages than plants: (i) they can be fed with industrial fumes and wastewater, (ii) algae do not compete with crops as they can be grown in sea water and (iii) their waste after burning can be used for animal feeding, biofuel production via fermentation or it can be recycled to feed more algae. Also, their oil content (which can

be used for biofuel production) varies from 30-80%, depending on the strain and growing conditions.

Despite its theoretical profitability, algae are not very efficient from an industrial point of view. Theoretical estimations predict a 8–10% of solar-to-biomass conversion efficiency and a maximum productivity of 77 g biomass m^{-2} day^{-1} (or equivalently, 280 ton ha^{-1} $year^{-1}$).[1] Nevertheless, experiments performed in a laboratory revealed a 3% of solar-to-biomass conversion efficiency in the best-case scenario[2,3] with a maximum productivity of around 40% of the theoretical value.[4–7]

The difference between the theoretical and the real efficiency values points out a problem to exploit algae to their maximum potential. Nowadays, the most efficient way to cultivate algae consists in using photobioreactors[8] although there are some drawbacks in their use. Some minor problems are based in the algae culture itself, as the nutrient availability is limited and some algae can produce toxins to avoid cell culture overgrowth. However, the main problem of photobioreactors is the lower light use efficiency value in comparison with the theoretical value.

This low light use efficiency can be associated with a combined effect of uneven light distribution along the photobioreactor and a suboptimal photosynthetic process. In fact, several authors have proposed models to optimize the light distribution within the photobioreactors.[8–10] Regarding the photosynthetic aspect, thermal dissipation constitutes the main cause of light absorption inefficiency as it can represent 80% of light losses in a process called non-photochemical quenching (NPQ).[11]

The main purpose of this thesis is to study and analyze from a molecular point of view the NPQ energy dissipation process in green algae *C. Reinhardtii* to further use biotechnological tools that allow us to increase its light absorption efficiency. For this purpose, we will use ultrafast spectroscopy tools such as time-resolved fluorescence (TRF) and transient absorption (TA).

1.2 Photosynthesis

Life on Earth is based on the chemistry of carbon. However, the vast majority of available carbon is present as an inorganic and oxidized form, being carbon dioxide gas the easiest reachable source. In nature, carbon is mainly used by living beings as an energy source or as an organic molecule building material so its reduction and fixation plays a key aspect in life development. There are some biological mechanisms to do this task but the most important pathway to achieve CO_2 reduction is photosynthesis.

Photosynthesis is a complex process which involve a large number of steps, but overall, it can be seen as a redox reaction in which CO_2 is reduced and a second generic molecule H_2A gets oxidized. The nature of the element A depends on the organism who performs photosynthesis as this process can be oxygenic or anoxygenic. In the case of study of this thesis, green algae perform oxygenic photosynthesis, so the overall reaction can be written as:

$$6CO_2 + 6H_2O \xrightarrow{\text{light}} C_6H_{12}O_6 + 6O_2 \tag{1.1}$$

this equation can be split into:

$$2H_2O + light \rightarrow 4H^+ + 4e^- + O_2 \tag{1.2}$$

$$CO_2 + 4H^+ + 4e^- \rightarrow CH_2O + H_2O \tag{1.3}$$

Equations 1.2 and 1.3 constitute the partial oxidation and reduction reactions, respectively. Nevertheless, free electrons are not normally present in biological systems, so reactions 1.2 and 1.3 requires the presence of reductive intermediates, which will be described in the following sections. In any case, this simplified model shows us two important aspects of photosynthesis: first, it is constituted by one light-dependent oxidative phase and another light-independent reductive phase and second, photosynthesis requires a series of intermediates to occur.

1.2.1 Chloroplasts

In green algae, both phases of photosynthesis take place in a cellular organelle called chloroplast.[12] Chloroplasts have an envelope composed by two lipid bilayers and an intermembrane space. The outer membrane is very permeable whereas the inner membrane is selectively permeable and only let pass certain types of metabolites.

The chloroplast interior consists in an aqueous solution known as stroma which contains enzymes associated to the Calvin cycle, in particular one related to the carbon fixation stage: ribulose-1,5-bisphosphate carboxylase/oxygenase (RuBisCO). Ribosomes, chloroplast DNA and mRNA are also found inside the chloroplast.[13] Within this solution, there is also a membrane system called thylakoid membrane. Thylakoids are small vesicles stacked together forming structures called grana which in turn are connected by another type of thylakoid membrane known as stroma lamellae. Thylakoids play a key role in photosynthesis because it is here where the light phase of photosynthesis occurs. In fact, the different proteins that form the photosynthetic apparatus are organized along

the thylakoid membrane but unevenly distributed as photosystem I (PSI) is localized principally in the stroma lamellae and photosystem II (PSII) is placed in the grana. The enclosed space within a thylakoid is called lumen. A brief scheme of all the parts of the chloroplast is shown in figure 1.1.

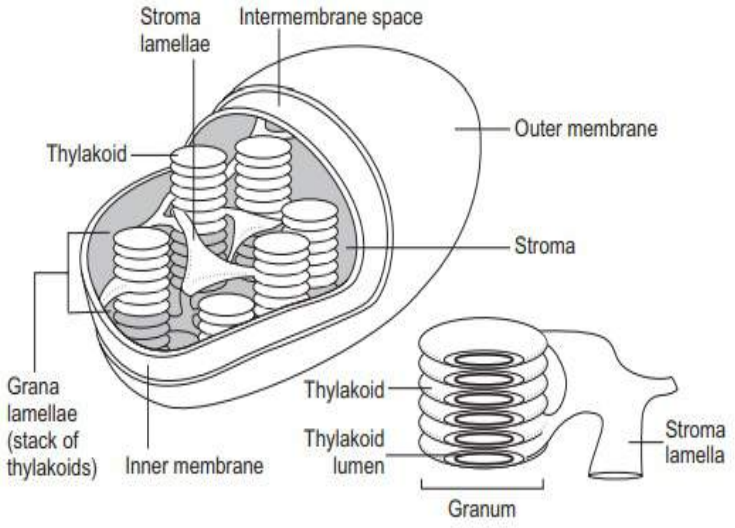

Figure 1.1: Schematic diagram of the chloroplast components. (Image from R. E. Blankenship, 2002)

1.2.2 Light phase

All proteins that participate in the light phase of photosynthesis can be grouped in four major protein complexes located in the thylakoidal membrane: Photosystem II (PSII), cytochrome b_6f, photosystem I (PSI) and ATP synthase. The main function of these complexes is to catalyze the light conversion into adenosine triphosphate (ATP) and nicotinamide adenine dinucleotide phosphate (NADPH). PSI and PSII are the responsible of the light harvesting while ATP synthase is the responsible to form ATP thanks to the proton-motive-force (*pmf*) generated in the light reactions. Moreover, cytochrome b_6f task is to ensure the electron transfer from PSII to PSI, increasing the *pmf* in the process.[14] A brief scheme of all the light phase steps can be seen in figure 1.2.

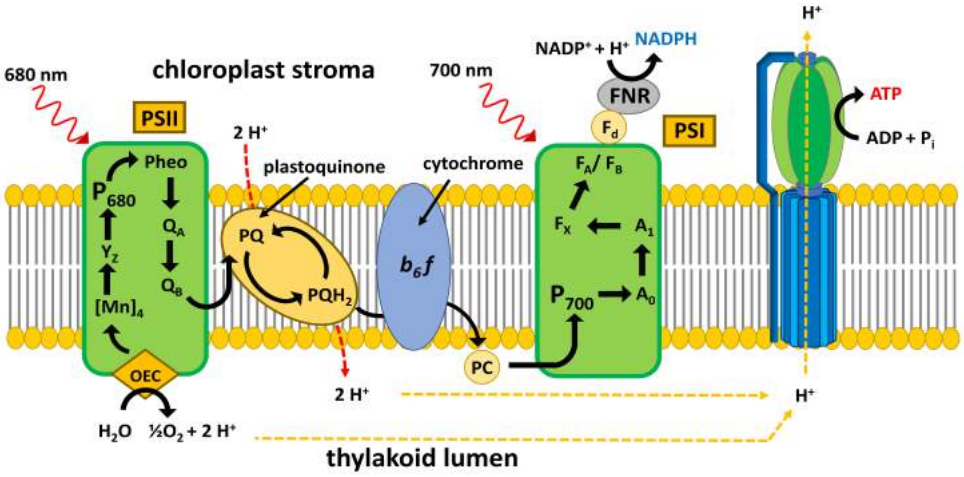

Figure 1.2: Schematic diagram of the light phase reactions.

Considering the large difference in the redox potential of the electron donor (molecular oxygen) and the electron acceptor ($NADP^+$) the energy needed to form NAPDH cannot be reached with the absorption of a single photon in the visible range so two photons are needed. Photon absorption is an extremely efficient process as quantum yields for PSI and PSII are ≈1 and 0.85, respectively. Thus, the two photons are absorbed sequentially by PSII and PSI following the so-called z-scheme.[14] Z-scheme diagram is shown in figure 1.3 with the corresponding redox potentials of each species.[15]

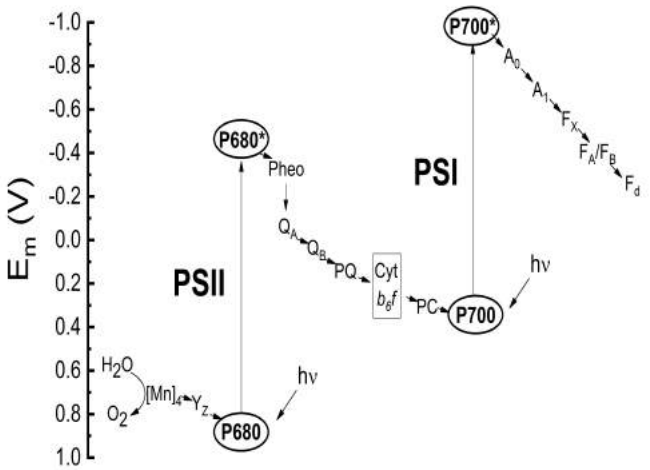

Figure 1.3: Schematic diagram of the light phase Z-scheme.

Photosynthesis starts with the absorption of one photon by a PSII special chlorophyll pair called P_{680}. The excited P_{680} undergoes charge splitting and the electron generated this way is transferred to pheophytin (Pheo), generating a Pheo anion and starting the electron transfer chain.

The electronic deficiency on $P_{680}{}^{+}$ is corrected by the oxidation of the aminoacid tyrosine, Y_Z, which get electrons in turn from the manganese cluster next to it. Finally, the manganese cluster extracts electrons from the oxidation of the lumenal water in the oxygen-evolving complex (OEC), generating oxygen and protons in the process.

The Pheo anion then interacts with the quinone pool and, in particular with Q_A. It is important to say that Q_A presence is a fundamental requirement in the success of the electron transfer chain, as it stabilizes the electron and avoid an useless recombination backreaction between the $Pheo^{-}$ and the $P_{680}{}^{+}$. Two electrons are then transferred from Q_A to the secondary mobile acceptor Q_B and generates $Q_B{}^{-2}$ who diffuses into the thylakoid membrane towards the cytochrome complex b_6f and starts the so called Q-cycle.[16] The reduced plastoquinone $Q_B{}^{-2}$ get two protons from the chloroplast stroma and then is oxidized by the cytochrome b_6 to form plastoquinol. Cytochrome b_6, in turn, is oxidized by the cytochrome f who then transfers its electron to a copper-containing protein, plastocyanine (PC). Overall, cytochrome complex b_6f oxidises two plastoquinols, reduces one plastoquinone and transports four protons into the thylakoid lumen for every two electrons captured by PC. The full Q-cycle can be expressed as:

$$PQH_2 + 2Cu^{+2}PC + 2H^{+}_{stroma} \rightleftharpoons PQ + 2Cu^{+}PC + 4H^{+}_{lumen} \tag{1.4}$$

The protons generated in the lumen during the water splitting and those liberated in the lumen after the action of the cytochrome complex b_6f create a pH gradient across the membrane and a proton-motive force (pmf) which will be used later for ATP synthesis.

Plastocyanine (PC) then transfers its electrons to PSI reaction center, P_{700}, and a second photon is absorbed. A second charge separation occurs and the electron is quickly and sequentially transferred through a series of carriers: a chlorophyll monomer, A_0, phylloquinone, A_1, an iron cluster, F_X, iron-containing proteins, F_A/F_B and finally a molecule of ferredoxin, F_d.[17,18] NADPH is thus formed from F_d after the activation of the ferredoxin-$NADP^{+}$ reductase (FNR).[18]

The electrochemical gradient formed during the light phase triggers the ATPase activation and the ATP formation in the stromal side of the chloroplast. ATPase is a complex protein system composed by transmembrane (CF_0) and stromal parts (CF_1)[19] acting as a molecular motor. CF_0 is composed by three static subunits (I, II and IV) and a rotary subunit III while CF_1 possesses also three static subunits, α, β and δ and two mobile components, γ and ϵ.

The *pmf* drives one proton from the lumen to one subunit III compartment, makes it rotate and then the proton is released in the stroma. This rotation drags CF_1 subunits γ and ϵ and provides enough energy to synthesize ATP in CF_1 β subunit.[20] A brief diagram of ATPase subunits is shown in figure 1.4.

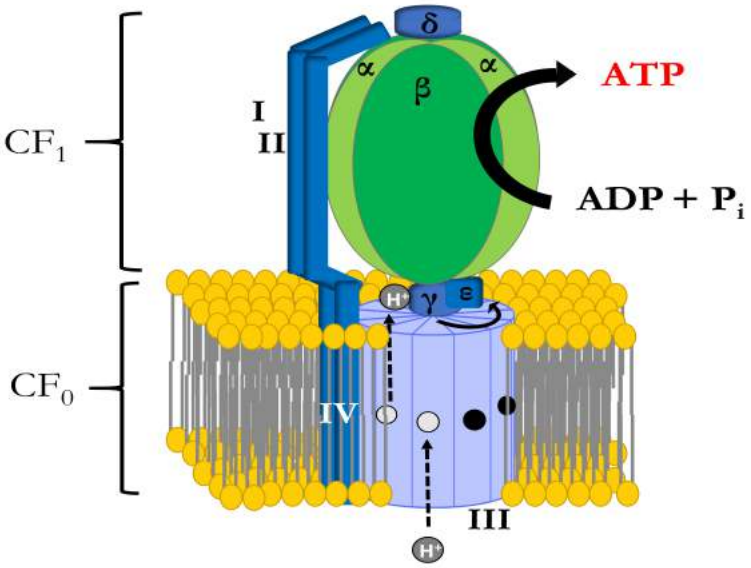

Figure 1.4: Schematic diagram of the ATPase complex protein.

In NADPH excess conditions, ATP formation can be done without molecular oxygen production in PSII through a model called cyclic electron flow.[21] In this cycle, electrons are taken from ferredoxin back to cytochrome complex b_6f and thus transferred to plastocyanin and back to P_{700}. The pH gradient formed during cytochrome complex b_6f reactions is used to activate ATPase.

1.2.3 Dark phase

Photosynthesis dark phase happens in the chloroplast stroma and consists in the formation of complex carbohydrates from CO_2 using the NADPH and ATP formed during the light phase in a series of reactions. These series of reactions are simply known as the Calvin cycle[22] and within it, the role of RuBisCO enzyme is key as it is the responsible of CO_2 fixation to a molecule of Ribulose-bisphospate (RuBP). Overall, Calvin cycle can be separated in the three stages listed below.

1. **CO_2 fixation:** CO_2 interacts with a molecule of RuBP and generates 3-phospho glyceric acid (3-PGA).

2. **PGA reduction:** 3-PGA reacts with NADPH and ATP to form glyceraldehyde 3-phosphate (GAP), a precursor of glucose.

3. **Regeneration of RuBP:** GAP reacts with ATP and regenerates the RuBP used in the first stage.

A brief diagram of the main reactions of the Calvin cycle can be seen in figure 1.5.

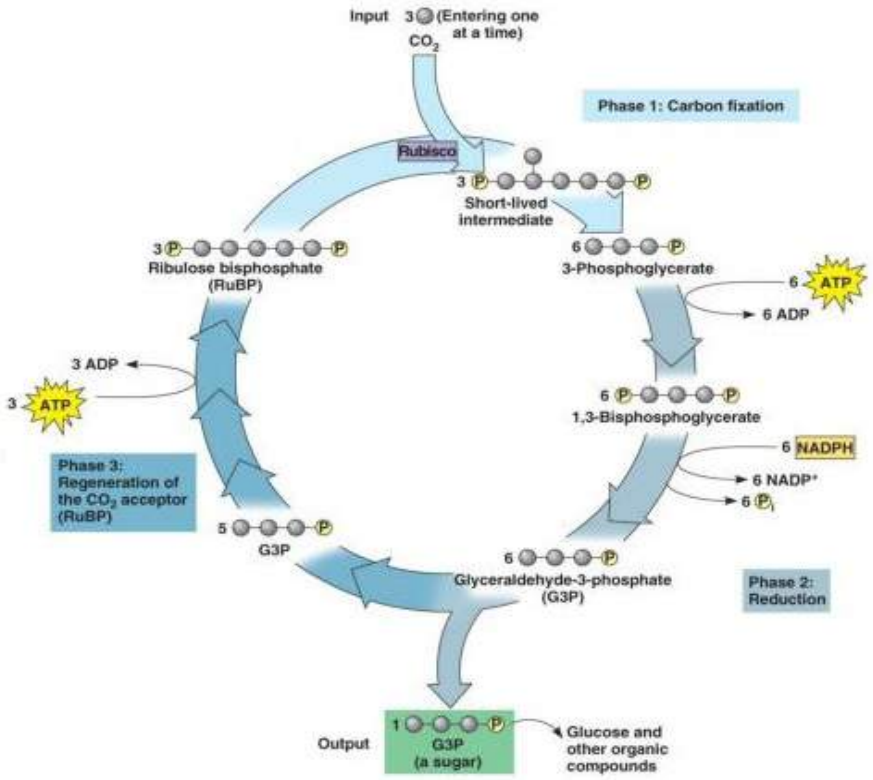

Figure 1.5: Calvin cycle main reactions diagram.

Overall, the general equation of the Calvin cycle is:

$$3CO_2 + 3RuBP + 9ATP + 6NADPH \rightarrow 6GAP + 9ADP + 6NADP^+ + 8P_\mathrm{i} \quad (1.5)$$

$$5GAP \rightarrow 3RuBP \quad (1.6)$$

Where reaction 1.5 represents CO_2 fixation and GAP reduction steps and reaction 1.6 represents RuBP regeneration. The missing GAP from reactions 1.5 and 1.6 is used in glucose synthesis.

1.3 Light harvesting pigments

1.3.1 Chlorophylls

Chlorophyll molecules constitute the main photoreceptors in the vast majority of photosynthetic organisms[23] and they are composed of a porphyrinic ring and a long hydrocarbonated phytol tail. The porphyrinic ring is coordinated to a central metallic cation (usually Mg^{+2}) and possesses a fifth hydrocarbonated ring. Also, depending on the chlorophyll, different functional groups are attached to the porphyrin ring. The phytol tail has a variable length depending on the type of chlorophyll and helps the chlorophyll to stay inside the thylakoidal membrane due to its high hydrophobicity. Chlorophyll structure is shown in figure 1.6.

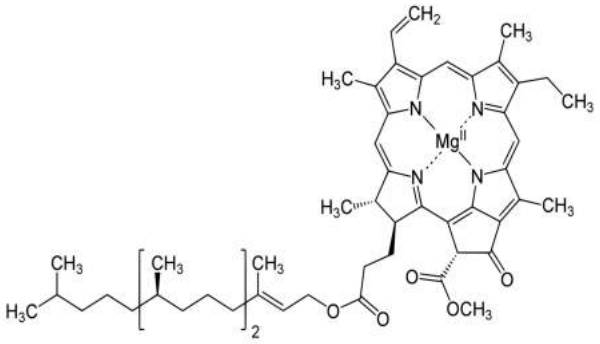

Figure 1.6: Chlorophyll molecular structure.

Depending on the functional group attached to the porphyrin ring, there are 5 different types of chlorophylls: a, b c_1, c_2 and d. All these chlorophylls are present in green algae, but only chlorophylls a and b are found in higher plants. The porphyrin ring determines the spectroscopic features and the absorption spectrum of the chlorophyll in the visible, due to its high level of π conjugation along the planar ring. In this sense, we can consider chlorophyll spectroscopic behaviour similar to the porphyrin ring one. Porphyrin has a D_{4h} symmetry group and its main absorption corresponds to two π-π^* transitions between the two highest occupied molecular orbitals (HOMO), a_{1u} and a_{2u} and the two e_g lowest unoccupied molecular orbitals (LUMO).[24]

The two configurations recombine due to its similar energy and the final electronic states are split into two with ^1E_u symmetry. The highest of those states is called the Soret band (B band) and it is found around 400-500 nm while the lower state is called the Q band[25] and appears between 600 and 700 nm. In turn, and due to the squared symmetry of the cycle, Q and B bands split into two sub-bands corresponding to x-polarized and y-polarized transitions, Q_x/Q_y and B_x/B_y, respectively.[23,25] Porphyrin molecular orbitals mix and its associated absorption spectrum can be seen in figure 1.7.

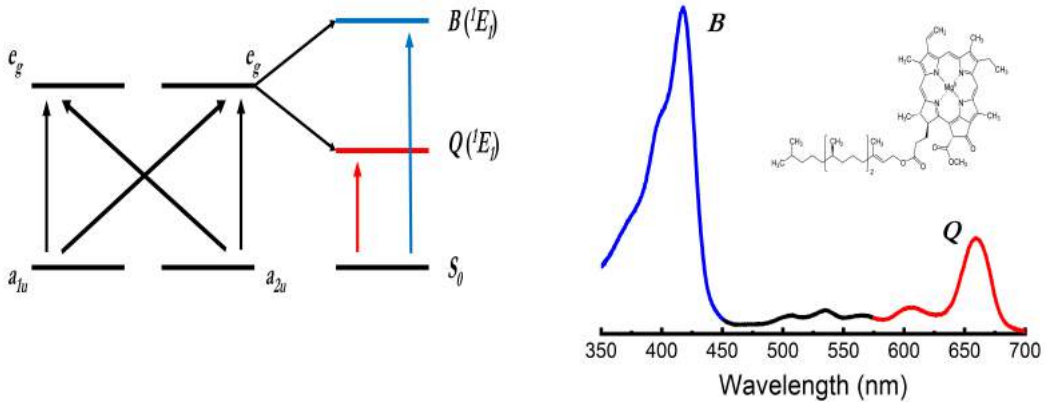

Figure 1.7: Porphyrin molecular states mix process *(left)* and its absorption spectrum *(right)*.

In reality, chlorophylls do not satisfy this theoretical model perfectly due to the fact that the different functional groups attached to the porphyrin group cause distortions in the ring group. These distortions create a quasi D_{4h} symmetry with the subsequent shifts in the absorption spectrum that explain the differences between chlorophylls.

Chlorophylls ground state, like the rest of the described excited states are singlet, making triplet state population by direct pumping forbidden by selection rules. Nevertheless, those states can be reached via excited singlet states intersystem crossing (ISC). In fact, excited triplet state formation in algae chlorophylls is a critical step in their survival, as ^{3}Chl* can lead to the formation of singlet oxygen via spin exchange (SE).[26] Singlet oxygen is part of a group called reactive oxygen species (ROS) and it can severely damage algal cellular structure[27] according to the reaction:

$$^3Chl^* + {}^3O_2 \rightarrow {}^1Chl + {}^1O^*{}_2 \tag{1.7}$$

Chlorophylls are principally found in the thylakoidal membrane attached to different proteins and pigments forming the photosystems. The main agent that anchor chlorophylls inside photosystems is, indeed, the Mg^{+2} cation present in the center of the porphyrin ring because it easily interacts with other aminoacids such as histidine (His).[28,29]

1.3.2 Carotenoids

Carotenoid molecules play several roles in photosynthesis ranging from protein stabilisation inside the thylakoid membrane[30,31] to light harvesting[32,33] and, specially, photoprotection.[34] They are composed of a long isoprenoid chain with two hydrocarbonated rings in both extremes and depending on the degree of hydrogenation, chain length or the presence of oxygenated functional groups, we can classify more than 1100 different types of them.[35] A carotenoid, β-carotene, structure is shown in figure 1.8:

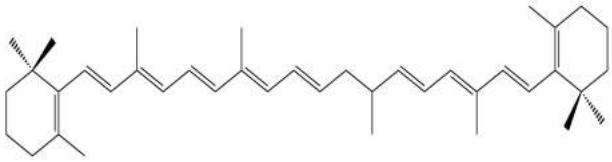

Figure 1.8: β-carotene molecular structure.

Depending on the absence or presence of oxygen in their structures, carotenoids can be classified in carotenes (those without oxygen) and xantophylls (with oxygenic functional groups). In photosynthetic organisms, the most important carotenoids are β-carotene (β-Car), lutein (Lut), violaxanthin (Vio), zeaxanthin (Zea) and neoxanthin (Neo) and all of them are found inside PSI and PSII.[36–38] In particular, carotenes are found in the photosystems core while the xantophylls are present in the antenna complexes.

Carotenoid spectroscopic features are determined mainly by the π conjugation along the carbon double bonds chain. As we did before, we can consider carotenoids spectroscopic behaviour relatable to a similar molecule family, the polyenes. Polyenes have a C_{2h} symmetry group and, as only π orbitals are relevant in the electronic structure, their excited molecular orbitals have a_u and b_g symmetry, being the b_g molecular orbital the first excited state and two energetically a_u molecular orbitals the second and the third excited states. Similarly to chlorophylls, energetically close a_u molecular orbitals can interact with each other and split into two electronic states with A_g symmetry, being the lowest one the S_1 state. On the other hand, b_g states does not interact with close molecular orbitals and constitute the S_2 state with a B_u symmetry. According to the free-electron model, the ground state has an A_g symmetry making $S_0 \rightarrow S_2$ the only transition permitted by selection rules and observable between 400 and 500 nm. Polyenes molecular orbitals mix and electronic state distribution alongside with its associated absorption spectrum can be seen in figure 1.9.

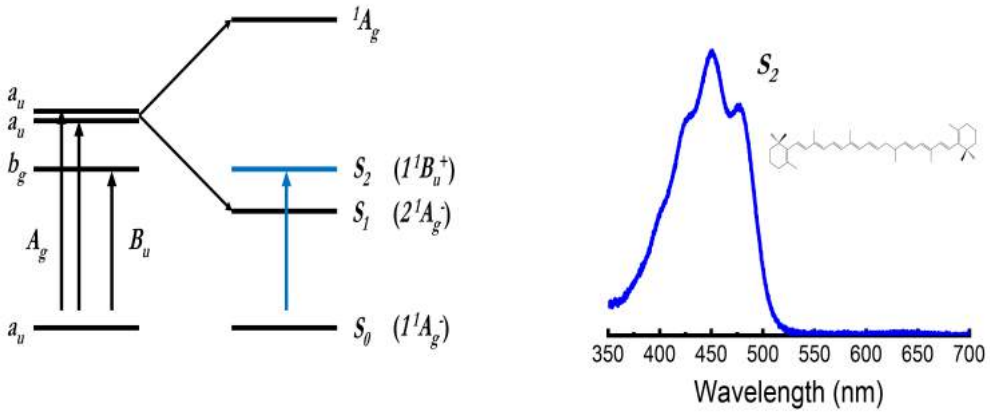

Figure 1.9: Polyene molecular states mix process *(left)* and its absorption spectrum *(right)*.

Carotenoids participate in some photoprotection mechanisms which quench the excess of chlorophyll excitation. One of them is called the xantophyll cycle and involves the participation of violaxanthin, zeaxanthin and an intermediate between the two, antheraxanthin.[39,40] In high light conditions, violaxanthin de-epoxidises and form zeaxanthin, a light absorbing competitor to chlorophylls. This reaction is catalyzed by a pH-dependent lumenal enzyme, violaxanthin de-epoxidase (VDE). When light stress is not so high, zeaxanthin epoxidase (ZE) activates and converts zeaxanthin back into violaxanthin. A brief diagram of xantophyll cycle can be seen in figure 1.10

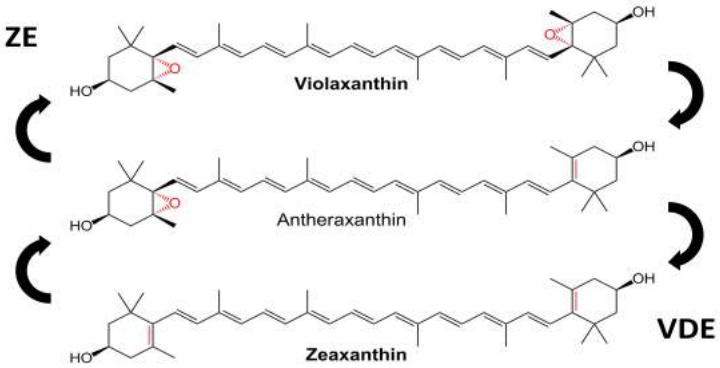

Figure 1.10: Xantophyll cycle diagram.

However, in green algae this mechanism is a secondary route, as carotenoid can undergo a spin exchange process to eliminate the presence of ^{3}Chl* or even quench the singlet oxygen itself[26] following the reactions:

$$^3Chl^* + {}^1Car \rightarrow {}^1Chl + {}^3Car^* \tag{1.8}$$

$$^1O^*{}_2 + {}^1Car \rightarrow {}^3O_2 + {}^3Car^* \tag{1.9}$$

Where reactions 1.8 and 1.9 show the quenching of excited triplet chlorophyll and the direct quenching of singlet oxygen by carotenoids, respectively. In general, the most common carotenoid triplet state formation occurs through the chlorophyll triplet spin exchange (equation 1.8) after an excited chlorophyll intersystem crossing following the scheme ^{1}Chl* $\rightarrow$ ^{3}Chl* $\rightarrow$ ^{3}Car*.

1.4 Photosystems

Photosystems I and II are protein complexes whose main role is to absorb light and generate the charge separation that starts the electron transport chain. Photosystems are located in the thylakoid membrane with PSI being ubicated in the stroma lamellae and PSII in the grana.

Despite the fact that both PSI and PSII are functionally different, they show two clearly distinctive parts: a core in which the electron transport takes place and an antenna system in charge of light absorption and energy transfer to the core. Chlorophylls and carotenoids are also present in these moieties. In particular, Chl a and carotenes are found in the core complexes and Chl a, Chl b and xantophylls are present in the antennas complexes.

A photosystem core is composed by a special pair of Chl a that forms the reaction center of the photosystem and a series of polypeptides named *Psa* and *Psb* referring to PSI and PSII, respectively. Moreover, antennas are formed by multiple polypeptides called *light harvesting complexes* (*lhc*), and equivalently to PS cores, they are referred as *lhca* and *lhcb* for PSI and PSII, respectively. For these reason, cores are usally named PSI/PSII and antennas are referred as LHCI/LHCII, being the whole photosystem named PSI-LHCI/PSII-LHCII supercomplexes, respectively.

1.4.1 Photosystem I

PSI-LHCI supercomplex main role is acting as a light-dependent plastocyanin-ferredoxin oxidoreductase. In green algae, its overall stucture resembles a fan with a core composed of fifteen *Psa* subunits and an antenna made by 10 *lhca* subunits distributed in two semi rings shape.[41,42] Also, PSI core contains the electron acceptors A_0 (*Chl a*), A_1 (phylloquinone), F_X (a Fe_4–S_4 cluster) and the pair of special chloropylls (P_A and P_B) that form the so called P_{700} reaction center.

The PSI fifteen subunits are named PsaA-O and while twelve of them are transmembrane (PsaA, PsaB, PsaF, PsaG, PsaH, PsaI, PsaJ, PsaK, PsaL, PsaM, PsaN, PsaO), the other three are extrinsic and face the stromal side of the thylakoid membrane (PsaC, PsaD, PsaE). LHCI semi rings are concentric and face the PsaG-PsaF-PsaJ-PsaK side. Each semiring is made of four lhca subunits with lhca-a, lhca-b, lhca-c and lhca-d placed in the inner ring and lhca-e, lhca-f, lhca-g and lhca-h forming the outer ring. The remaining lhca subunits, lhca-i and lhca-j, are found as a dimer facing the PsaB–PsaH–PsaI–PsaM core side. An overall diagram of PSI-LHCI supercomplex can be seen in figure 1.11.

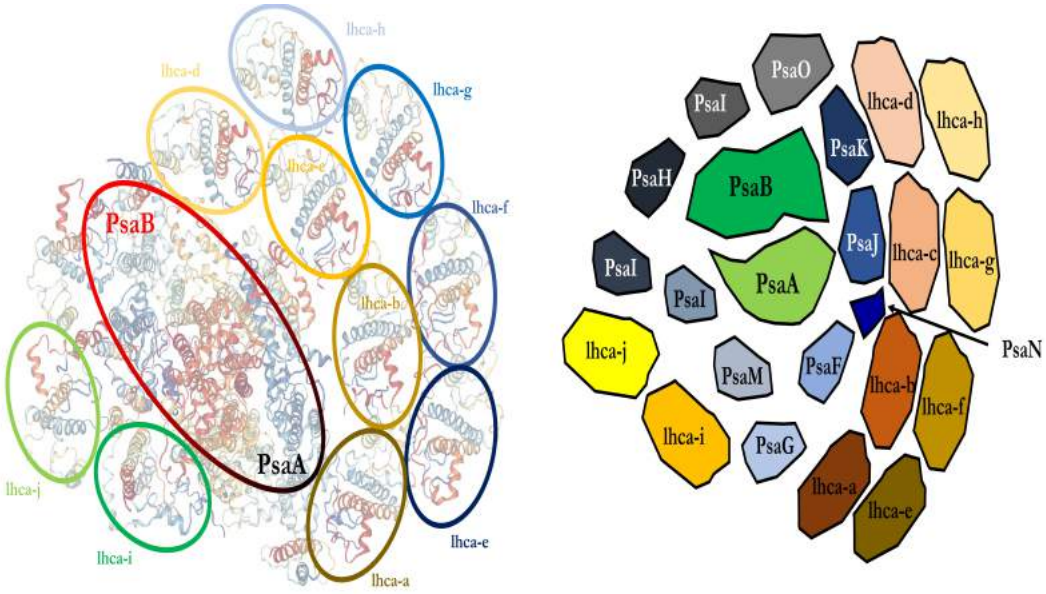

Figure 1.11: Supramolecular organization of PSI-LHCI supercomplex. *(Left)* Top view (excluding PsaC, PsaD and PsaE). *(Right)* Diagram model.

All these subunits contain chlorophylls and carotenoids. In total, 244 chlorophylls are found in PSI-LHCI supercomplex, 145 of which placed in the antenna and the remaining 99 standing in the core. On the other hand, we can find 54 carotenoids in the supercomplex, 22 inside the PSI core and the rest of them within the *lhca* antennas.

However, the question about how the energy collected by the antenna complex is sent to the reaction center in green algae still remains. In the first place, a deep funnel model was proposed, in which electronic energy transfer (EET) is performed sequentially from high-energy to low-energy pigments until the primary donor is reached.[43] Nevertheless, this model does not explain very well why almost all PSI core complexes have chlorophylls that absorb at higher wavelengths than the primary donor, the so-called chlorophyll red forms. In this sense, a roller coaster-like model was proposed, in which the energy gap between the red chlorophylls and the primary donor, P_{700}, was filled by the thermal energy of the physiological medium.[44,45] Recently, X. Qin et al. performed single-particle cryo-electron microscopy experiments in green algae LHCI[41] and proposed a energy transfer model between LHCI and PSI core in which the energy collected by the outer semi ring was transferred to the inner semi ring and thus transferred to the PSI core in most of the cases. Nonetheless, the mechanisms of EET between *lhcas* within each semi ring (if any) are still unknown. This model also proposed a direct EET from the lhca-i/lhca-j dimer to the PSI core and an additional EET between each monomer. A picture of the LHCI-PSI energy transfer model can be seen in figure 1.12

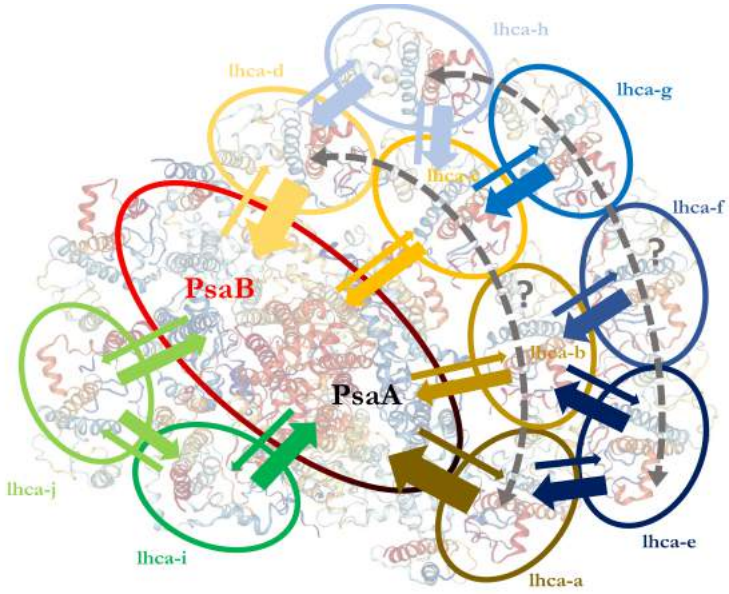

Figure 1.12: LHCI-PSI energy transfer model.

1.4.2 Photosystem II

PSII-LHCII supercomplex main function is acting as a light dependent water plastoquinone oxidoreductase. In green algae, its structure consists in a PSII core and two antenna layers composed of major trimeric LHCII proteins[46] and minor monomeric LHCII proteins (CP26 and CP29).[47] PSII core is formed by a polypeptide dimeric complex that contains eighteen intrinsic subunits (PsbA, PsbB, PsbC, PsbD, PsbE, PsbF, PsbH, PsbI, PsbJ, PsbK, PsbL, PsbM, PsbR, PsbTc, PsbW, PsbX, PsbZ and Psb30) and three extrinsic subunits (PsbP, PsbQ and PsbO).[48] Subunits PsbA and PsbD form the reaction centre proteins D1 and D2, respectively. On the other hand, PsbB and PsbC form the inner antennas CP47 and CP43, respectively.[49] The core also contains the reaction center P_{700}, pheophytin and the quinone pool (Q_A/Q_B). Alongside with subunits D1 and D2, cytochrome b-559 stabilizes the polypeptide dimer complex and, under it, the oxygen evolving complex (OEC) can be found. OEC is made of tyrosine (Y_Z), a manganese cluster and three extrinsic subunits previously mentioned to provoke the water splitting.

In *C. Reinhardtii*, the major trimeric LHCII antenna is composed by four types of LHCII apoproteins which are involved in photoprotection mechanisms: type I (LhcbM3, LhcbM4, LhcbM6, LhcbM8 and LhcbM9), type II (LhcbM5), type III (LhcbM2 and LhcbM7) and type IV (LhcbM1).[50–55] In addition, depending on the strength of the interaction core-LHCII, the LHCII antenna trimers can be classified as S-LHCII, M-LHCII or L-LHCII (S, M and L stands for strongly, moderately or loosely association).

The three types of major LHCII and the minor antennas form the two layers in which the LHCII antenna complex is divided. The inner antenna layer is made of S-type LHCII and the minor antennas CP26 and CP29 and constitutes the C_2S_2 supercomplex. The outer layer is composed by M and L-type LHCII antennas and binds the C_2S_2 supercomplex creating a larger structure known as the $C_2S_2M_2L_2$ supercomplex.[56] An overall diagram of PSII-LHCII supercomplex can be seen in figure 1.13.

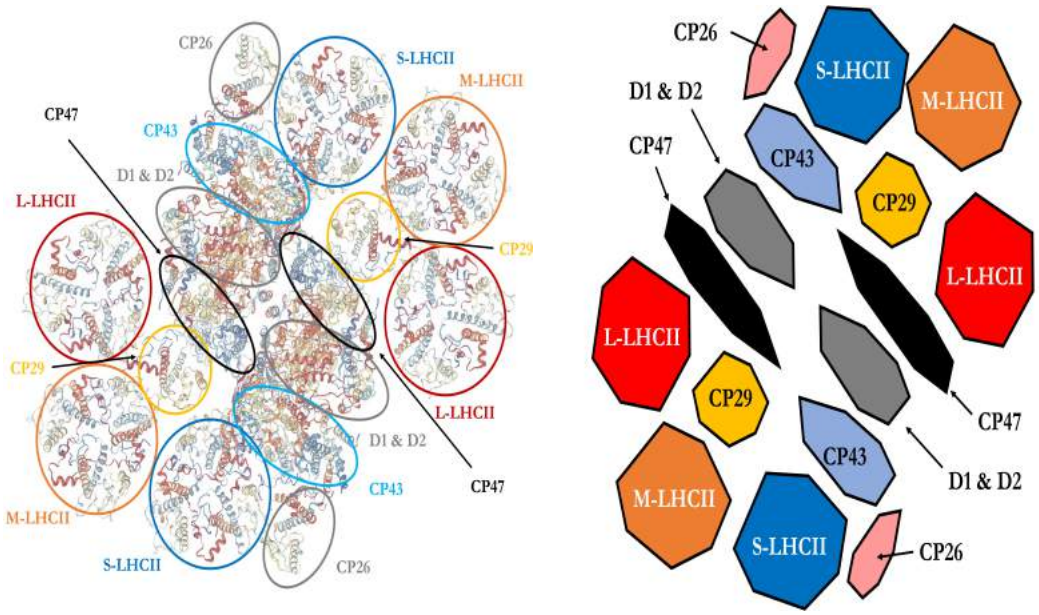

Figure 1.13: Supramolecular organization of PSII-LHCII supercomplex. *(Left)* Top view (excluding PsaP, PsaQ and PsaO). *(Right)* Diagram model

As reported in Drop et al.,[57] each LHCII apoprotein binds fourteen chlorophylls and four carotenoids. Considering this, we can estimate a total of 602 chlorophylls and 172 carotenoids within the $C_2S_2M_2L_2$ supercomplex with 294 Chls and 84 Cars binding the PSII core and 308 Chls and 88 Cars binding the LHCII antenna.

Recently, Sheng, X. et al. perfomed single-particle cryo-electron microscopy experiments to determine the structure of the $C_2S_2M_2L_2$ supercomplex and the energy transfer pathways between the LHCII antenna complex and the PSII core.[48] They propose a downhill model in which the peripheral LHCII antennas transfer the energy to the PSII RC through the minor antennas CP29, CP43 and CP47. On the other hand, the energy collected by CP26 is directly transferred to CP43. A diagram with the different excitation pathways can be seen in figure 1.14

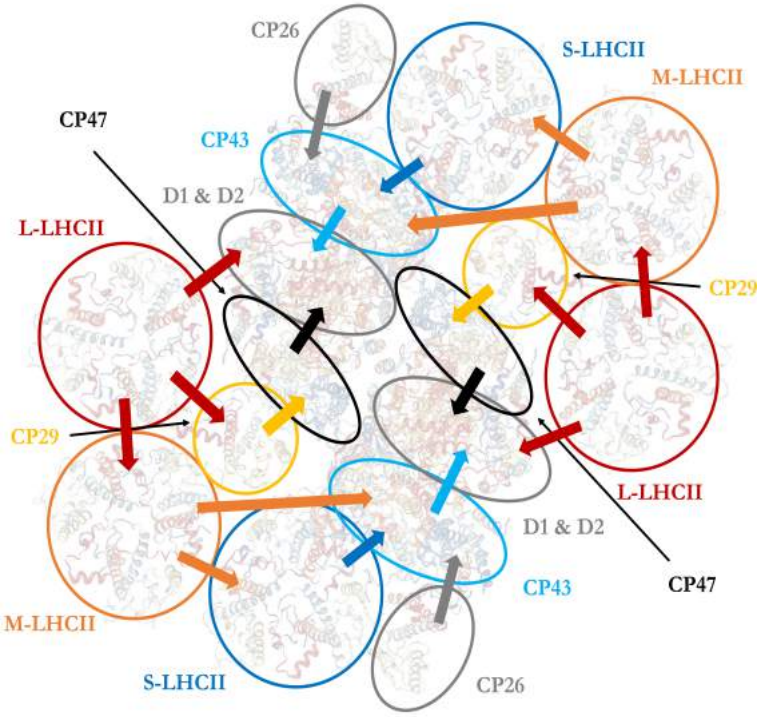

Figure 1.14: LHCII-PSI energy transfer model.

1.5 Photoinhibition and photoprotection

Light is a vital element for photosynthetic organisms survival. However, an excess of it can be harmful as many reactive intermediates generated in the process can damage the thylakoid membrane and the whole photosynthetic apparatus. This photodamage process is often referred as photoinhibition, since the light used for generating these non-desired intermediates cannot be used for the photosynthesis itself and therefore, reduces photosynthesis efficiency.[58–60]

As we saw in section 1.2, photosynthesis starts with the absorption of a photon by the LHCs of PSII which results in the excitation of a chlorophyll molecule to a singlet excited state (^{1}Chl*). At this point, the excited singlet chlorophyll can follow several pathways back to the ground state: (a) it can fluoresce, (b) it can be de-excited by thermal processes, (c) it can transfer its energy to the PSII reaction center and start the electron transfer chain and (d) it can generate an excited chlorophyll triplet state. An overall scheme of all these processes is shown in figure 1.15.

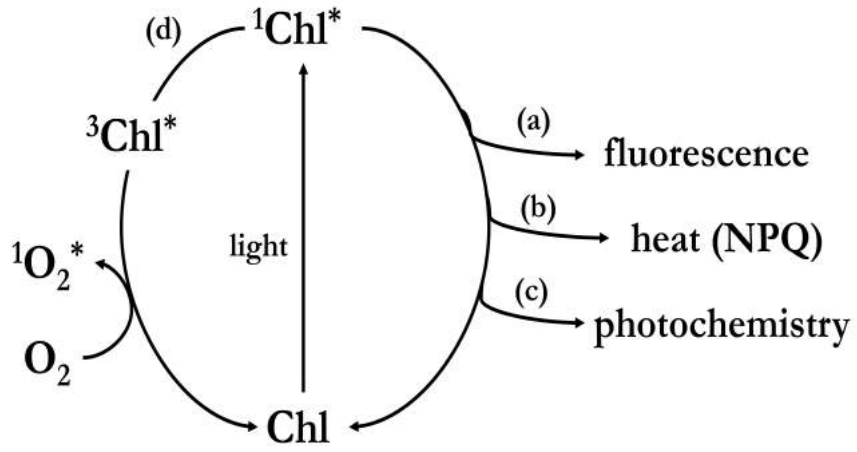

Figure 1.15: Excited singlet chlorophyll relaxation pathways. (a) fluorescence, (b) thermal de-excitation, (c) photosynthetic reactions, (d) chlorophyll triplet formation.

Among these options, the most efficient one is the starting of the electron transfer chain and the least efficient the ^{1}Chl* fluorescence with a quantum yield of ≈0.6-3 %.[61] Chlorophyll triplet formation is not an efficient process as it shows a quantum yield of 4%; however, this value can increase up to 25% under high amounts of light.[62] If the amount of light is too high, the excited singlet chlorophylls accumulate and thus, they can convert into excited triplet chlorophylls (^{3}Chl*) via intersystem crossing. Excited triplet chlorophylls are highly reactive species that are not intrinsically dangerous, but they can interact with the triplet oxygen formed during the water splitting and generate singlet oxygen via spin exchange (see formula 1.7) which can oxidize proteins, pigments[63] or thylakoid membrane lipids[64] causing even cell death in an extreme case.

In general, differences in the luminous flux received by algae are due to environmental reasons which act at timescales ranging from months (seasons change) to hours (day-night cycle) or even minutes (unequally distribution of algae in a colony, bad weather conditions). In order to deal with this uneven light distribution and to avoid photoinhibition, algae have developed the so called photoprotection mechanisms.

Photoprotection mechanisms can be classified into two groups depending on their timescale and nature, having short-term and long-term photoprotection mechanisms. The biological difference between them is that in the short-term mechanisms, energy excess is released as heat with no protein synthesis involved in the process while in the long-term mechanisms, more proteins involved in the photosynthetic apparatus must be synthesized to deal with the new requirements of the photosynthesis reactions.

1.5.1 Short-term photoprotection mechanisms

Non-photochemical quenching (NPQ) is a group of complex mechanisms by which the photodamage is controlled by decreasing the efficiency of the light harvesting capabilities of the photosynthetic apparatus. Its activation depends on the intrathylakoidal pH gradient generated during the electron transport chain and it is described by the following formula:

$$NPQ(t) = \frac{(F_m(t) - F_m^{'}(t))}{F_m^{'}(t)} \tag{1.10}$$

Where F_m is the maximum fluorescence measured in dark conditions and F_m' represents the maximum fluorescence at different times during illumination. NPQ has three components which are defined by their respective lifetimes after excitation:

1. **qE:** it is the fastest component and consists in the thermal dissipation within LHCII after lumen acidification.[65]

2. **qT:** it is based in changes in the antenna sizes of LHCII and LHCI due to phosphorylation or antenna subunits migration. This term is also referred as state transitions.[66]

3. **qI:** it is the slowest NPQ component and consists in a reversible photoinhibitory quenching, i.e, damage to PSII reactions centers.[58]

It is important to mention that the physical mechanisms underlying NPQ are conserved in all photosynthetic organisms but the organisms capacity to develop NPQ can vary a lot among them. In fact, we can see differences in NPQ capacity among the same species as well. For example, in the case of *C. Reinhardtii*, environmental conditions can drastically vary its NPQ capacity from ≈0 to ≈2.[67] A more detailed analysis of the components of NPQ is shown below:

• **qE** As previously established, qE consists in the thermal dissipation of excess energy from LHCII after lumen acidification. This process is highly efficient (around 80% of the excess energy is released as heat[68]) and it is related to the xanthophyll cycle we saw in subsection 1.3.2. (see figure 1.10).

To trigger qE, it is mandatory to have an element that can sense variations in the luminal pH and amplify the quenching. In plants, pH detection is performed by PsbS while quenching amplification is done by lhcb.[36] On the other hand, in *C. Reinhardtii*, both functions are performed by an specific protein within a stress-related LHC subgroup called LHCSR (light harvesting complex stress-related).[69] Morphology and function of the lhcsr family members will be discussed in the following section.

• **qT** States transitions consist in the migration of LHC antenna subunits between PSI and PSII, reducing or increasing their relative antenna sizes in the process. Photosystems I and II possess different absorption features and while both photosystems have an absorption band in the visible red region, PSI shows a broad absorption band in the far-red region which is missing in PSII.

In natural conditions, light availability fluctuates over time,[66] so photosynthetic organisms are constantly redistributing the antenna sizes of their photosystems to optimize the efficiency of the electron flow. According to this antenna redistribution, we can identify state 1, in which PSII activity is more prominent than PSI, and state 2, in which PSI activity gains more importance than PSII.

Differences between both states are also observable looking at their emission spectra. In state 1, the intensity of the far-red signal is lower than the intensity from the red part while in state 2, the situation is the opposite. For these reasons, state 2 shows higher levels of NPQ compared to state 1.

• **qI** this NPQ term is usually vaguely defined and refers to all NPQ processes happening in a longer time scale than the transthylakoid pH gradient.[70] Due to this fact, qI comprises all phenomena related to the photodamaging of PSII. The role of the ΔpH or the presence of zeaxanthin is still under debate and for that reason, some authors proposed splitting the term "qI" into "sustained, pH-dependent NPQ"[71–73] and "sustained, pH-independent NPQ".[73]

1.5.2 Long-term photoprotection mechanisms

Long-term photoprotection mechanism are triggered when photosynthetic organisms are exposed to a high light stress conditions for a long time (hours, days). In general, these mechanisms involve morphological and structural changes such as chloroplast movement or the reduction of photosystems antenna sizes through the no expression of proteins. Other mechanisms would involve the accumulation of antioxidant species such as α-tocopherol or carotenoids.

1.6 Light harvesting complex stress related proteins

In the previous section, we mentioned that qE triggering in green algae *C. Reinhardtii* was due to the activation of one protein from the light harvesting stress-related (lhcsr) family. This group is composed of two proteins, LHCSR1 and LHCSR3, encoded by three genes (*lhcsr1* for LHCSR1 and *lhcsr3.1* and *lhcsr3.2* for LHCSR3).

LHCSR1 and LHCSR3 structure are practically identical as they are composed of three transmembrane α-helices with short helices facing the lumenal part. The transmembrane helices also bind pigments (chlorophylls and carotenoids) with a variable ratio depending on the protein whereas the short helices bind acid groups (aspartic and glutamic).[28,74,75] An overall structure for the LHCSR proteins is shown in figure 1.16.

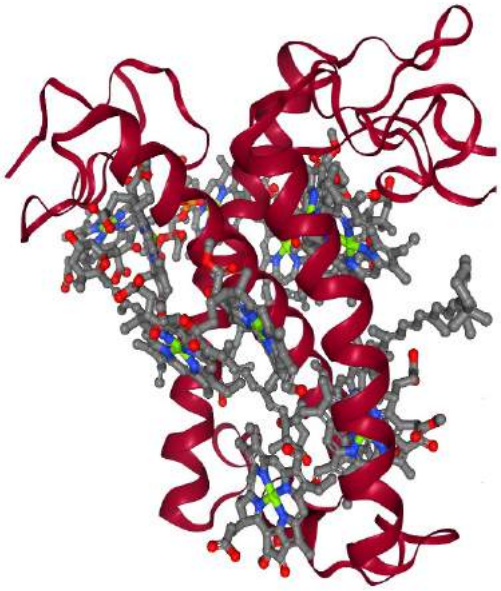

Figure 1.16: Common structure of a LHCSR protein family member.

In *C. Reinhardtii* qE activation, LHCSR3 plays a major role while LHCSR1 is relegated to a secondary position. LHCSR3 importance was demonstrated by Peers et al. by comparing NPQ induction of a *C. Reinhardtii* wild type algae with a mutant (*npq*4) lacking LHCSR3 protein.[69] Under high light conditions, the authors observed NPQ induction both in the wild type and in the *npq4* mutant but the NPQ value (as defined in equation 1.10) was lower in the case of the *npq4* mutant.

LHCSR3 also plays a role as a pH sensor through the acid residues of its C terminus.[76,77] Ballottari et al. and Liguori et al. studied the pH sensing capacity of LHCSR3 by confronting a strain of a wild-type *C. Reinhardtii* against a mutant in which the acid residues were suppressed. Acid residues suppression was achieved either by the removal of all acid sites[76] or by the substitution of the acid groups for pH-insensitive groups.[77] In both works, the authors studied the ^{1}Chl* decay at 680 nm using TRF in wild-type *C. Reinhardtii* and the mutant at acid pH (pH=5) and neutral pH (pH=7.5). In both

cases, they found that no NPQ induction was seen in the mutant at low pH as opposed to the wild type protein and thus they concluded that the acid groups in the C-terminus were key for pH sensing.

Tokutsu and Minagawa studied where LHCSR3 protein is found within the thylakoid membrane.[78] To do so, the authors compared the isolated PSII-LHCII supercomplex from wild type *C. Reinhardtii* with the *npq*4 mutant under two light intensities (high and low) . They observed that LHCSR3 was only found in the wild type PSII-LHCII supercomplex under high light conditions whereas LHCSR3 was not found in the wild type under low light conditions neither in the *npq*4 mutant in any light intensity condition. Thus, they studied the fluorescence of the wild type PSII-LHCII-LHCSR3 supercomplex under two pH conditions (acid, pH = 5.5 and neutral pH = 7.5) and found that the supercomplex showed a high fluorescence at acid pH whereas low fluorescence was observed at neutral pH. Therefore, the authors proposed a three steps model for qE quenching induction: (I) expression of *Lhcsr*3 gene under high light conditions, (II) binding of LHCSR3 to the PSII-LHCII supercomplex and (III) conformational change of LHCSR3 after lumen acidification.

1.7 Time-resolved spectroscopic techniques

Spectroscopy can be defined as the study of the light-matter interactions. These interactions were described by Einstein[79] and they can be classified in (a) absorption, (b) spontaneous emission and (c) stimulated emission. A brief scheme of all these interactions is shown in figure 1.17.

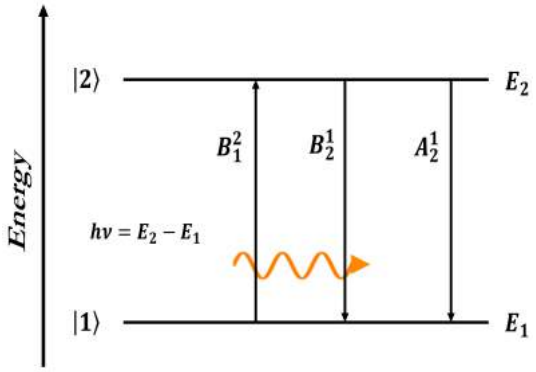

Figure 1.17: Fundamental light-matter interactions with their associated Einstein coefficient: absorption (B_1^2), stimulated emission (B_2^1) and spontaneous emission (A_2^1).

There is a group of spectroscopic techniques known as time-resolved spectroscopies which are useful due to the fact that the measured quantity can be associated with the states population of a photoactive species. Therefore, we can register non-equilibrium population dynamics. For the purpose of this thesis, we will focus on time-resolved fluorescence (TRF) and transient absorption (TA).

1.7.1 Time-resolved fluorescence

A time-resolved fluorescence measurement consists in recording the spontaneous emission of a certain fluorophore excited via light absorption. Fluorescent light usually falls into the Visible-NIR spectral regions so it can be spectrally resolved very easily using a grating. The measured quantity of a TRF measurement is usually the fluorescence emission depending on wavelength and time after excitation. A typical spectrally resolved measurement map can be seen in figure 1.18.

Spontaneous emission is a genuine stochastic process and while the single photon emission process itself happens in an ultrashort timescale (sub-fs), the fluorophore excited state lives much longer than that (from fs to μs). The individual fluorophores remain in the excited state for a certain amount of time and go back to the ground state at a random time after excitation, creating a well defined temporal probability distribution.

Also, spontaneous emission was described theoretically by Einstein in 1917 using the so-called A and B coefficients[79] (see figure 1.17). If we consider the simplest case for spontaneous emission, i.e. an ideal excited fluorophore in a two levels system, the probability of de-excitation (dW) within a defined time interval (dt) is described by the A_2^1 coefficient following the formula:

$$dW = A_2^1 dt \tag{1.11}$$

If we now consider an excited state population n, the temporal probability of the photon emission is defined by:

$$dW = \sum_{i=1}^{n} A_2^1 dt = A_2^1 n dt \tag{1.12}$$

De-excitation naturally implies excited state depopulation and thus we can define the probability of de-excitation by dW=-dn. Therefore, we can rewrite equation 1.12 as:

$$dn = -A_2^1 n dt \tag{1.13}$$

If we reorder and solve the differential equation 1.13, we obtain:

$$n(t) = n(0)e^{-A_2^1 t} \tag{1.14}$$

We can thus correlate the excited state population with the fluorescence intensity through the formula:

$$I(t) = I_0 e^{-\frac{t}{\tau}} \tag{1.15}$$

Where I_0 and τ are the fluorescence at time zero and the decay time of the fluorophore, respectively.

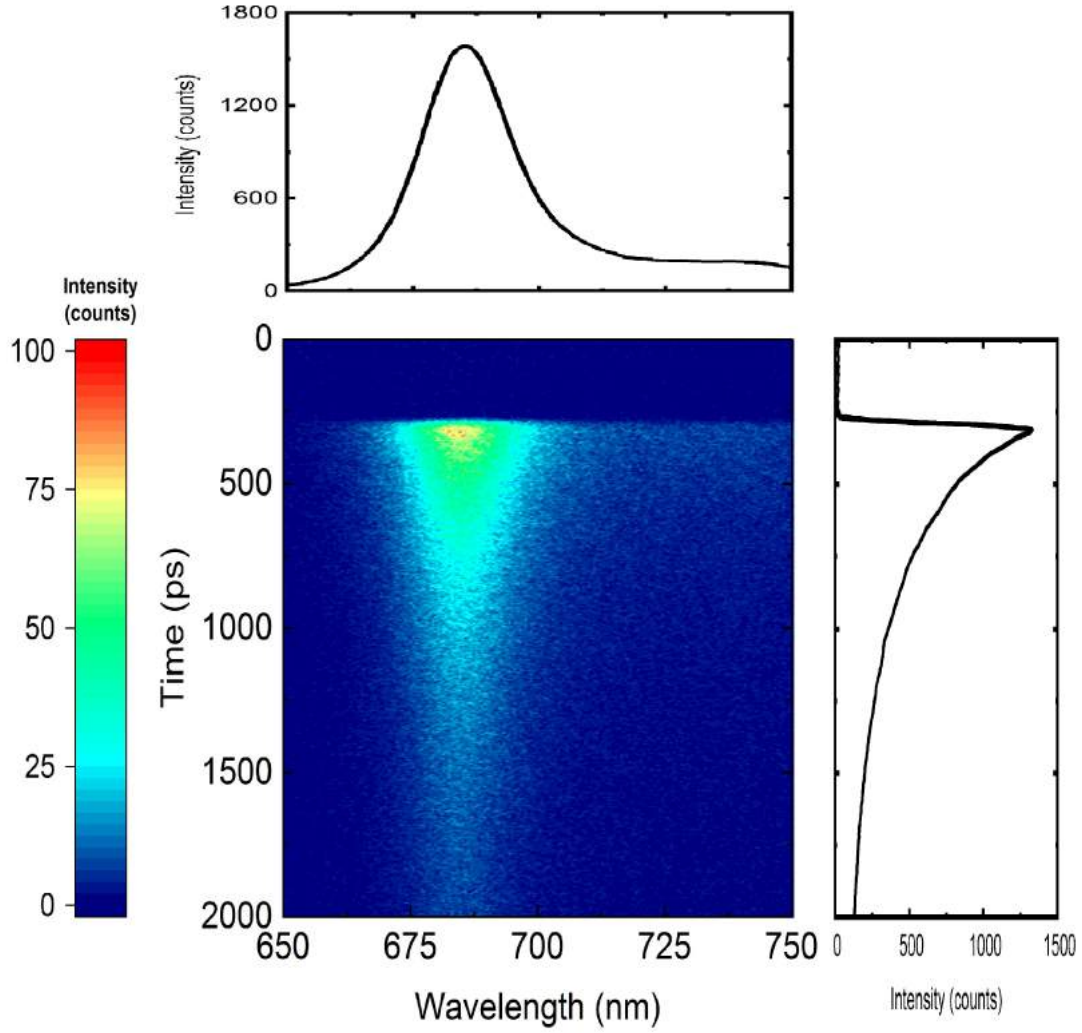

Figure 1.18: Time-resolved fluorescence map of an *in vitro* LHCSR3 protein showing: (Upper panel) Spectrum integrated between 350-500 ps after excitation and (Side panel) kinetics integrated between 680-690 nm.

Time-resolved fluorescence measurements are usually performed using a light pulse as the excitation and an appropriate detection system. In consequence, the measured temporal profile will always be a convolution between the instrumental response function (IRF) of the system and the kinetics of the fluorophore to be measured. For this reason and to minimize the use of deconvolution, ultrashort pulses are desirable in this technique.

There are multiple detection systems for TRF but they are classified in two types: electronic and optical. Optical detection is based in the interaction between the emitted light and a second light beam before detection whereas the electronic detection consists simply in the recording of the emitted light by electronic devices. Another difference between these types consists in the limitation of their temporal resolution. Hence, the temporal resolution of the electronic detection systems is limited by the frequency bandwidth of its electronic compounds and usually achieve temporal resolutions of ≈100 ps. On the other hand, optical detection systems are only limited by the temporal width of the light pulse used for excitation and therefore we can achieve temporal resolutions of <100 fs in the best case scenario.

Electronic detection

Fast photo-diode and oscilloscope The fluorescent light arrives to a fast photo-diode and generates a current that is registered as a function of time using an oscilloscope.[80] The best resolution provided by these systems is ≈1 ns.

Time-correlated single photon counting (TCSPC) In this case, we need to work in a single-photon statistic regime. To reach that regime, the emitted light is attenuated to get single-photon statistics and then selectively amplified with a photomultiplier tube. An external detector (usually a fast photo-diode) is used to register the temporal difference between the arrival of the excitation pulse and the detection of the fluorescent photon. By registering multiple single photons, an histogram is built showing the kinetics of the fluorophore.[81,82] The best resolution provided by these systems is ≈100 ps.

Streak camera The fluorescent light is converted into photoelectrons in a photocathode placed within a vacuum tube. The electrons cross the vacuum tube and are deflected by a pair of time-dependent sweeping electrodes placed perpendicularly to the electron trajectory. The deflected electrons then hit a phospor screen and are reconverted into light which is recorded in a CCD camera.[83,84] The best resolution provided by these systems is ≈1 ps.

Optical detection

Upconversion In this case, the pump beam is split into two by a beam splitter generating the excitation and the gate beams. The excitation beam is used to excite the sample and generate the fluorescent light. The emitted light is then overlapped temporally and spatially with the gate beam inside a nonlinear medium generating a signal whose frequency equals the sum of the fluorescent and gate beams. Finally, the signal is spectrally selected and detected, obtaining a fluorescence measurement in the temporal width of the gate.[85]

In our case, we will use a streak camera detection method for all TRF measurements with the setup present in Center for Nano Science and Technology (CNST) in Milano. Streak camera principle and a full description of the TRF setup is explained in chapter 2 of this thesis.

1.7.2 Transient absorption

A transient absorption measurement consists in recording the stimulated emission of a certain sample excited after light absorption. Stimulated emission detection requires inevitably the presence of two light beams on the sample: the first beam promotes the sample to an excited state and the second one is used to cause the stimulated emission from the excited sample. These beams are usually known as pump and probe, respectively and therefore, it is very common to name these techniques as pump-probe techniques. The wavelengths of pump and probe beams vary from sample to sample. The pump wavelength is usually chosen to match the ground state main absorption band while the probe wavelength is usually selected to monitor the transitions of interest.

Due to the fact that a probe beam is needed for detection, all TA measurements will have a certain background. To subtract the effect of the probe on the background, differential measurements are performed. Therefore, the measured quantity will be the change in the probe signal with and without the presence of the pump beam. Geometrically speaking, the simplest way to measure changes in the probe beam consists in a transmission configuration.

To better explain the pump-probe signals, we will consider a three levels model containing the fundamental ground state and the first and second excited states. If the pump pulse is resonant with the $|0\rangle \rightarrow |1\rangle$ transition, the sample reaches the first excited state. From this state, two stimulated transitions are allowed: returning back to the ground state via stimulated emission (SE) or absorbing the probe photon and reach the second excited state in a process called photoinduced absorption (PA). A scheme of this model is shown in figure 1.19.

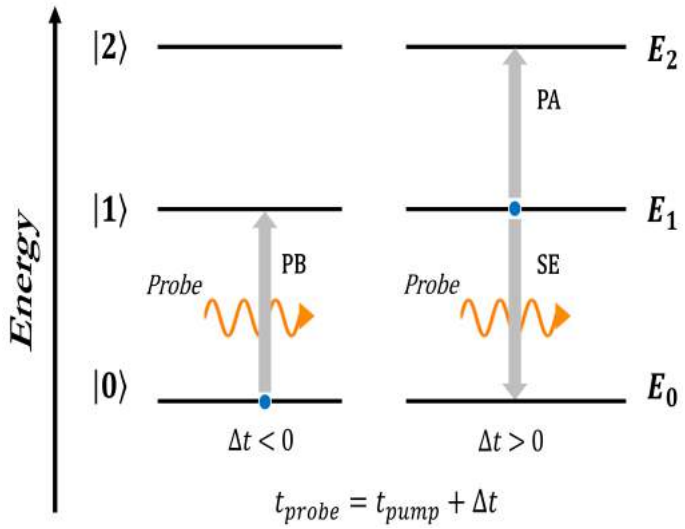

Figure 1.19: Pump-probe signals scheme at different probe arrival times. Photobleaching (PB), stimulated emission (SE) and photoinduced absorption (PA) signals are shown.

We can set differential changes in probe transmission with and without the pump as the magnitude to monitor ($\Delta T = T_{pump\ on}$-$T_{pump\ off}$). Once the pump excites the sample, less sample remain in the ground state so $T_{pump\ on} > T_{pump\ off}$ and ΔT photobleaching signal becomes positive. Once the fluorophore reaches an excited state after pump excitation, if the probe beam has the proper wavelength we can see stimulated emission (SE). Stimulated emission causes that more photons arrive to the detector, therefore $T_{pump\ on} > T_{pump\ off}$ and ΔT stimulated emission signal becomes positive.

Let's now consider $|1\rangle \rightarrow |2\rangle$ transition and a probe photon with the proper wavelength to cause that transition. If a probe photon arrives before the pump, it will not be absorbed and thus, it will reach the detector. On the other hand, the probe photon can be absorbed after pump excitation in a photoinduced absorption (PA) process. In summary, in PA $T_{pump\ on} < T_{pump\ off}$ so the overall ΔT signal remains negative.

In a more proper way, we can define transient absorption as the temporally resolved differential absorption signals previously mentioned. For this reason, a typical TA map measurement shows the intensity of the differential absorption signal as a function of time and wavelength. An example of a TA measurement map is shown in figure 1.20.

As a time-resolved technique, transient absorption allows to measure the differential absorption of the fluorophore as a matter of state population transitions. Assuming that the temporal overlap between pump and probe pulses is negligible, we can study differential absorption as the absorption defined by the Lambert-Beer law. In this sense, state transitions are described by the product of $\sigma\ (\lambda)$, the cross section for the transition and the concentrations of the fluorophore, $n(t)$, as state populations. Additionally, L and A represent the thickness and the absorbance of the sample, respectively.

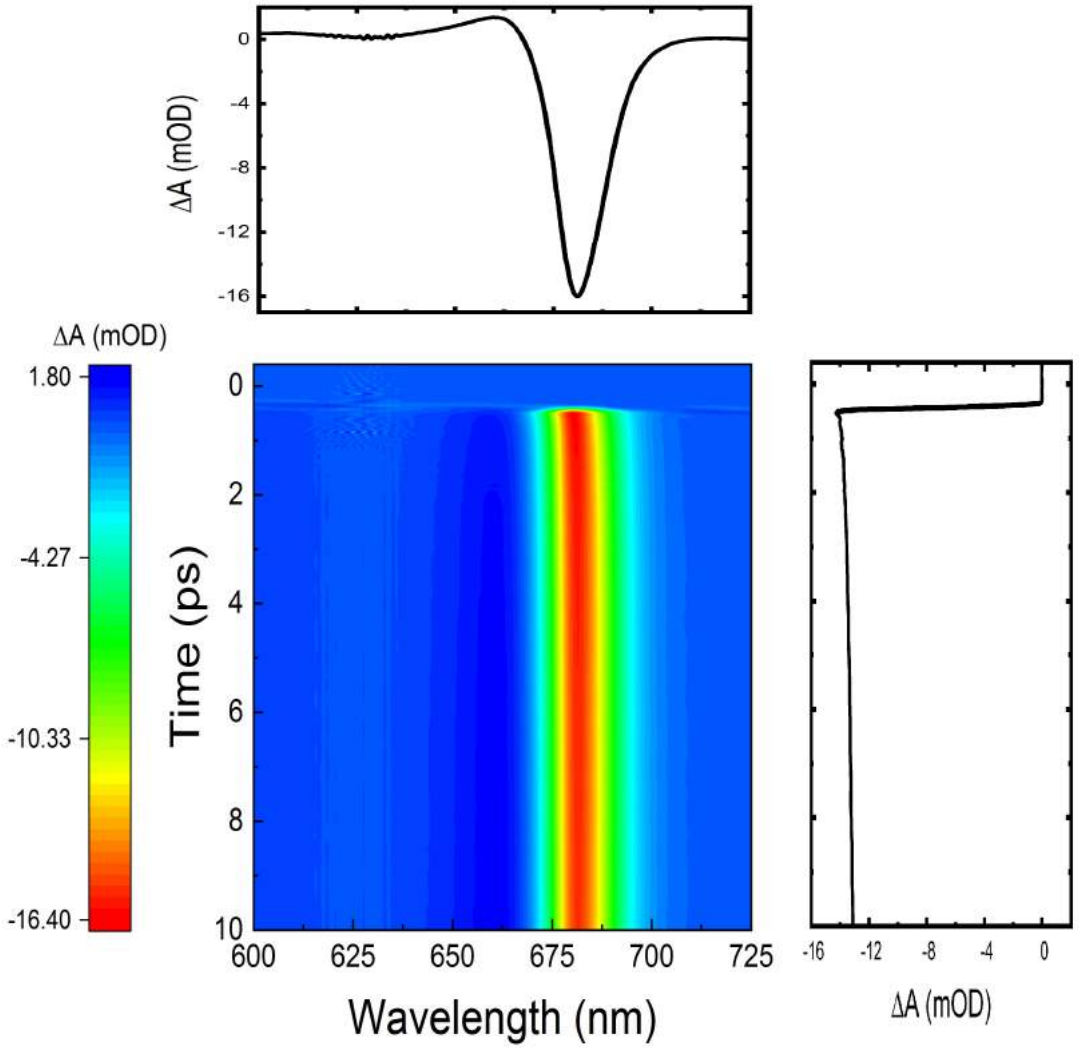

Figure 1.20: Transient absorption map of an *in vitro* LHCSR3 protein showing: (Upper panel) Spectrum integrated between 1 and 2 ps after excitation and (Side panel) kinetics integrated between 675 and 685 nm.

Lambert-Beer law is finally represented by the following expression:

$$\Delta A = \sigma(\lambda) n(t) L \tag{1.16}$$

Pump excitation causes changes in the absorbance of the sample, so we can consider ΔA=$A_{pump\ on}$-$A_{pump\ off}$. As this absorbance variation implies changes in individual states population, we can express Δn as Δn=$n_{pump\ on}$-$n_{pump\ off}$ and therefore equation 1.16 is rewritten as:

$$\Delta A = \sum_i \sigma_i(\lambda) \Delta n_i(t) L \tag{1.17}$$

Absorbance can be expressed as a function of the probe transmission by the formula A=-ln(T) so that the differential absorbance results:

$$\Delta A = -\ln(T_{pump\ \ on}) + \ln(T_{pump\ \ off}) \tag{1.18}$$

$$\Delta A = -ln\left(\frac{T_{pump\ \ on}}{T_{pump\ \ off}}\right) \tag{1.19}$$

$$\Delta A \approx -\left(\frac{T_{pump\ \ on}}{T_{pump\ \ off}} - 1\right) \tag{1.20}$$

$$\Delta A \approx -\left(\frac{\Delta T}{T_{pump\ \ off}}\right) \tag{1.21}$$

with approximation ln(x) $\approx$ x - 1 being used in equation 1.20. Defining $T_{pump\ off}$ as simply T and combining equations 1.17 and 1.21, we finally obtain:

$$\frac{\Delta T}{T} = -\sum_i \sigma_i(\lambda) \Delta n_i(t) L \tag{1.22}$$

Transient absorption measurements are usually performed with ultrashort pump pulses to increase the temporal resolution of the measurement itself. Secondarily, it is important to notice the detected probe intensity (regardless the detection system) will always be a convolution between the temporal profile of the pump pulse and the sample response, needing deconvolution to recover the true signal from the sample. Thus, the ultrashort pump pulses are also used to minimize the use of deconvolution. There are multiple detection systems for TA and, similarly to TRF detection, they can be classified into electronic and optical detection.

Electronic detection

Flash-photolysis In this case, a pulsed and tunable ps/ns laser is used as pump, while a continuous wave light source is used as the probe beam. In the most simplest scheme, the probe light is detected at a certain time (before or after excitation) by a fast photo-diode coupled to a oscilloscope. The signal intensity is then calculated as the difference of intensity of the probe pulse before and after the sample excitation.[86,87] In these setups, the temporal resolution is determined by the instrumental response function of the detector and they usually reach values of ≈10 ps.

Optical detection

fs pump-probe Here, the output of a fs laser is sent to a beam splitter to create both pump and probe beams. Different non-linear optic elements can be used to tune the wavelength of pump and probe to our requirements. Indeed, it is very common to use a single wavelength as a pump and a super continuum generated white light as a probe. The advantage of using such a probe lies in the fact that a broadband probe can be used to monitor several transitions at the same time. Pump and probe need to be temporally and spatially overlapped in the sample and while spatial overlap is achieved by simple alignment, the temporal overlap is reached thanks to an optical delay line. The transmitted probe intensity is finally registered thanks to a slow detector. The sample dynamics are built up by scanning several positions on the delay line.[88,89] The temporal resolution of this setups is usually ≈100 fs.

For the purposes of this thesis, we will use a fs pump-probe detection system for all TA measurements with the setup present in the physics department of Politecnico di Milano. The full description of the setup will be shown in chapter 2.

Chapter 2

Materials and Methods

In this chapter, we will focus on the experimental aspects of the performed measurements. A detailed description of the key elements and a general overview of the time resolved fluorescence and transient absorption setups is shown in sections 2.1 and 2.2, respectively. Section 2.3 is focused on data treatment, especially in a description of the global analysis fitting method.

2.1 Broadband TRF setup description

The time-resolved fluorescence setup present at the Center for Nano Science and Technology (CNST) is configured to deal with several different experimental conditions. In particular, it covers broadband excitation and detection ranges from the MUV to the visible and NIR (260-1400 nm) with a spectral resolution of few nm. Also, we can change the configuration to detect very fast processes in the ps-ns scale or slower processes up to μs and even ms. In addition, spatial resolution down to the μm can be reached by the use of a confocal microscope. The ability of using a wide broadband excitation wavelengths and its detection at different spectral and temporal ranges, alongside with a precise spatial resolution is what gives this setup a strong versatility and a huge range of measuring conditions.

In the following sections, we will see a setup overview, focusing on the elements that provide pump wavelength selectivity and high temporal, spectral and spatial resolution. An overall scheme of the optical layout is shown in figure 2.1

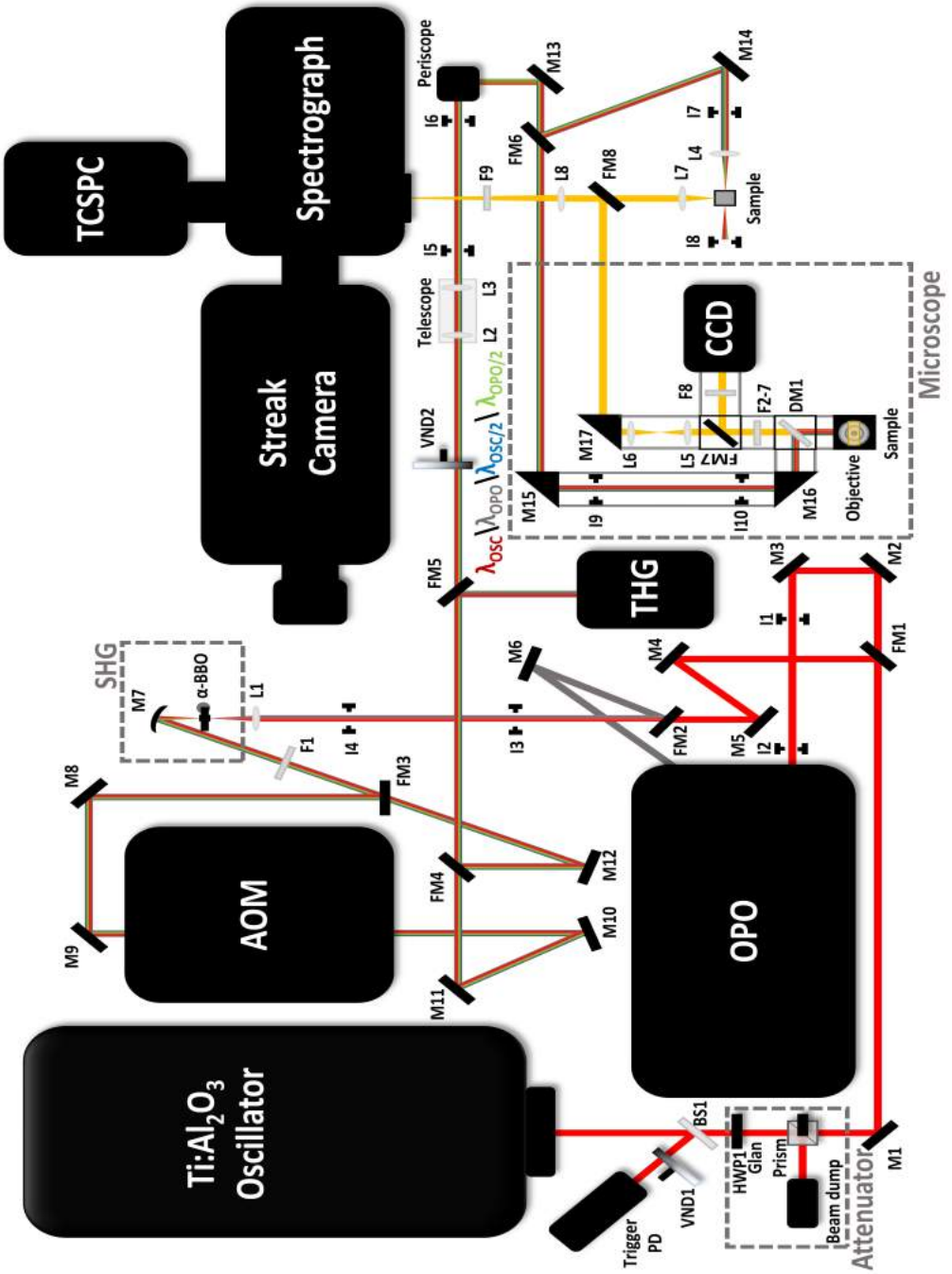

Figure 2.1: Time-resolved fluorescence setup overview. Abbreviated terms: beam splitter (BS), variable neutral density filter (VND), half-wave plate (HWP), steering mirror (M), flip mirror (FM), alignment iris (I), optical lens (L), absorbance filter (F), dichroic mirror (DM).

2.1.1 Wavelength selection

A commercial Ti:Al_2O_3 oscillator (Coherent Chameleon Ultra II) was used as the fundamental excitation source due to its tunablity in a wide range of wavelengths in the visible and NIR (680-1080 nm). Its output provides $sech^2$ pulses with a full width half maximum (FWHM) of ≈140 fs and a 80 MHz repetition rate.

A high power attenuator is placed right after the oscillator to control its power. Attenuator is composed of a broadband half-wave plate and an air-gap Glan-Taylor prism, which only let horizontally polarized light pass.

To increase the excitation range, a set of nonlinear optics based sub-systems were developed. The most entirety of the visible region was obtained via second harmonic generation (SHG) of the Ti:Al_2O_3 oscillator output. In order to obtain it, the beam is focused into a type-I alpha barium borate crystal (α-BBO) cut at 29.3°. An α-BBO is a birefringent material with a high $\chi^{(2)}$ nonlinear coefficient which allows high-order nonlinear effects. Rotation of the crystal axis with respect to the incident beam allowed us to achieve a broadband phase matching and a new spectral range of excitation from 340 to 540 nm. As SHG is not a fully efficient process (in this case, the maximum efficiency is around 10%), an absorbing filter must be placed afterwards to remove the residual pump.

To cover the NIR and the visible part of the spectrum that cannot be reached with the Ti:Al_2O_3 oscillator, we use a resonant NIR optical parametric oscillator (OPO). The OPO is pumped by the oscillator and generates pulses in the 1000-1400 nm region.

The OPO output can then be sent to a BBO crystal cut at 21.4° to fill the visible range gap left by the Ti:Al_2O_3 oscillator and its doubled-frequency spectra. As before, phase matching is achieved by rotating the crystal axis with respect to the incident beam. The final wavelength range obtained this way ranges from 500 to 700 nm.

Finally, the MUV range was achieved thanks to a third harmonic generation (THG) system optimized to work between 800 and 900 nm. The interaction between the oscillator fundamental and its doubled-frequency pulses generates a broadband spectra from 266 and 300 nm. The whole excitation spectrum of the setup is resumed in figure 2.2.

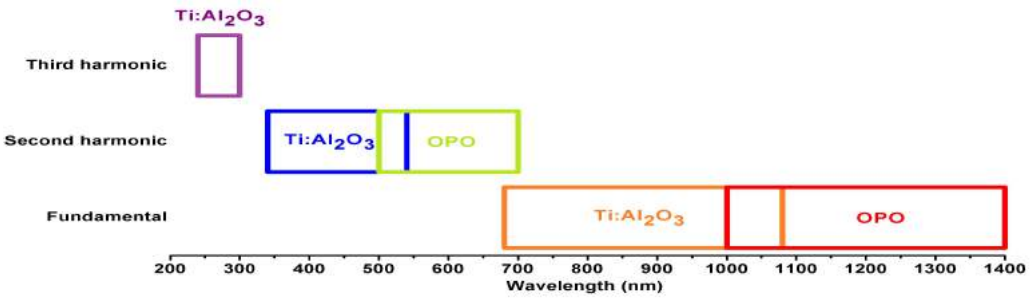

Figure 2.2: Full excitation spectra of TRF setup.

2.1.2 Excitation repetition rate selection

$Ti:Al_2O_3$ oscillator operates at 80 MHz, which means that pulse-to-pulse time is 12.5 ns. For long lived samples, this time can be too short and the second pulse can re-excite the system when it has not fully relaxed.

To avoid this, the repetition rate of the train pulse can be regulated by an acusto-optic modulator (AOM). In an AOM, light crosses a SiO_2 crystal and gets modulated when a radio-frequency transducer applies pressure on the crystal and diffracts the beam at specific times. An electronic control is then used to divide the train pulse in an integer multiples of 12.5 ns.

2.1.3 Spatial resolution

Spatial resolution was determined by the construction of a confocal microscope. The spot size was controlled by a telescope and the expanded beam was sent to a dichroic long pass filter as seen in figure 2.1. The reflected beam was then coupled to an objective and focused into a sample.

The emitted light, alongside with the excitation pump, travels the excitation path backwards until the dichroic filter, where the pump is reflected once more and the fluorescent light goes through the filter. As the absorbance below the operational wavelength is not exactly 100%, an additional long-pass filter can be placed after the dichroic filter to remove even more possible residual pump.

To determine the microscope field of view (FOV), a flip mirror was placed in the emission path after the dichroic mirror to send the emmited light to a CCD camera. Positioning and focusing on the sample can be achieved manually by moving the XYZ stage under the sample holder. A LED light over the objective is used to work on brightfield conditions.

Once the focusing position on the sample is reached, the flip mirror is removed to send the fluorescent light to a telescope, which collimates the beam. After that, a second flip mirror sends the light to the detection system.

2.1.4 Detection system

Depending on the range of wavelengths of the emitted light, the detection system will vary. For signals in the visible and MUV, a commercial streak camera system is used while for signals in the NIR range, a time correlated single photon counting (TCSPC) is chosen.

Excitation, excluding microscope measurements, was performed by focusing the pump beam to get a ≈100 μm spot diameter into the sample. The collection was then done at 90° respect to the excitation beam in order to avoid pump detection as much as possible. To suppress even more pump detection, carefully chosen long pass filters were placed just before the detection system.

Emitted light was then sent through a lens-based telescope with a collection solid angle of 0.14π sr to a commercial spectrograph which has two visible and one NIR diffraction gratings with different blazes (1501 mm^{-1}, blaze 300 nm; 1501 mm^{-1}, blaze 1200 nm; 501 mm^{-1}, blaze 600 nm) to provide broadband spectral resolution. A piezo-driven flip mirror can be used to select the detection system (streak camera or TCSPC).

Streak camera A streak camera is a device used to detect ultrafast light phenomena providing a time vs wavelength vs intensity image. Its operating principle is resumed in figure 2.3. The input light consists in a package of photons with different wavelengths (separated by the spectrograph seen in the previous section) which arrives at different times after excitation.

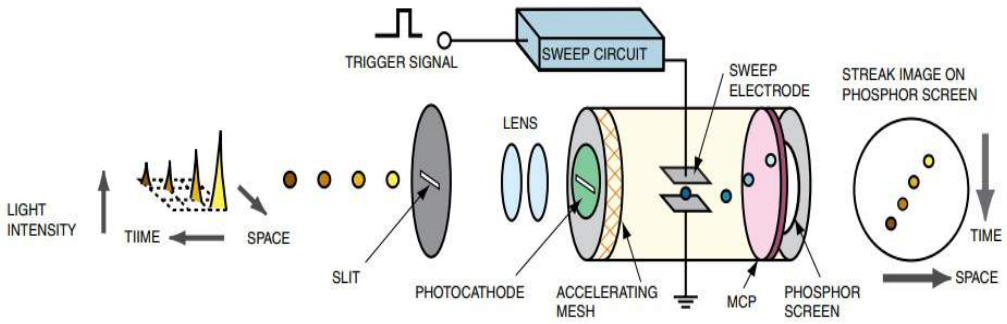

Figure 2.3: Streak camera operating principle. Image extracted from Hamamatsu operator manual.

Light crosses a slit and then, a pair of lenses focuses it into a photocathode, which will convert the incident photons into electrons almost instantaneously and proportionally to the intensity of the light. Electrons generated this way are then accelerated by a pair of electrodes and cross the streak tube.

In the middle of the tube, a time-dependent sweep voltage is applied between two electrodes and causes the deflection of the electrons generated in the photocathode. This sweeping temporal dependence allows to resolve the fluorescence light temporally as the electron deflection angle and path depends on the arrival time of the photons to the

sweep electrodes.

After the sweep, the electrons arrive at a micro-channel plate (MCP) in which they are multiplied several thousand times and sent to a phosphor screen to reconvert them into light. On the phosphor screen, pulses are sequentially ordered from top to bottom according to their arrival time. Those which arrived first will be placed on the top part and those which arrived later on the bottom. Finally, light is collected and the signal is digitalized thanks to a high-resolution CCD camera.

The timing of sweeping voltage is a crucial aspect to control as the sweep voltage is applied when the fluorescent light arrives to the streak camera. To synchronize both phenomena, the splitted beam right before the laser attenuator (see figure 2.1) is sent to a PIN photodiode and used as a streak camera trigger. Additionally, the delay between trigger and fluorescent light can be precisely tuned thanks to a delay generator unit coupled to a computer.

Streak camera includes both a synchroscan and slow sweeping units. The main difference between them is the nature of the time-varying voltage. Synchroscan unit performs a sinusoidal sweep and is used for measuring samples within a 2 ns time range with a 20 ps temporal resolution. On the other hand, the sweeping voltage in the slow sweep unit is mainly linear and is used for measuring samples with a temporal window greater than 2 ns, reason by which it is used in conjunction with the AOM.

TCSPC TCSPC detection was achieved using a NIR fast PMT coupled to a TCSPC card with a instrumental response function (IRF) of ≈1 ns. In order to correctly operate with the device, liquid nitrogen must be used to cool down the fast PMT. Triggering of the TCSPC signal was performed using the fundamental pump beam in the same way we saw before for the streak camera.

2.2 Transient absorption setup description

The transient absorption setup at the physics department of Politecnico di Milano was designed to work in a non-degenerate configuration. The main advantage of this type of configuration is that both pump and probe can be tuned in a wide range of wavelengths.

A commercial Ti:Al_2O_3 oscillator (Coherent Libra) operating at 800 nm was used as the fundamental light source. The output beam is composed of sech^2 pulses with a FWHM of ≈100 fs and 1 kHz repetition rate. Right afterwards, the beam size is regulated by a telescope and sent to a beam splitter to generate both pump and probe beams.

In this specific case, pump pulse is the output of a nonlinear optical parametric amplifier (NOPA) calibrated to work optimally in the visible and the probe pulse is a broadband generated via white light supercontinuum (WLC) generation in the visible or NIR, depending on the crystal used in this process. Probe detection is performed thanks to an optical multichannel analyzer (OMA) which works in both wavelength ranges. In the following sections, we will see a setup overview, focusing on the pump and probe

generation and the detection of the probe pulses. An overall scheme can be seen in figure 2.4.

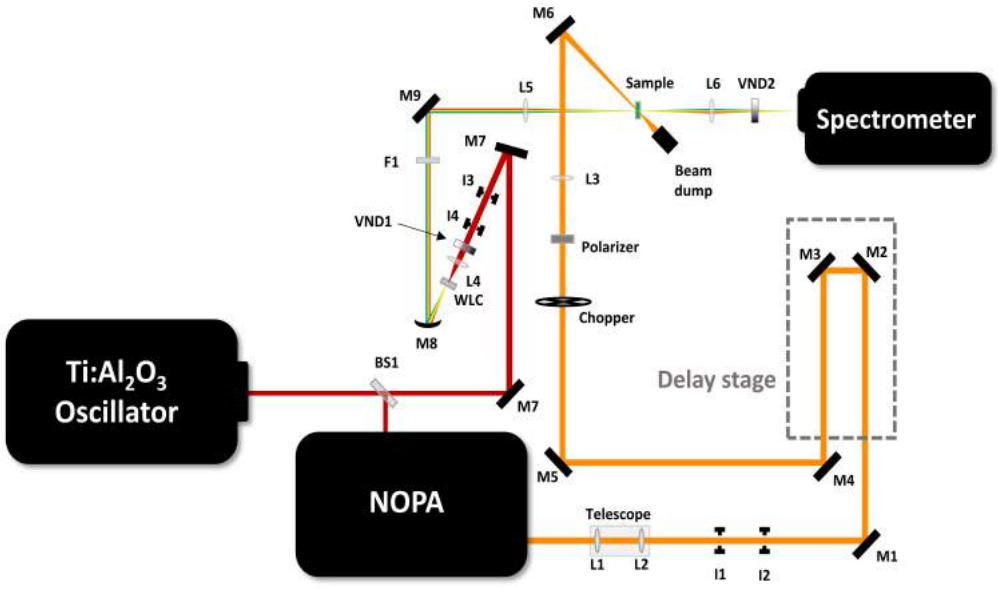

Figure 2.4: Transient absorption setup overview. Abbreviated terms: beam splitter (BS) optical lens (L), alignment iris (I), steering mirror (M),variable neutral density filter (VND), white light generation crystal (WLC), absorbance filter (F).

2.2.1 Pump pulse generation

The generation of the pump pulse is achieved thanks to a non-linear three wave mixing effect called optical parametric amplification (OPA). In OPA, a low frequency signal pulse, ω_s, is amplified by interacting with a strong second pump pulse, ω_p, with a frequency $\omega_p > \omega_s$. That interaction causes the amplification of the signal photon and generates a third photon called idler whose frequency will be determined by ω_p-ω_s. Also, this process only occurs if the momentum conservation (phase matching) is fulfilled (i.e., $k_p = k_s + k_i$). A scheme of the phenomenon is seen in figure 2.5

Pump generation was performed thanks to a custom-built NOPA whose overall description can be seen in figure 2.6. In this setup, the 800 nm beam from the oscillator is sent to a beam splitter, in which 10% is transmitted to generate the signal pulse and the remaining 90% is reflected and used to generate the pump pulse.

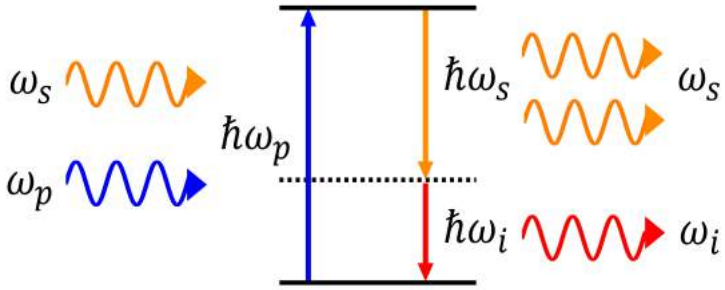

Figure 2.5: Optical parametric amplification process scheme.

The transmitted 800 nm is then attenuated and used to create the white light supercontinuum seed. After that, the seed is collimated by a spherical mirror and the signal wavelength is tuned at 630 nm using a proper bandpass filter.

On the other hand, the reflected 800 nm is sent to a type I α-BBO crystal cut at 29.2^o to generate the pump pulse at 400 nm. Once the pump is created, it is filtered to remove the residual 800 nm.

To generate the 630 nm amplification in the second type I α-BBO, pump and signal photons must overlap both spatially and temporally. Spatial overlap is achieved by simple alignment, while temporal requires the use of a translation stage for fine tuning in the pump pathway.

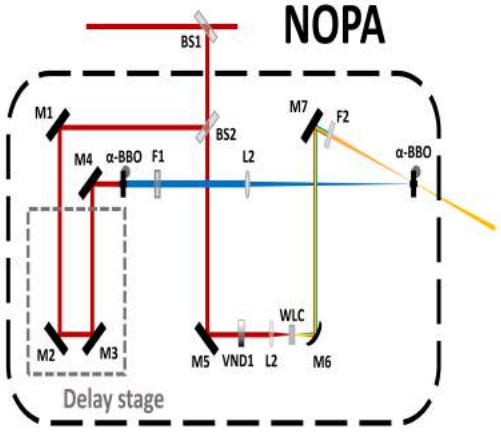

Figure 2.6: NOPA overview. Abbreviated terms: beam splitter (BS), steering mirror (M), optical lens (L), variable neutral density filter (VND), white light generation crystal (WLC), absorbance filter (F).

The amplified 630 nm beam is then enlarged with a telescope which doubles the spot diameter up to ≈400 μm and sent to the delay stage. After that, the beam is modulated mechanically with a chopper working at 500 Hz, its polarization is changed to a magic angle configuration (54.7°) and finally, it is focused into the sample.

2.2.2 Broadband probe pulse generation

Similarly to what we saw in the signal pulse generation of the NOPA, the generation of the broadband probe pulse is done exploiting the WLC generation effect. To achieve that, the transmitted part of the Ti:Al_2O_3 oscillator after the first beam splitter (see figure 2.4) is attenuated with a variable neutral density filter (VND) and focused with a proper lens into the thin WLC crystal. The white light generated this way is then collimated by a spherical mirror and crosses one or more bandpass filters in order to remove possible fundamental residuals and then focused into the sample.

Depending on the spectral range in which we want to generate the white light, different materials will be used as WLC crystals: a Ti:Sapphire plate provides us a visible broadband between 450 and 750 nm while a YAG does it in the 800-1150 nm region. Figure 2.7 shows the broadband probe generation achieved with the two different plates.

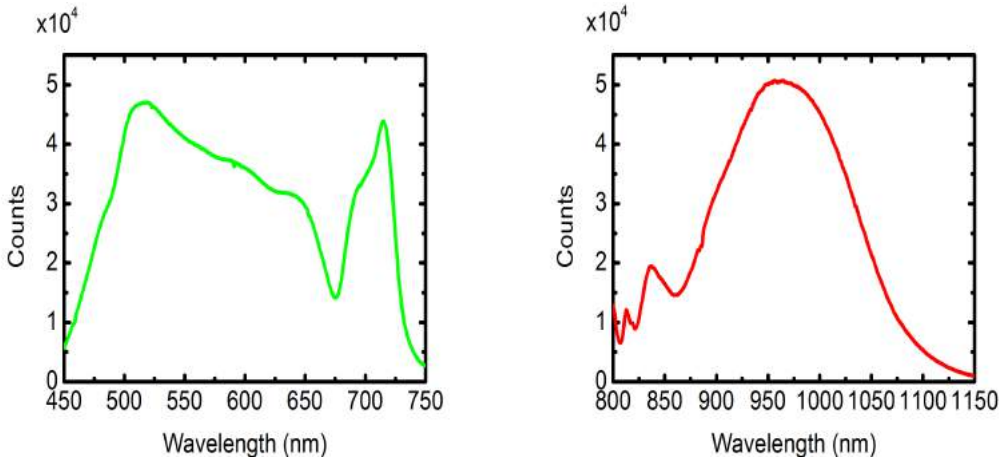

Figure 2.7: Spectra of probe pulses in the visible (left) and NIR (right) ranges given by WLC generation in Ti:Sapphire and YAG plates, respectively.

2.2.3 Detection system

Due to the fact that the probe pulse is broadband, its detection is carried out by a OMA optimized to work in the visible and the NIR. To perform this task, the OMA contains two controllable gratings with different blazes that disperse light on a linear CCD camera. OMA resolution is determined by the number of pixels on the CCD camera and the grating in use and usually this values is less than 1 nm. A brief scheme of an OMA can be seen in figure 2.8.

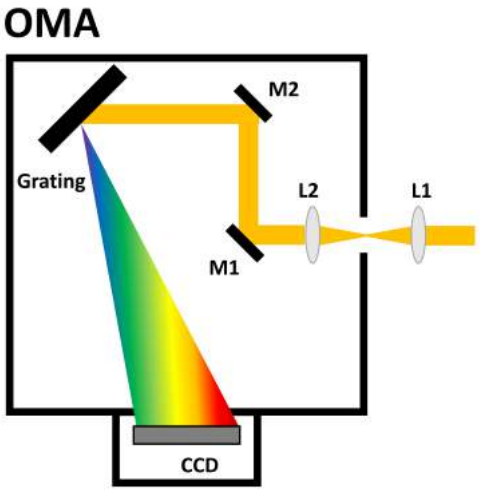

Figure 2.8: OMA overview. Abbreviated terms: optical lens (L), steering mirror (M)

2.3 Data processing

The main objective of time resolved spectroscopy is to measure the relative populations of the different states that conform the system under study to elucidate its dynamics. Normally, the system is complex and little information is known beforehand, which makes the analysis and results interpretation difficult. To solve this problem, we can use a powerful tool called global analysis.[90,91]

Global analysis is a fitting tool which uses least squares fitting with variable projection methods to recreate experimental data. Also, it requires a certain modelling and some reasonable initial assumptions based on the physics of our system. We will see the mathematics underlying this process and a description of its main features in the following sections.

2.3.1 Mathematical basis

Before establishing a model to describe the data, we have to make two assumptions that will simplify the analysis: we will consider the system homogeneous and separable.

Homogeneity It implies that we can consider a discrete set of parameters to describe the system instead of using distributed parameters, as it would happen in an heterogeneous system.

Separability It determines that the spectroscopic properties of a mix of components are the sum of its individual components spectroscopic properties weighted by their concentration.

In this sense, if a system is composed by a certain number of elements n_{comp}, we can consider its time-resolved measured map ψ as:

$$\psi(t,\lambda) = \sum_{l=1}^{n_{\mathrm{comp}}} c_l(t)\epsilon_l(\lambda) \tag{2.1}$$

Where $c_l(t)$ and $\epsilon_l(\lambda)$ represent the concentration and the spectrum of the component l, respectively.

In general, electronic transitions are described by first-order kinetics which means that populations follow first-order differential equations. Solution of a first-order differential equations system is a sum of exponential decaying functions, so in our case, equation 2.1 can be rewritten as:

$$\psi(t,\lambda) = \sum_{l=1}^{n_{\mathrm{comp}}} (exp(-k_l t) \circledast i(t))\epsilon_l(\lambda) \tag{2.2}$$

In which $c_l(t)$ is the result of the convolution between the exponential function containing k_l, the rate of the exponential decay of component l, and $i(t)$, the instrument response function (IRF) of the detector. The final goal is, then, to obtain the value of these parameters from the experimental data.

2.3.2 Global analysis

Once we have a time-resolved experimental dataset which is homogeneous and separable, we can start a global analysis. First of all, we need to reasonable estimate the number of components n_{comp} we will consider in our analysis. It is recommended to have previous knowledge of the system to determine n_{comp} but in the case we are not sure about the nature of the system, we can apply the Singular Value Decomposition (SVD) theorem to get this information.

SVD theorem is based in the fact that we can determine that any m $\times$ n matrix has a singular value decomposition represented by the formula:

$$\Psi_{m\times n} = U_{m\times m} S_{m\times n} W^T_{n\times n} \tag{2.3}$$

Where U and W are orthogonal matrices containing the left and right singular vectors and S is a diagonal matrix which contains the singular values or eigenvalues.

These eigenvalues give us a very good estimation of the number of components of our system, as their values are always non-zero. In this sense, considering again our system with $\mathrm{n_{comp}}$ components, the magnitude of the eigenvalues will be: $s_1 \geqslant s_2 \geqslant ... \geqslant s_{\mathrm{n_{comp}}} > 0$, with next term being $s_{\mathrm{n_{comp+1}}} = 0$.

Unavoidably, due to experimental conditions, it is not so easy to determine the exact point in which the magnitude of the eigenvalue is different from the noise, so in that case, we have to look at the left singular values and determine if it can contain relevant data or it is just regular noise.

With the number of components already set, we have to establish a model which will describe our data. In our case we will consider an unidirectional kinetic model in which the components decay sequentially and populate the following state one after the other with increasing lifetimes until the last one, which decays back to the ground state ($1 \rightarrow 2 \rightarrow ... \rightarrow n_{comp}$). Additionally, we have to consider some features to do a proper analysis. In particular, we have to correct the parabolic frequency chirp induced by white light generation, the instrumental response function and some coherent artifacts generated right after time zero.

Once all the parameters we need to recreate our data are set, we will start our global analysis with a series of initial values for all the variables and fit our data using an iterating least squares fitting algorithm. If the analysis is successful, we will obtain the time constant (k_l) and the spectrum (ϵ_l) for each l component. The collection of all ϵ_l spectra is called Decay Associated Spectrum (DAS) and graphically show us the evolution of the system. Overall, we can resume a global analysis in the steps resumed in figure 2.9

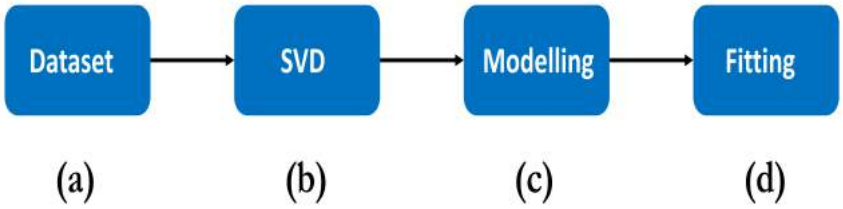

Figure 2.9: Global analysis diagram. *(a)*: Dataset selection, *(b)*: Number of components selection after singular values decomposition, *(c)*: Modelling, *(d)*: Fitting.

To illustrate this process, let's consider a practical case. The dataset we will use corresponds to a transient absorption measurement in the visible of a LHCSR3 sample after selective chlorophyll excitation at 630 nm. Its 2D map is shown in figure 2.10.

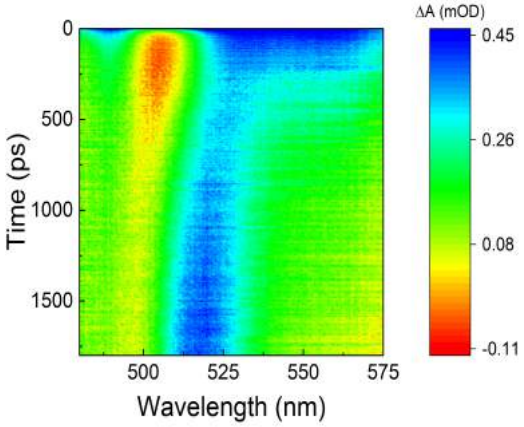

Figure 2.10: Visible LHCSR3 dataset (480-575 nm) obtained after excitation at 630 nm.

This map is characterized by a negative ΔA signal appearing at short times and a positive increasing signal appearing at longer times. At this point, we could argue that our system can be described by two components but, to be more precise, we will have a look at the eigenvalues of each component after singular value decomposition (SVD) and its respective left and right singular vectors. This process is shown in figure 2.11.

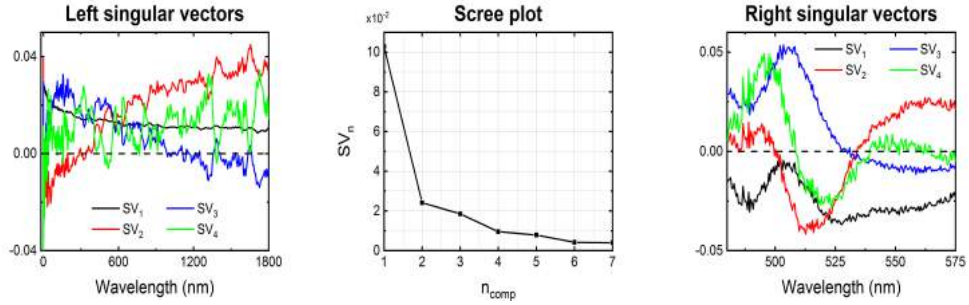

Figure 2.11: Selection of the number of components. *(Left)*: Left singular vectors, *(Center)*: Eigenvalues after SVD, *(Right)*: Right singular vectors.

The scree plot (a line plot of the eigenvalues, figure 2.11, center) shows a strong contribution of the first eigenvalue and a minor contribution of the second, third and possibly fourth eigenvalues. To finally set the number of components our global analysis will have, we observe the left singular vectors (figure 2.11, left). Here, we see clear dynamics for the first three eigenvalues as opposed to the fourth one, which seems to be just noise. Therefore, our model will consider three time constants.

To complete our modelling, we have to correct the WLG-induced frequency chirp using a quadratic polynomial function centered in a specific wavelength and set values to correct the distortions at early times produced by the IRF and coherent artifacts.

We then run our analysis and after several iterations, we fitted our dataset with three time constants and obtained its decay-associated spectra (DAS). Results are shown in figure 2.12.

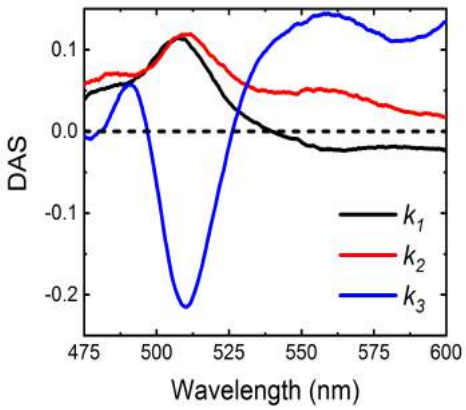

Figure 2.12: LHCSR3 DAS in the visible (480-575 nm) obtained after excitation at 630 nm.

The DAS (figure 2.12) shows what we expected from the TA map (figure 2.10): we are working with a short ΔA component and a second one that arises at longer times. Due to the huge similarities between the first and the second DAS, we could argue that the first process is biexponential (including k_1 and k_2) while the second one is a monoexponential (k_3).

Finally, we can estimate how good our global fitting is by comparing the fitted results with the original experimental data. A spectral and kinetic comparison of our fitting and the experimental data at 200 ps and ≈505 nm can be seen in figure 2.13.

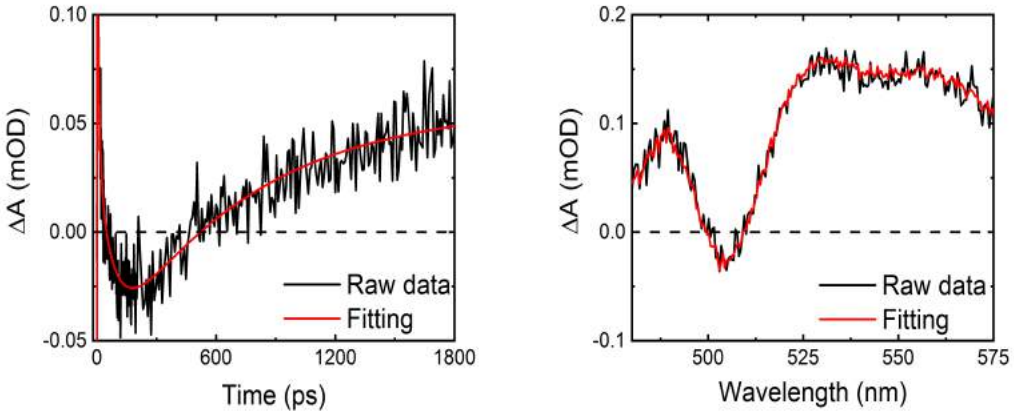

Figure 2.13: Experimental-fitted data comparison. *(Left)*: Kinetics at ≈505 nm, *(Right)*: Spectra at 200 ps after excitation.

From figure 2.13, we can see that our analysis fits the spectra and the kinetics accurately, so we can conclude that our global analysis was successful.

There are multiple software to perform global analysis but in this case, we used a Java-based software package created by professor Ivo H. M. van Stokkum in VU University Amsterdam called Glotaran. More detailed information about this program and how to use it can be seen in their work.[92]

Chapter 3

Non-photochemical quenching on wild type *Chlamydomonas Reindhartii*

In this chapter, we will focus on the spectroscopic features of *in vitro* LHCSR3 protein of wild type algae *Chlamydomonas Reindhartii*. Section 3.1 will show the state of the art of the studies on LHCSR3 from different algae. Section 3.2 will be focused on the experimental results obtained using time-resolved fluorescence (TRF) and transient absorption (TA) techniques on samples under different experimental conditions. Finally, section 3.3 is dedicated to the discussion of the results.

3.1 Background

As previously said in chapter 1, LHCSR3 constitutes a key element in *C. Reinhardtii* photoprotection as it is used as a pH sensor and as a NPQ trigger. Its NPQ triggering properties are due to interactions between the different pigments bound to it, mainly chlorophylls and carotenoids. However, despite knowing that its bounding molecules play a key role in photoprotection, there is not a full consensus about the exact molecular mechanisms underlying this process.

Throughout the years, several non-exclusive mechanisms have been proposed, all of them starting with a fast quenching of ^{1}Chl*, but while some of them consider an intense Chl-Chl coupling leading to charge transfer states as the main quenching reason,[93,94] the vast majority support the idea of a Chl-Car interaction.

Chl-Car interaction is explained through three mechanisms. The first one is based on energy transfers from excited ^{1}Chl* state to carotenoid short-lived dark states. In particular, several studies detected a ^{1}Chl* $\rightarrow$ Car S_1 state energy transfer[95–99] and, more recently, a ^{1}Chl* $\rightarrow$ Car S_q state[100] was observed. The second Chl-Car mechanism would involve an electron transfer between the Car and the photoexcited Chl, resulting in the formation of a Car radical cation and a Chl radical anion.[101,102] Finally, the third

mechanism consists in a Car-Chl excitonic coupling in which the coupled state acts as a quencher.[103]

Nevertheless, the main topic of debate is the nature of these carotenoids and which role the xanthophyll cycle plays in photoprotection. In this sense, a study carried out *in vitro* in *Physcomitrella Patens*[104] revealed the existence of both a zeaxhantin-dependent and a zeaxhantin-independent quenching mechanisms happening at the same time in LHCSR1. This work concluded that, when zeaxanthin was involved as a quencher, the main energy dissipation mechanism was a ^{1}Chl* $\rightarrow$ Car S_1 energy transfer while when zeaxanthin was absent, the formation of a Car radical cation was favored. Same results were observed more recently *in vivo* in the microalgae *Nannochloropsis oceanica*[105] in presence of a LHCSR-like protein, LHCX1.

In the case of *in vitro* LHCSR3 in *C.Reinhardtii*, the presence of zeaxanthin was proven to be unnecessary for NPQ induction[106] as the most probable quenching mechanism is the formation of a Car radical cation, triggered especially at low pH. Results of this study agree with previous studies in the same molecule[104] but also bring the question about what the quenching mechanism of LHCSR3 *in vivo* is.

Experiments performed on LHCSR3 *in vivo*[105,107] and on the supercomplex PSII-LHCII-LHCSR3 *in vitro*[108] showed a fast quenching in the ten to hundred of ps timescale, in contrast with the ns fluorescence decay that was seen in isolated *in vitro* LHCSR3 before.[104,106] These results suggest that the protein environment around LHCSR3 is another quenching factor to take into account.

A more complete analysis on *C. Reinhardtii* LHCSR3 was performed by Ballottari et al. as they studied the behavior of a LHCSR3 variant *in vivo* and *in vitro* under different protein aggregation conditions.[76] They observed the fast quenching on the *in vivo* sample and, interestingly also on *in vitro* samples, but only in strong protein aggregation conditions. In summary, all the experiments performed so far in LHCSR3 *in vitro* demonstrate that the two main quenching factors in this protein are pH and protein aggregation.

3.2 Experimental results

3.2.1 Sample preparation and characterization

LHCSR3 coding sequence (CDS) was amplified using high light adapted *C. Reindhardtii* complementary DNA (cDNA) and then cloned into a petMHis expression vector. Competents BL21 *Escherichia coli* cells were used to overexpress LHCSR3 which was later purified as inclusion body. Finally, it was refolded *in vitro* with pigment addition to get the final LHCSR3 holoprotein as previously reported.[109] Pigment composition of the refolded protein can be seen in table 3.1.

Pigment	**Chls**	Chl a	Chl b	**Cars**	Vio	Lut
Amount	8.00	6.98	1.02	2.44	1.60	0.84
σ		0.03	0.00		0.14	0.08

Table 3.1: Refolded LHCSR3 pigment analysis

pH was controlled using 20 mM solutions of commercial pH 7.5 or pH 5 HEPES buffers to get the final pH. Aggregation was controlled by the selective addition of a 0.03% n-dodecyl-α D-maltoside (α-DM) detergent solution so that two aggregation states were simulated: one with less aggregation in which the amount of detergent is high (0.03%) and another with more aggregation in which the detergent quantity is lower (0.003%). For simplicity, these two aggregation states will be referred in the future as HD (High Detergent) and LD (Low Detergent). LHCSR3 was then characterized by steady-state absorption spectroscopy. Results of this analysis are shown in figure 3.1.

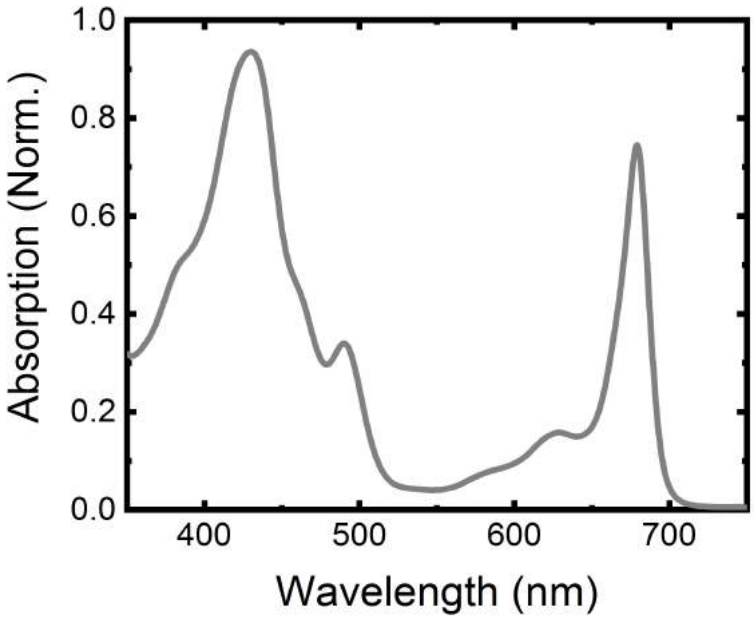

Figure 3.1: Steady-state absorption spectrum of LHCSR3 at room temperature.

We observed two distinctive Chl a absorption bands: The Soret band, peaking at ≈430 nm and the Q_y band peaking at ≈680 nm. It is also remarkable the appearance of a higher vibrational band of the Q_y state at 630 nm and a signal at ≈490 nm due to carotenoid contribution.

LHCSR3 was further characterized using steady-state fluorescence spectroscopy. Figure 3.2 shows the results on all four samples at different excitation wavelengths.

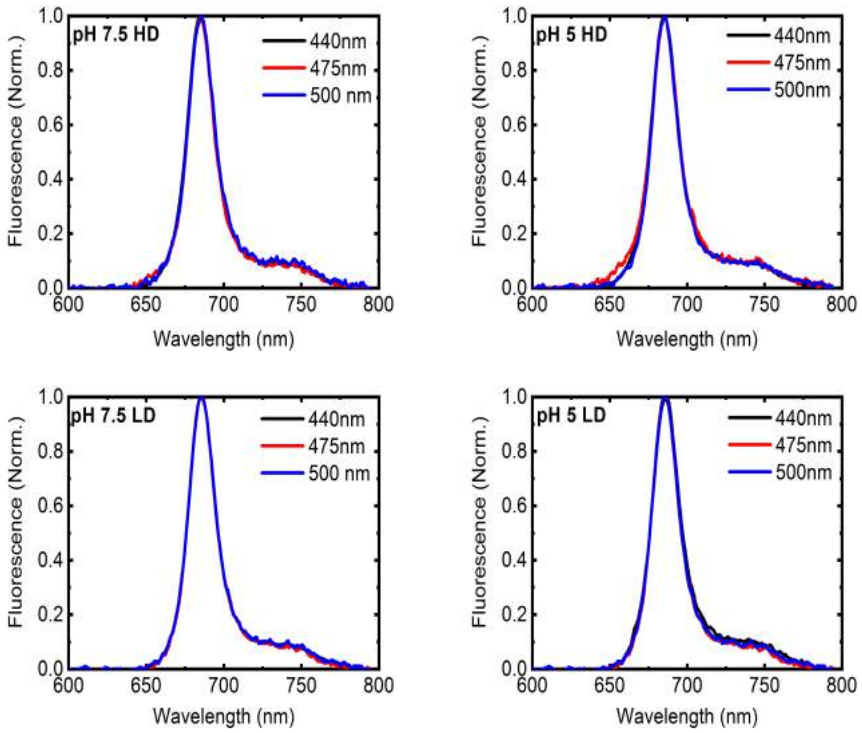

Figure 3.2: Steady-state emission spectra for all samples at different excitation wavelengths (440, 475 and 500 nm).

For all samples, we observe the typical Chl a fluorescence emission range between 650 and 800 nm, with a peak at 685 nm and a shoulder around 725 nm, regardless the excitation wavelength. In theory, changes in the pH of the medium can induce protein aggregation so we performed steady-state fluorescence spectroscopy at 77 K. Spectra for all samples are shown in figure 3.3.

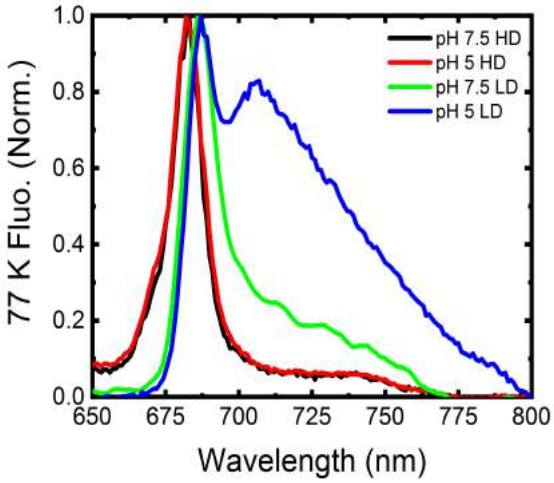

Figure 3.3: Steady-state emission spectra for all samples at 77 K.

A rising in the far-red part of the spectrum is observable only in LD conditions and matches with the formation of oligomers. As expected, detergent concentration is the main actor in aggregation induction and the effect of pH is relegated to a second place, only seeing a noticeable difference in high quenching conditions (LD). In addition, this non-pH dependency in HD conditions can be exploited for controlling the effect of pH alone.

3.2.2 Time resolved fluorescence measurements

Time-resolved fluorescence (TRF) analysis were carried out in the setup described in chapter 2. We chose 430 nm as the excitation wavelength to match the Soret band absorption. As this wavelength is obtained after SHG of a 860 nm fundamental excitation source, we need to remove the residual pump light by placing a longpass filter with a cutoff at 700 nm (BG40). After the sample, we placed a longpass filter with a cut off at 495 nm (LP495) to remove the residual 430 nm excitation light. Temperature was set at ≈12°C to avoid thermal protein denaturalization. Experimental TRF maps for all samples can be seen in figure 3.4.

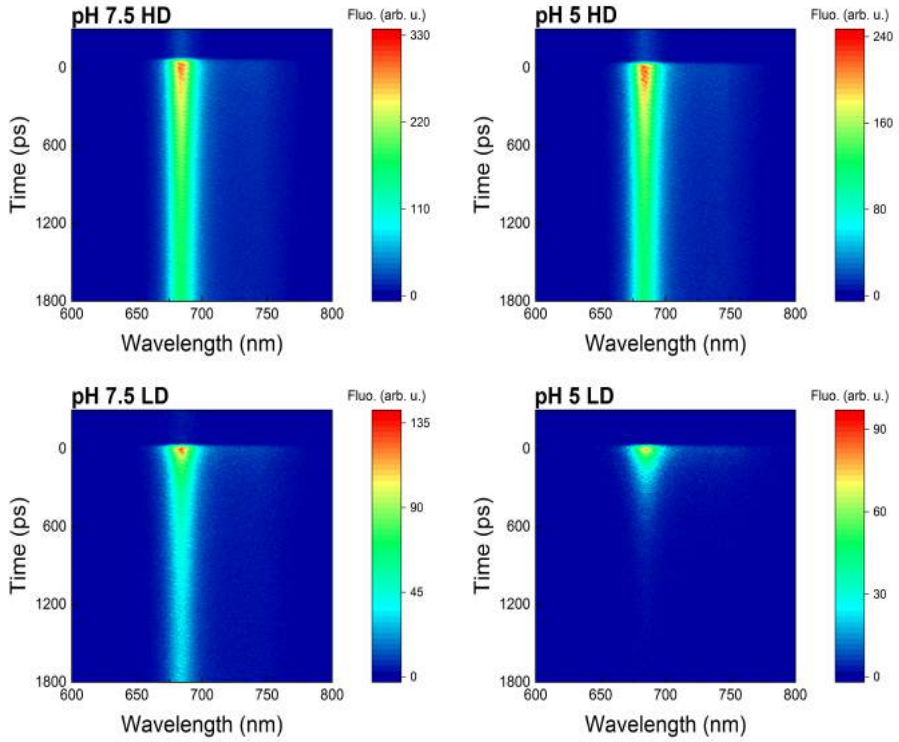

Figure 3.4: TRF maps of LHCSR3 in different quenching conditions after excitation at 430 nm.

We integrated experimental data over the full temporal window to get spectra for all samples whereas we integrated the data between 650 and 760 nm to obtain their kinetics. Results can be seen in figure 3.5

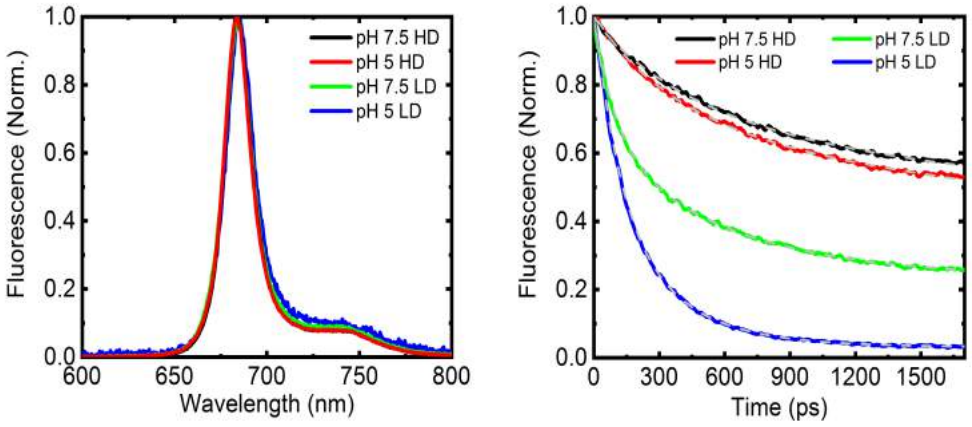

Figure 3.5: Time-resolved spectra *(left)* and kinetics *(right)* of all LHCSR3 samples at ≈12°C. Fitted traces shown as dashed gray lines.

From figure 3.5, aggregation is the main factor that affects lifetime quenching as LD samples show a faster decay than HD ones. pH also has a role in overall quenching, being faster those samples with a lower pH. The fact that pH-induced quenching is stronger in LD samples than HD suggests that pH has a secondary role in quenching as previously reported.[74] Results of biexponential kinetic fitting curves and the calculus of the average decay time ($\tau_{avg}=\Sigma A_l \tau_l$) are shown in table 3.2.

	$\mathbf{A_1}$ (%)	τ_1 (ps)	$\mathbf{A_2}$ (%)	τ_2 (ps)	τ_{avg} (ps)
pH 7.5 HD	48	593	52	8132	**4506**
pH 5 HD	51	521	49	7574	**3962**
pH 7.5 LD	58	184	42	2655	**1222**
pH 5 LD	59	119	41	330	**206**

Table 3.2: LHCSR3 biexponential fitting results for all samples.

These measurements point out a clear aggregation and pH dependence in LHCSR3 lifetime and establish a well defined pattern: the lower the pH and detergent concentration, the more quenched the sample is. However, all these features does not provide any insights of the molecular mechanisms that explain this process so further measurements are required.

3.2.3 Transient absorption measurements

Transient absorption measurements were carried out with the setup described in chapter 2. The pump wavelength was set at 630 nm to selectively excite chlorophyll a, as this wavelength matches the higher vibrational band of the Q_y state and carotenoids does not absorb at this wavelength. The probe beam consisted in a broadband white light between 450 and 750 nm. Pump beam was mechanically modulated by a chopper and its polarization was set at 54.7°. Sample temperature was set at ≈12 °C to avoid protein degradation. TA maps and spectra at 100 ps after excitation for all samples are shown in figure 3.6 and 3.7, respectively.

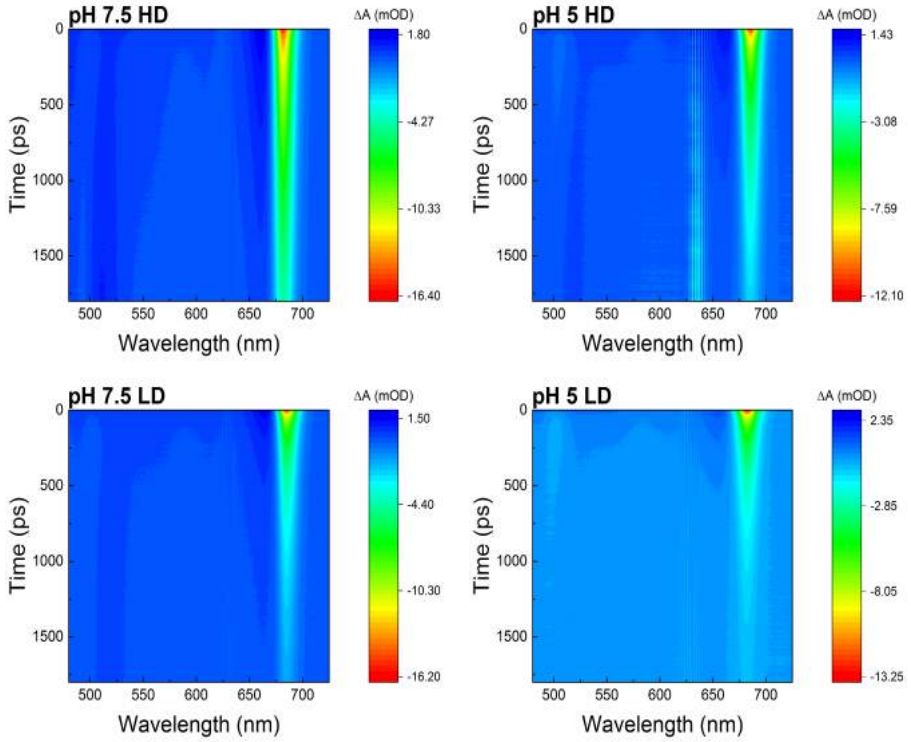

Figure 3.6: Visible TA maps of LHCSR3 in different quenching conditions after excitation at 630 nm.

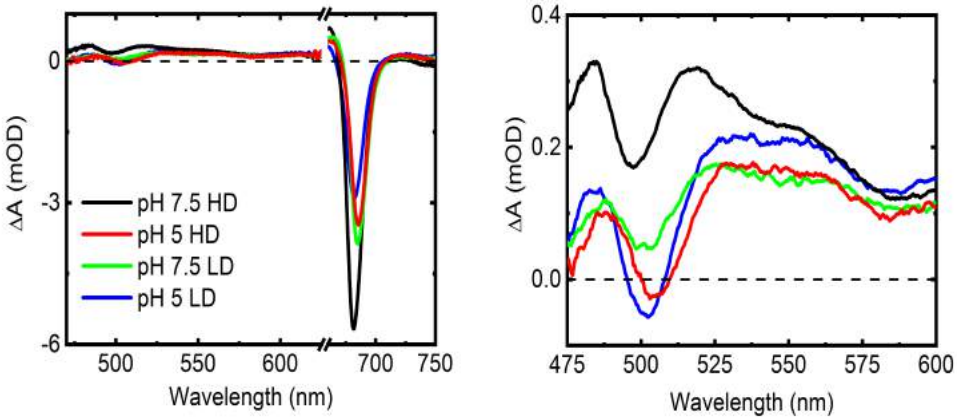

Figure 3.7: TA spectra of LHCSR3 at 100 ps after excitation at 630 nm for all samples. *(Left)* Whole spectral range. *(Right)* Closeup to the 475-600 nm region.

At early times, we see a series of signals in all samples: a negative signal at ≈680 nm corresponding to the Chl a ground state bleaching (GSB) and its stimulated emission (SE), a broad positive signal from 470 to 600 nm due to ^{1}Chl* photoinduced absorption (PA) and a residual part of the scattered pump at 630 nm. However, it is important to

notice that these signals kinetics can be distorted if we work in high fluence conditions due to a nonlinear effect called singlet-singlet (S-S) annihilation.[110]

As LHCSR3 protein has multiple pigments connected, high fluence light can cause the excitation of many chlorophyll a molecules. If two of these excited chlorophylls interact, one chlorophyll can transfer its energy to the second one and promote it to a higher excited state that rapidly decays to original excited state, annihilating one exciton in the process. A brief scheme of this process can be seen in figure 3.8.

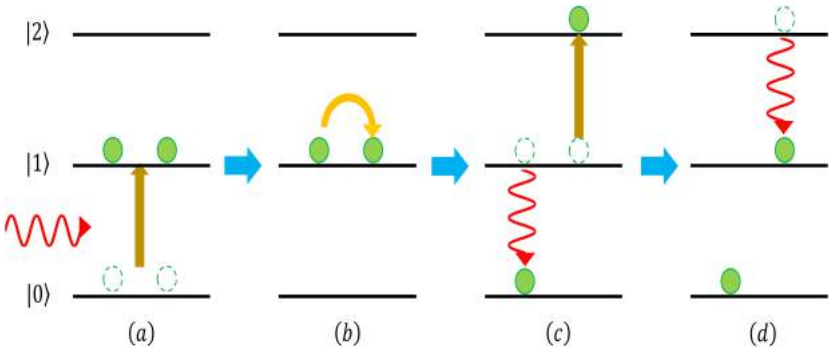

Figure 3.8: Singlet-Singlet annihilation process: (a) excitation, (b) energy transfer, (c) electronic states transitions, (d) relaxation.

Considering this, we did fluence dependence measurements to further work on S-S annihilation-free conditions. Figure 3.9 shows the kinetics of chlorophyll a GSB at 680 nm of pH 5 LD sample at different fluence values.

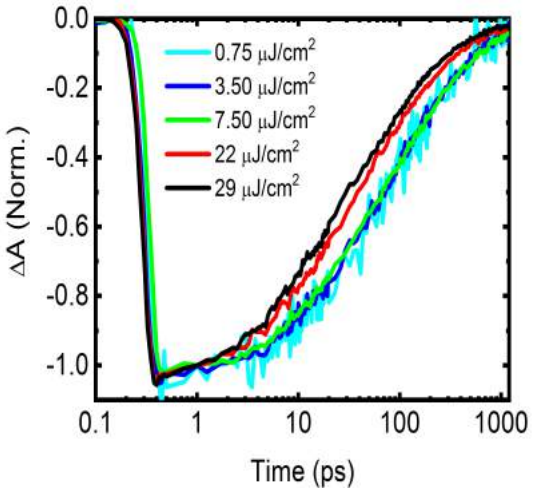

Figure 3.9: Fluence dependence of Chl a GSB dynamics at 680 nm for the pH 5 LD sample.

We see the kinetics-distorting effect of S-S annihilation at fluences higher than 20 $\mu J/cm^2$, so we set a value of 6 $\mu J/cm^2$ in all of our measurements. With a safe fluence value set, we studied the Chl a GSB dynamics. Figure 3.10 left shows the spectra of all samples at 100 ps after excitation while figure 3.10 right indicates the kinetics of chlorophyll a GSB at ≈680 nm for all samples.

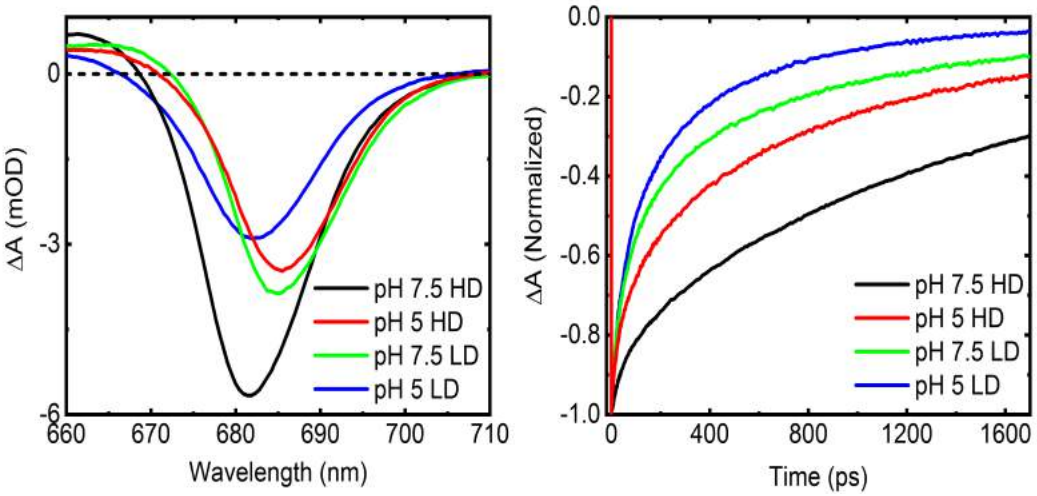

Figure 3.10: *(Left)* LHCSR3 TA spectra of Chl a GSB of all samples, *(Right)* LHCSR3 TA kinetics of Chl a GSB of all samples.

We observe similar results as those from TRF: aggregation constitutes the main quenching factor in Chl a GSB as LD samples present a shorter lifetime than HD ones. On the other hand, pH plays a secondary but significant role in the overall Chl a lifetime, showing a shorter lifetime for the samples at pH 5 as opposed to those at pH 7.5. Nevertheless, TA data shows a fast component in the pH 5 HD and LD samples which is not resolved in TRF due to its lower temporal resolution (20 ps in TRF against 100 fs in TA).

As Chl-Car interaction constitutes the basis of most of qE mechanisms, we focused on the 470-575 nm region. TA maps for all samples in this region are shown in figure 3.11.

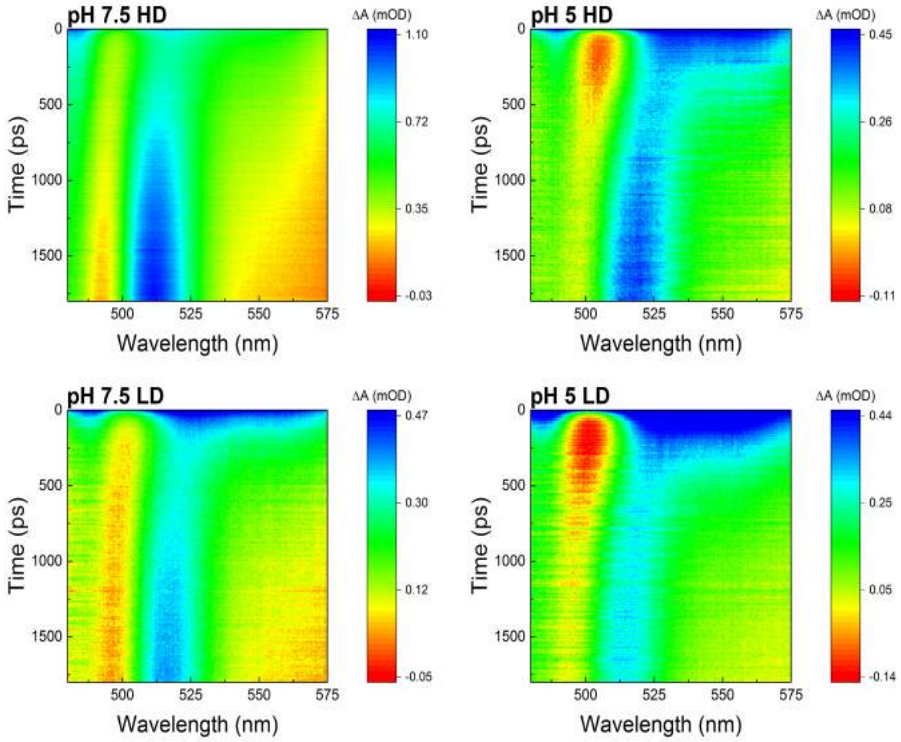

Figure 3.11: Visible TA maps of LHCSR3 in the carotenoid region (470-575 nm) in different quenching conditions after excitation at 630 nm.

In figure 3.11, we can see two main spectral features that are common for all samples: a ΔA minimum at around 500 nm at early times which is more evident at pH 5 LD (as it has a strong ΔA negative value) and a maximum placed at 510 nm at longer times, specially noticeable at pH 7.5 HD conditions. These two signals cannot be due to the mentioned broad PA of ^{1}Chl* exclusively, as PA alone does not explain why we find a negative signal at early times and also why the positive signal at 510 nm increases with time.

The fact that 500 nm matches the 0-0 peak of the Car $S_0 \rightarrow S_2$ transition allows us to assign this signal to a Car GSB. Likewise, the signal at 510 nm can be attributed to the absorption of the carotenoid excited triplet state, ^{3}Car*, as previously observed.[95,104,111] Chlorophylls and carotenoids coupling is produced immediately after Chl a excitation and can be explained as an ultrafast electrochromic shift of the carotenoid S_2 state.[103,104,112,113] This effect resembles a time-resolved Stark effect in which the local electric field changes produced by the excited chlorophylls is sensed by the carotenoids and induces a blue shift on the carotenoid S_2 state. Focusing on the Car GSB, figure 3.12 shows the transient absorption spectra of pH 5 LD sample at different times alongside the kinetics at 500 nm for all samples.

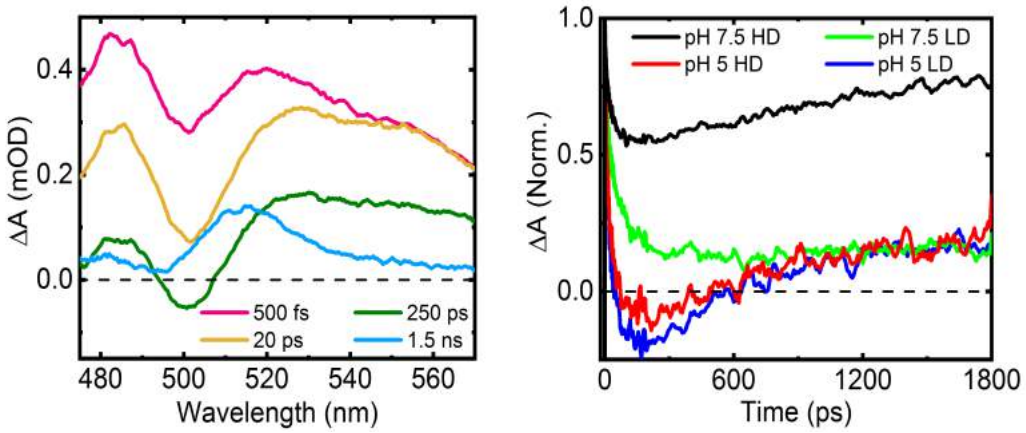

Figure 3.12: TA data of LHCSR3 after excitation at 630 nm. *(Left)* spectra of pH 5 HD at different times, *(Right)* normalized kinetics at 500 nm, showing the Car GSB. All kinetics were normalized at ≈500 fs after excitation.

In all samples (see figure 3.12 right) we see a buildup of the Car GSB in the first hundreds of picoseconds which is more evident in the pH 5 samples as the TA signal turns positive. At pH 5, the Car GSB signal is strong enough to prevail over the Chl a PA and provokes the change of sign as opposed to pH 7.5 conditions. Overall, we see a marked pattern in carotenoid GSB as more carotenoids bleach the lower the pH and the higher the aggregation are. Remarkably, at late times we see a rising of the ΔA signal due to the overlap of Car GSB signal with the Car triplet formation. Figure 3.13 shows the transient absorption spectra of pH 7.5 HD sample at different times and the kinetics at 510 nm for all samples.

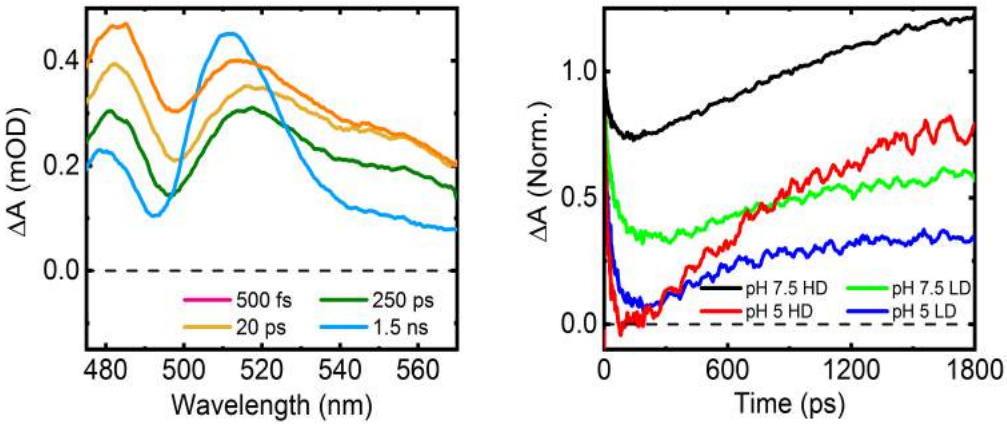

Figure 3.13: TA data of LHCSR3 after excitation at 630 nm.*(Left)* Spectra of pH 7.5 HD at different times. *(Right)* Normalized kinetics at 510 nm, showing the Car triplet formation. All kinetics were normalized at ≈500 fs after excitation.

For all samples, we observe the formation of a PA signal at ≈510 nm on the long timescale (see figure 3.13 right), corresponding to the absorption of ^{3}Car*. As we saw in chapter 1, carotenoid triplet state is populated via ^{3}Chl*-^{3}Car* energy transfer after chlorophyll intersystem crossing (ISC) according to the scheme ^{1}Chl* → ^{3}Chl* → ^{3}Car*. Hence, the longer the population remains in the ^{1}Chl* state, the more efficient the ISC will be and subsequently the more ^{3}Car* will be formed. This is exactly what we see in our experimental data as the pH 7.5 HD sample (which was the one with the longer Chl decay lifetime, figures 3.5 and 3.11) forms more carotenoid triplet than the pH 5 LD sample (the most quenched one, figures 3.5 and 3.9).

One possible quenching mechanism of the chlorophyll excited state consists in an energy transfer from the ^{1}Chl* to the Car S_1 state. S_1 is a dark state, which implies that we cannot see directly its PA from the Car ground state. However, we can detect S_1 population indirectly as the $S_1 \rightarrow S_n$ transition of the carotenoids falls into the 530-580 nm, depending on the carotenoid we are considering.[104]

The ultrashort lifetime of S_1 state and the fact that $S_1 \rightarrow S_n$ transition occurs in few ps makes difficult the observation of S_1, being visible only when it is highly populated. To unveil the contribution of Car S_1 in the overall ^{1}Chl* quenching, we performed double difference spectra by subtracting the spectrum at 500 fs from the spectrum at 5 ps. Results of this operation are shown in figure 3.14 alongside with the kinetics at 570 nm.

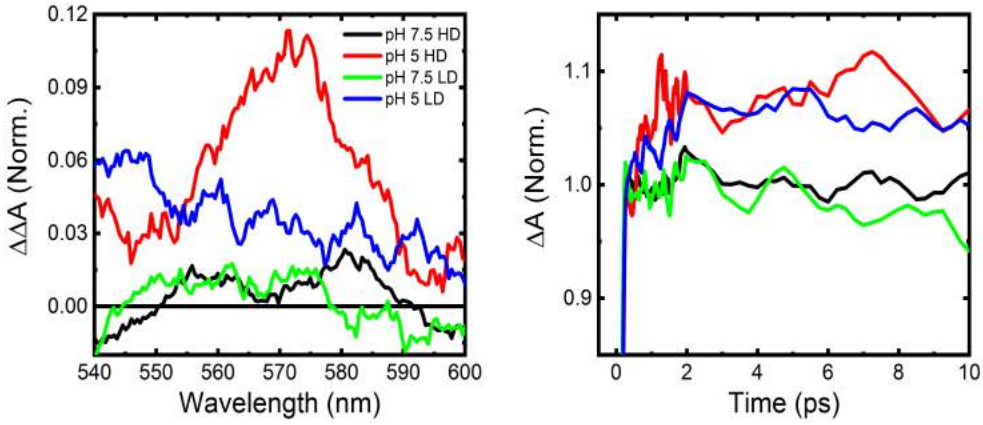

Figure 3.14: *(Left)* Normalized TA double difference spectra obtained by substraction of the spectra at 500 fs from the one at 5 ps following 630 nm excitation. Normalization done at the Chl a GSB peak. *(Right)* Normalized kinetics at 570 nm in the first 10 ps, showing Car $S_1 \rightarrow S_n$ transition. Normalization done at ≈300 fs after excitation.

After spectra subtraction (figure 3.14 left), we see a positive signal from 550 to 590 nm for all samples which is more evident in pH 5 samples. pH 5 HD is the sample in which this feature is more pronounced, observing a peak at ≈570 nm. Therefore, we focused on the kinetics at this wavelength (figure 3.13 right) and we see a slight but clear rising at early times in pH 5 samples as opposed to pH 7.5 ones. Thus we can say that this weak dissipation channel is pH-dependent as it is only active at low pH conditions.

TA data in the carotenoid region (480-570 nm) was properly fitted with three time constants using a global analysis routine with Glotaran software.[92] As described in chapter 2, we assumed an unidirectional model in which each component decay sequentially following the scheme $1 \rightarrow 2 \rightarrow 3...$ Fit results alongside its fitting errors are summarized in table 3.3 while decay-associated spectra (DAS) of all samples are shown in figure 3.15.

	τ_1 (ps)	τ_2 (ps)	τ_3 (ps)
pH 7.5 HD	13.3 ± 0.1	105 ± 1	1547 ± 13
pH 5 HD	10.1 ± 0.1	80 ± 1	713 ± 6
pH 7.5 LD	11.1 ± 0.2	100 ± 1	678 ± 7
pH 5 LD	9.0 ± 0.1	69 ± 1	475 ± 2

Table 3.3: LHCSR3 global analysis fitting results for all samples in the 480-570 nm range.

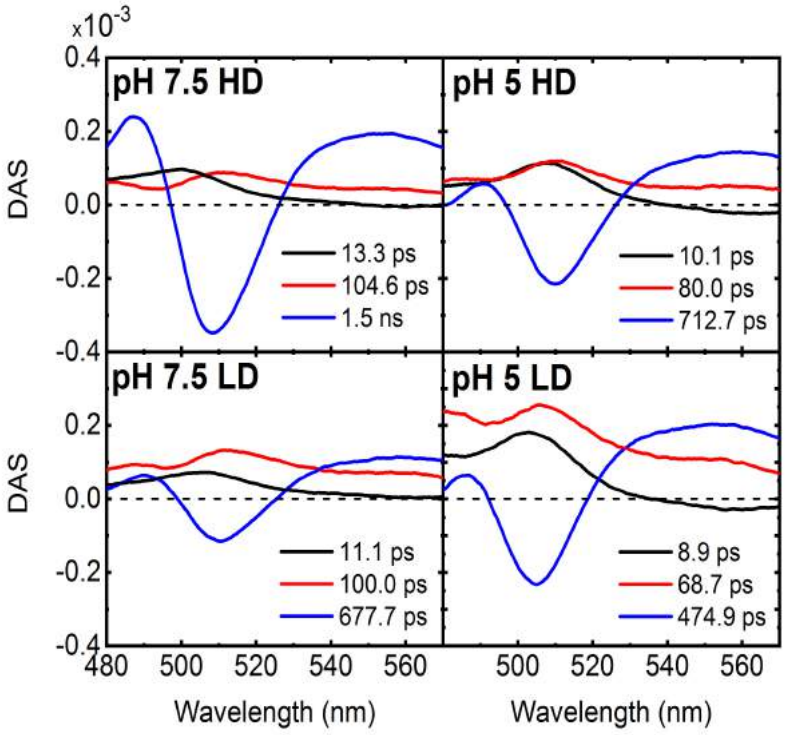

Figure 3.15: DAS of the time constants found after global analysis in the visible for all samples.

We assign the calculated time constant as follows: a fast multiexponential buildup of the carotenoid GSB in the first tens of picoseconds (τ_1: ≈10 ps, τ_2: 70-100 ps) and the rise of the Car triplet state in the hundreds of ps (τ_3: 500-1500 ps). It is important to notice that the component associated with the carotenoid triplet state arise (τ_3) becomes faster the more quenched the sample is due to the shorter lifetime of ^{1}Chl* state.

All this data confirms the influence of carotenoids in the overall qE process as we can correlate the lifetime shortening of ^{1}Chl* (figures 3.5 right and 3.9 right) with the buildup of the carotenoid GSB. Nevertheless, we can not provide conclusive evidence about the quenching mechanism, as we are not able to distinguish if the Car GSB is related to energy or charge transfer from chlorophylls to carotenoids.

As carotenoid radical cations absorb in the NIR region,[104,106] we extended our experiments to the 850-1050 nm spectral range to determine whether an electron transfer to the photoexcited Chls is the reason for Car GSB or not. Figure 3.16 shows the TA maps in the NIR range.

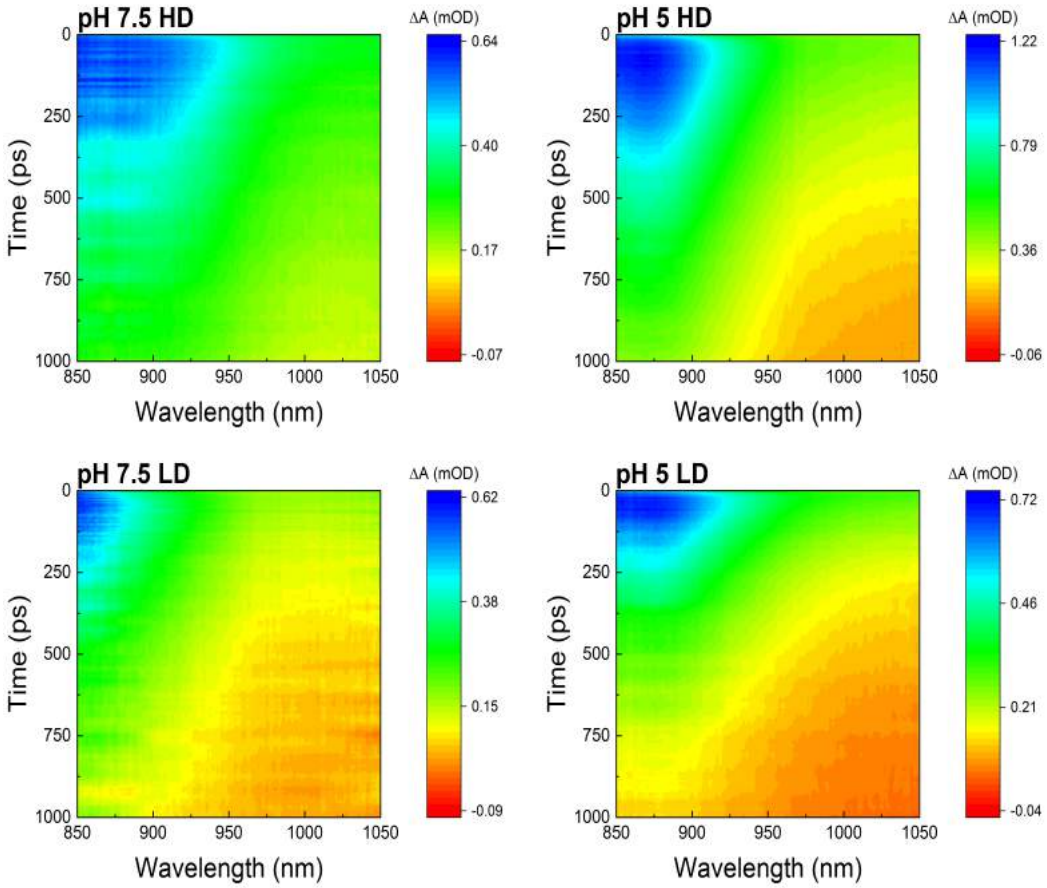

Figure 3.16: NIR TA maps of LHCSR3 in different quenching conditions after excitation at 630 nm.

We observe a positive band all over the spectral range with a maximum between 850 and 900 nm which becomes stronger at low pH conditions. This signal was previously assigned to a ^{1}Chl* PA[101] process in which carotenoid radical cation formation is also involved. Carotenoid radical cation formation is an ultrafast process that happens in few ps,[114] so we focused on the signal at early times. Figure 3.17 shows spectra of the sample with the strongest Car GSB signal, pH 5 LD, at different times after excitation

(see figure 3.12 right).

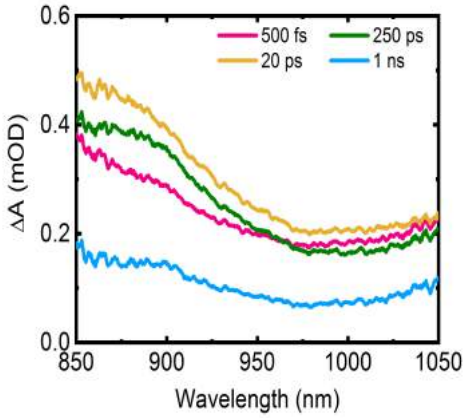

Figure 3.17: NIR TA spectra of pH 5 LD sample at different times after excitation at 630 nm

At 20 ps after excitation, we see a clear buildup which is more evident at ≈880 nm with respect to 1050 nm. As chlorophyll population decays within this time scale, this signal must be related to the formation of the radical cation previously mentioned.

Even so, this information is not enough to determine which carotenoid is involved in the process. To figure this out, we performed double difference spectra by subtracting the 500 fs spectrum from another at 20 ps, when the radical cation is already formed. This operation, alongside with TA kinetics at 870 nm for all samples are represented in figure 3.18.

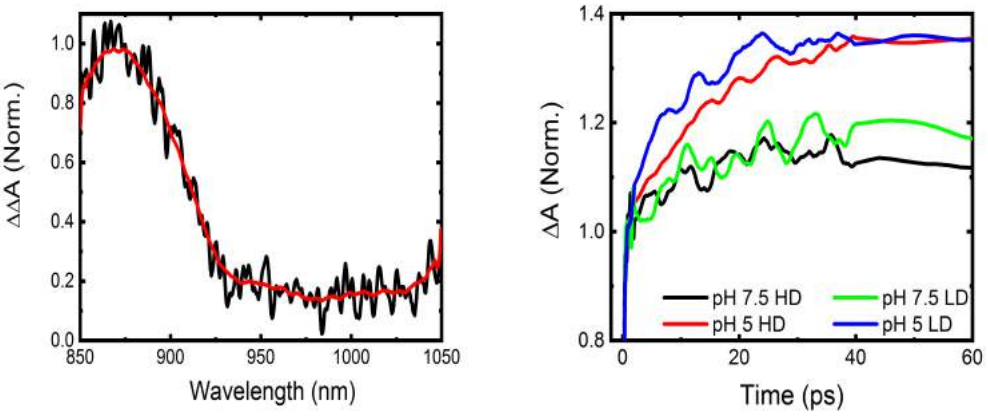

Figure 3.18: *(Left)* Double difference spectrum obtained by subtraction of the spectra at 500 fs from the one at 20 ps. Smoothed line in red *(Right)* Normalized TA kinetics at 870 nm for all samples. Normalization done at 870 nm for the spectrum and at ≈800 fs after excitation for the kinetics

Figure 3.18 left shows the resulting spectrum after the double difference operation peaking at 870 nm, which is in very good agreement with the PA spectrum of a lutein radical cation previously observed.[115] Nevertheless, our limited spectral coverage does not allow us to unequivocally determine if lutein is the only carotenoid involved as the

radical cation of the other carotenoid present in LHCSR3, violaxanthin, peaks at 830 nm.[115] TA kinetics at 870 nm (figure 3.18 right) shows that the radical cation is formed in all cases but enhanced at pH 5 conditions, specially at LD concentration. On the other hand, the radical cation is formed in the same amounts at pH 7.5 regardless of the amount of detergent we use. Therefore, these results point out a clear pH dependence in the radical cation formation.

TA data in the NIR region (880-1050 nm) was properly fitted with three time constants following the same global analysis routine we used with the visible data. Fitting results are shown in table 3.4 and decay-associated spectra (DAS) of all samples are visible in figure 3.19.

	τ_1 (ps)	τ_2 (ps)	τ_3 (ps)
pH 7.5 HD	9.7 ± 0.2	71.4 ± 3.1	894.2 ± 12.5
pH 5 HD	10.0 ± 0.1	55.9 ± 0.5	770 ± 2.9
pH 7.5 LD	19.4 ± 0.5	86.7 ± 4.4	550.4 ± 8.7
pH 5 LD	10.1 ± 0.1	54.1 ± 1	408.5 ± 1.1

Table 3.4: LHCSR3 global analysis fitting results for all samples in the 880-1050 nm range

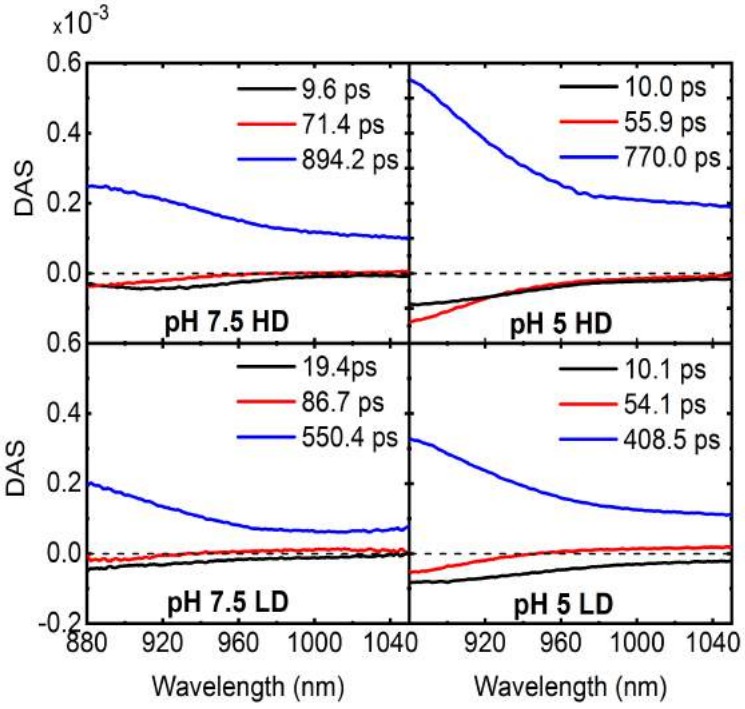

Figure 3.19: Decay-associated spectra of the time constants found after global analysis in all samples in the 880-1050 nm region

Global analysis fitting was performed using three time constants for all samples. These constants were assigned to a fast multiexponential buildup of the carotenoid radical cation in the first tens of picoseconds (τ_1: ≈10 ps, τ_2: 50-90 ps) and a longer decay in the hundreds of ps timescale (τ_3: 400-900 ps) associated to both carotenoid radical cation and chlorophyll excited state decays. The fastest components, τ_1 and τ_2, match very well with those found in the global analysis performed in the visible and related to the buildup of the Car GSB signal at 500 nm (see figure 3.11 and table 3.3). We can thus conclude that the buildup of the PA signal in the NIR and the Car GSB in the visible are proof of the radical cation formation and define electron transfer from carotenoids to chlorophyll as a significant quenching mechanism which is enhanced at low pH and high protein aggregation conditions.

3.3 Discussion

According to the signals discussed in the previous section, we can propose a model which explains ^{1}Chl* de-excitation. The model is shown in the Jablonski diagram in figure 3.20.

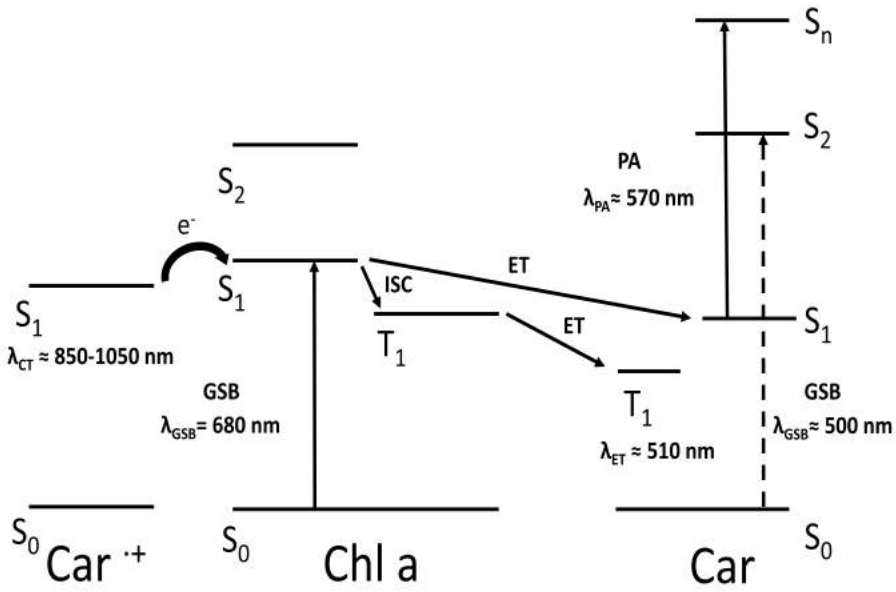

Figure 3.20: ^{1}Chl* de-excitation pathways after selective excitation at 630 nm.

This model starts with a Chl a GSB at 680 nm and a concomitant Car GSB with a maximum around 500 nm. From this point, ^{1}Chl* population can follow several pathways. In a short timescale, we can observe an energy transfer from the ^{1}Chl* to Car S_1 states in the visible range and an electron transfer from carotenoids to chlorophylls happening in the NIR. In a longer timescale, however, ^{1}Chl* can undergo intersystem

crossing and generate ^{3}Chl*. Thus, we observe a carotenoid triplet formation through a ^{3}Chl* $\rightarrow$ ^{3}Car* energy transfer. In this model, the main quenching mechanisms in LHCSR3 are the electron transfer from carotenoids to chlorophylls and a weak energy transfer from ^{1}Chl* to Car S_1 state. These mechanisms work simultaneously and are observed in all pH and detergent conditions, implying that these pathways are always active but enhanced by low pH and low detergent concentrations. Figure 3.21 shows a brief scheme of the quenching mechanisms happening in LHCSR3 after Chl a excitation at 630 nm.

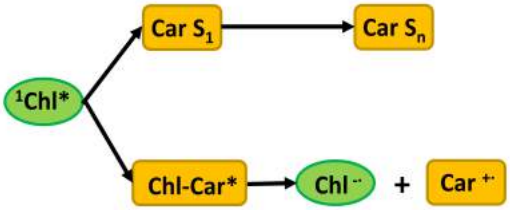

Figure 3.21: ^{1}Chl* quenching mechanisms in LHCSR3 after selective excitation at 630 nm.

These two mechanisms were recently observed *in vivo* for LHCX1 in *Nannochloropsis oceanica*[105] while only ^{1}Chl* to Car energy transfer was reported *in vitro* for LHCSR1 from *Physcomitrella patens*.[104] Nevertheless, in both proteins the presence of zeaxanthin was key in the activation of these mechanisms. Energy transfer was also reported in trimeric LHCII but only in aggregation conditions.[97]

Here, we presented the case of *in vitro* LHCSR3 from *Chlamydomonas Reinhardtii*, in which both carotenoid radical cation and energy transfer to the carotenoid S_1 state are observed at low pH conditions and regardless the presence of zeaxanthin or protein aggregation. However, these quenching mechanisms are not enough to entirely explain LHCSR3 quenching activity, since we see that the pH 7.5 LD sample is more quenched than pH 5 HD one as opposed as we could expect considering that both processes happen predominantly at low pH.

Therefore, protein-protein interaction must constitute an additional quenching mechanism which is stronger at low detergent conditions, where LHCSR3 simulates its *in vivo* activity.[76] Several works have reported aggregation-dependent quenching mechanisms[93,97,116,117] under *in vivo* and *in vitro* conditions for different LHC complexes in higher plants. These mechanisms are characterized by the appearance of a far-red fluorescence in leaves.[118] In quenched cells of *C. Reinhardtii*, however, this far-red fluorescence was not observed.[119]

In our case, both TRF and TA data reveal the presence of the aggregation-related quenching mechanism as we see ^{1}Chl* decay components in the first hundred of picoseconds timescale in LD conditions which become more important at pH 5 (Figures 3.5

and 3.9). These results agree with those found on *in vitro* LHCSR1 from *Physcomitrella Patens* in LD conditions,[104] as they associated a sub 100 ps decay component to the formation of aggregates due to its red-shifted spectrum. Furthermore, a previous work on LHCII *in vitro* showed that, apart form the ^{1}Chl* $\rightarrow$ Car S_1 energy transfer pathway, the principal quenching mechanism related to aggregation was the formation of a Chl-Chl transfer state,[93] which could explain the strong quenching we are observing in the LD samples.

With all the reasons exposed before, we can propose a quenching model for LHCSR3 in which lumen acidification triggers qE in the protein, switching it to a highly quenched state where protein-protein interactions and charge transfers from carotenoids to chlorophylls are the main quenching mechanisms.

Chapter 4

Non-photochemical quenching on *Chlamydomonas Reindhartii* mutant

In previous chapters, we pointed out the importance of LHCSR3 protein in NPQ induction as it serves both as a pH sensor and as a quencher. Briefly, we studied the quencher aspect of the protein and proposed a model in which the main quenching mechanisms on wild type *C. Reinhardtii* were a charge transfer from carotenoids to chlorophylls and a non-radiative protein-protein interaction. Charge transfer mechanism was observed as a carotenoid radical cation and a chlorophyll radical anion formation. Protein-protein interaction (referred as protein aggregation) was observed as a strong detergent-dependent quenching in the ^{1}Chl* de-excitation both in TRF and TA (see figures 3.5 (right) and 3.10 (right)). Nevertheless, we did not deepen into the pH sensing ability of LHCSR3.

Liguori et al. and Ballottari et al. showed in their respective works[76,77] that pH sensing is performed in LHCSR3 thanks to the presence of eight carboxylic acid groups facing the lumenal part of the thylakoids (four glutamic acid and four aspartic acid residues) in the C-terminus part of the proteins. In both works, the authors also study how pH sensing suppression affects the photophysics of LHCSR3 in *C. Reindhartii*. To do so, they compared the dynamics of the fluorescence decay at 680 nm between a wild type strain of LHCSR3 and a mutant with no pH sensing functions at two pH values: acid and neutral. pH sensing suppression was achieved either by the removal of all acid groups[76] or by the exchange of those groups for new ones which are insensitive to pH changes (glutamine and asparagine).[77] In both cases, the fluorescence kinetics of the mutant strain did not show any remarkable differences at the two pH conditions as opposed to the wild type strain, pointing out the sensitivity of the C-terminus group as a pH sensor and its qE induction capabilities.

In this chapter, we compare the spectroscopic properties in acid (pH=5) and neutral pH (pH=7.5) between wild type *C. Reindhartii* LHCSR3 protein and a mutant in which all acid groups are replaced by a non pH sensitive residue, bm6. For simplicity, we will refer at these two proteins as WT (wild type) and bm6 (mutant bm6). Section 4.1

is focused on the experimental results obtained using TRF and TA techniques on the wild-type and the bm6 mutant while section 4.2 is dedicated to the discussion of the results.

4.1 Experimental results

4.1.1 Sample preparation and characterization

The amplification of LHCSR3 coding sequence was done using the same protocol explained in chapter 3. Very briefly, LHCSR3 coding sequence was amplified using high light adapted *C. Reindhardtii* complementary DNA, cloned into an expression vector and then LHCSR3 cells were overexpressed using *E. coli* cells. Finally, LHCSR3 was purified as an inclusion body and refolded *in vitro* with pigment addition to get the final LHCSR3 holoprotein as previously reported.[109] Pigment composition and structure of the refolded protein can be seen in table 4.1 and figure 4.1.

As we saw in the previous chapter, aggregation plays a significant role in LHCSR3 dynamics. We used a solution of 0.03% n-dodecyl-α D-maltoside (α-DM) as a detergent for two reasons: (i) to recreate the high detergent conditions we used in the previous chapter and (ii) to be able to do a relative comparison between the results obtained in this work and the results obtained in the previous chapter. pH was set using 20 mM solutions of pH 7.5 or pH 5 comercial buffer (HEPES). bm6 mutants were created from the wild type following the protocol described in previous works.[77]

Pigment	**Chls**	Chl a	Chl b	**Cars**	Vio	Lut
WT	7.00	6.85	0.15	7.00	4.14	2.86
bm6	7.00	5.87	1.13	6.81	4.39	2.42

Table 4.1: Refolded LHCSR3 pigment analysis.

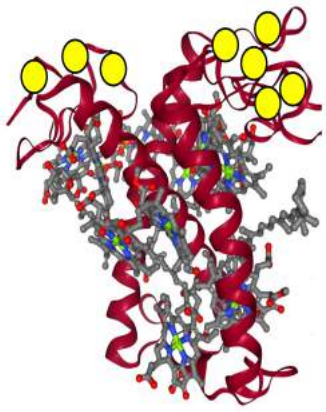

Figure 4.1: LHCSR3 bm6 mutant structure. bm6 group represented as yellow circles.

LHCSR3 WT and the bm6 mutant were then characterized by steady-state absorption spectroscopy. Absorption spectra normalized at the chlorophyll absorption peak in the Q_y band is shown in figure 4.2.

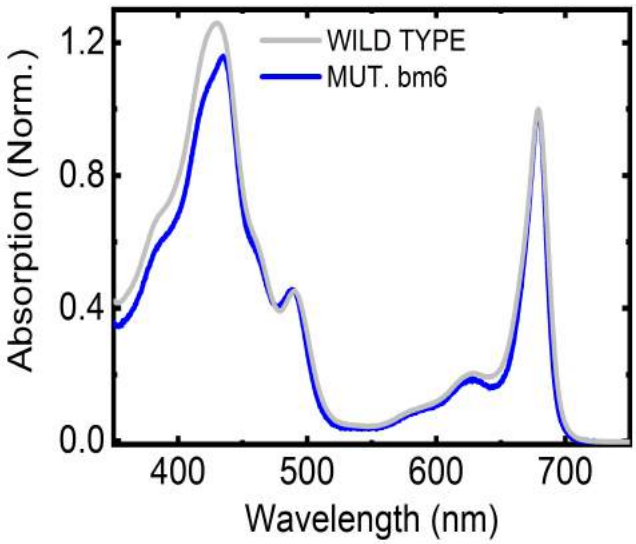

Figure 4.2: Steady-state absorption spectrum of LHCSR3 at room temperature. Normalization done at the peak of the Q_y absorption band (≈680 nm).

From figure 4.2, we observe the two typical Chl a absorption bands: one from 350 to 500 nm with a peak around 430 nm corresponding to the Soret band and the Q_y band peaking around 680 nm and a higher vibrational band at ≈630 nm.

Both LHCSR3 WT and bm6 were further characterized using steady-state fluorescence spectroscopy. Figure 4.3 shows the results of both proteins at different excitation wavelengths.

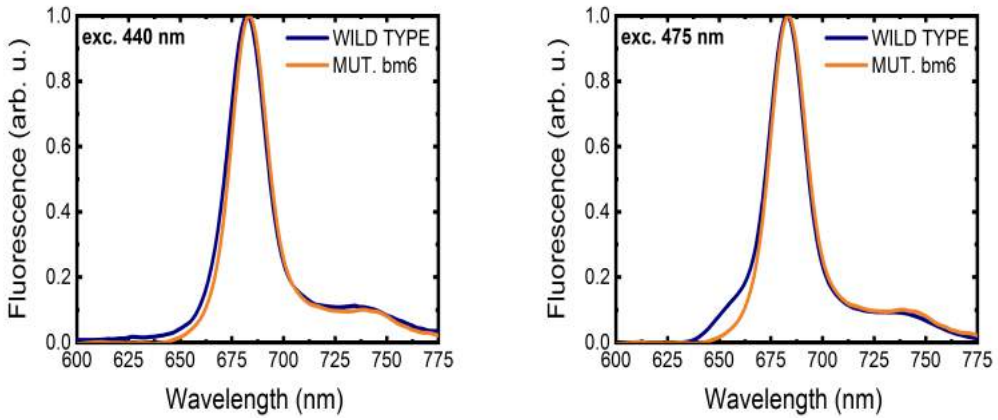

Figure 4.3: Steady-state emission spectra of LHCSR3 WT and bm6 mutant with excitation at 440 (left) and 475 nm (right), respectively.

For all samples, we observe the typical Chl a fluorescence emission range between 650 and 800 nm, with a peak at ≈685 nm and a shoulder around 725 nm, regardless the excitation wavelength.

4.1.2 Time resolved fluorescence

TRF measurements were performed with the setup described in chapter 2 with the same technical features we selected in chapter 3. Briefly, we chose 430 nm as the excitation wavelength to match the Soret band absorption. This wavelength is obtained after SHG of a 860 nm fundamental excitation source so we removed the residual pump light by placing a longpass filter with a cutoff at 700 nm (BG40). In order to remove the residual 430 nm excitation light after the sample, we placed a longpass filter with a cutoff at 495 nm (LP495). Also, temperature was set at 12°C to guarantee protein structural stability. Experimental maps of LHCSR3 WT and bm6 can be seen in figure 4.4.

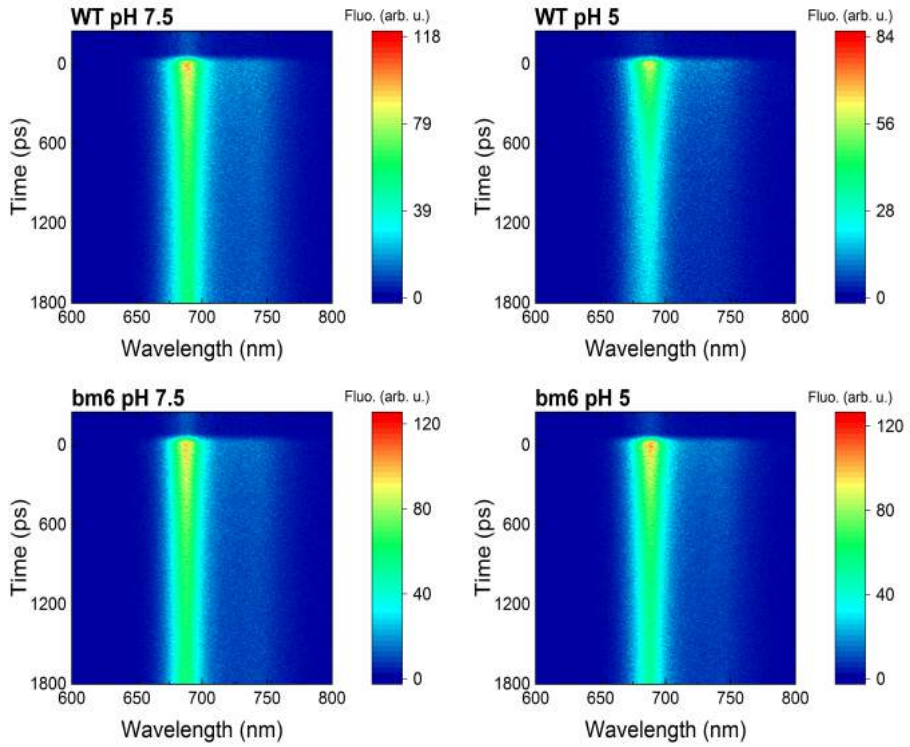

Figure 4.4: TRF maps of LHCSR3 WT and bm6 mutant in different quenching conditions after excitation at 430 nm.

In figure 4.5, we can see the spectra and kinetics of all samples after integrating all over the temporal window and between 650 and 760 nm, respectively.

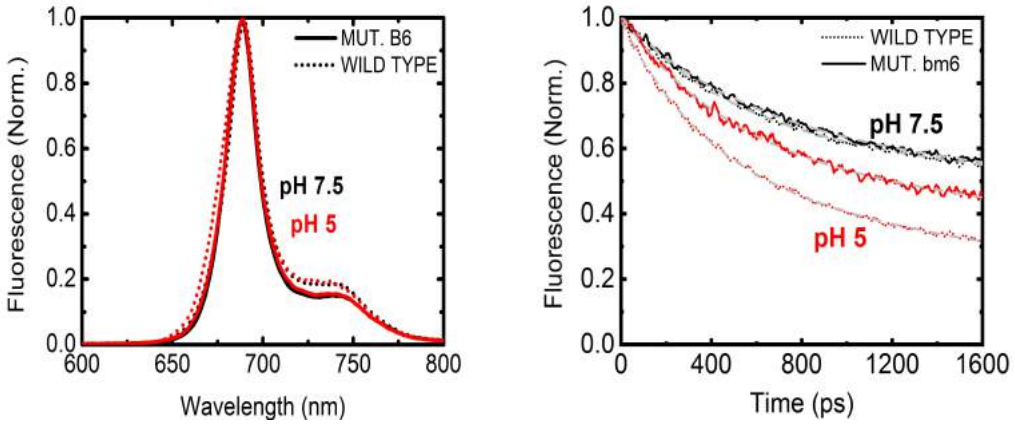

Figure 4.5: Time-resolved fluorescence spectra *(left)* and kinetics *(right)* of LHCSR3 WT and bm6 mutant samples at ≈12°C (pH 5 samples shown in red; pH 7.5 samples shown in black). Fittings of the experimental kinetics are also shown in the right panel as dashed gray lines.

From figure 4.5 (right), we can observe that pH variation affects considerably the overall LHCSR3 lifetime, being the lifetime shorter the lower the pH is, either for the wild type and for the bm6. Also, for both pH conditions we see that the bm6 mutant shows a longer lifetime than the wild type. Results of biexponential kinetic fitting are shown in table 4.2 alongside with the average lifetime (τ_{avg}=$\Sigma A_i \tau_i$) obtained for all samples.

	$\mathbf{A_1}$ **(%)**	τ_1 **(ps)**	$\mathbf{A_2}$ (%)	τ_2 **(ps)**	τ_{avg} **(ps)**
pH 7.5 WT	37	498	63	9762	**6437**
pH 5 WT	49	386	51	3297	**1871**
pH 7.5 bm6	37	582	63	9996	**6513**
pH 5 bm6	44	478	56	6197	**3681**

Table 4.2: LHCSR3 WT/bm6 mutant biexponential fitting results for all samples

It is noticeable that our fitted τ_{avg} for the wild type here differs from the results of the high detergent wild type samples obtained in the previous chapter. As we saw, samples dynamics are very sensitive to environmental changes so it is reasonable to think that sample treatment can induce some changes in their dynamics. In this sense, we decided to remeasure the wild type strain from which the bm6 mutant was obtained to do a consistent comparison between the wild type and the bm6 mutant. In any case, in a qualitative aspect, we see the same results we observed in chapter 3.

4.1.3 Transient absorption measurements

Transient absorption measurements were performed in the setup described in chapter 2 with the settings described in chapter 3. Briefly, the pump wavelength was set at 630 nm to selectively excite the higher vibrational band of the Q_y state of chlorophyll a and the probe consisted in a broadband white light between 450 and 750 nm. Pump beam was further modulated by a chopper and its polarization was selected to match the magic angle condition with respect to the probe beam. Finally, samples temperature was set at ≈12 ^{o}C to avoid protein degradation. In the previous chapter, we saw that chlorophyll singlet-singlet annihilation can cause distortions in the kinetics of our samples.[110] In order to do a correct analysis of the LHCSR3 kinetics, we first did fluence dependence measurements on our samples to choose a safe value for each one. Figure 4.6 shows the kinetics measured at the chlorophyll a GSB peak at ≈680 nm.

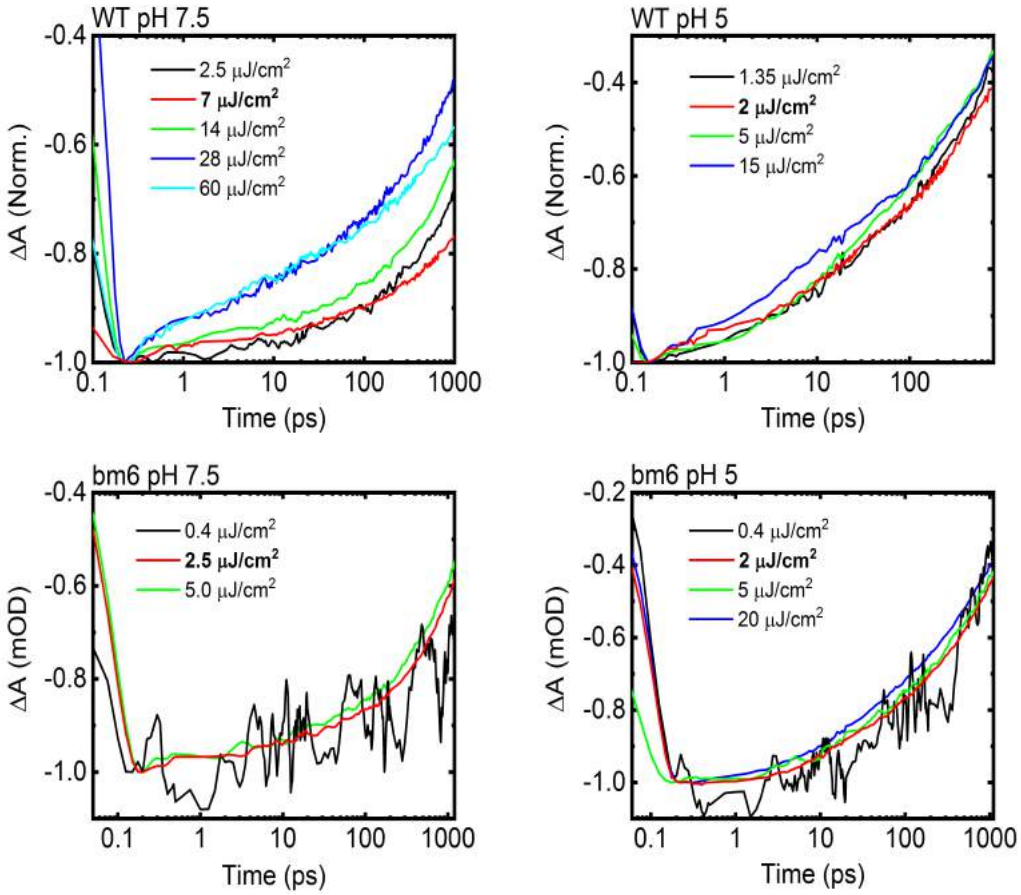

Figure 4.6: Fluence dependence of LHCSR3 WT and bm6 mutant. Normalized kinetics at the Chl a GSB peak (≈680 nm) after excitation at 630 nm for all samples.

Singlet-singlet annihilation kinetics-distorting effects are noticeable at values above 15 μJ/cm^2, so we selected 7 μJ/cm^2 as a safe fluence value for WT pH 7.5 and ≈2 μJ/cm^2 for all the other samples (the specific fluences used in each measurement are shown in bold in the legend of their respective graph in figure 4.6). As a remark, fluence dependence measurements have shorter acquisition times than the final measurements, therefore the fluence dynamics at 680 nm show a worse signal to noise ratio than the final measurements. Once we set the correct fluence values for all samples, we performed TA measurements in the visible (450-750 nm). TA maps for all samples are shown in figure 4.7.

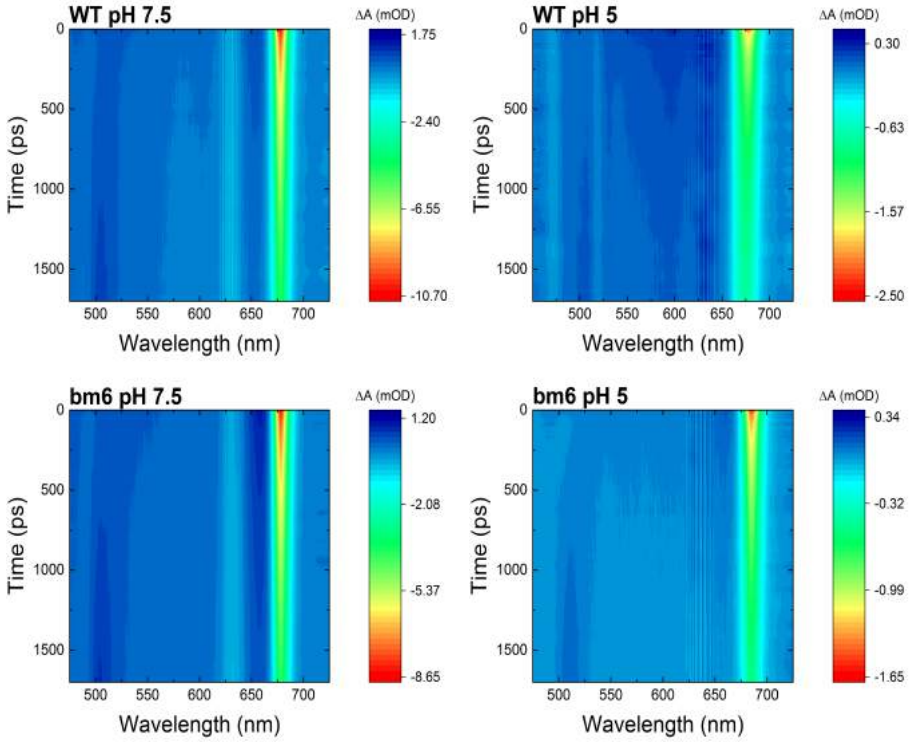

Figure 4.7: TA maps of LHCSR3 WT and bm6 mutant in different quenching conditions after excitation at 630 nm

Similarly to what we saw in the previous chapter, TA maps show two characteristic features: a strong negative peak around 680 nm and a broad positive band from 450 to 600 nm. The 680 nm signal comes from the chlorophyll a ground state bleaching (GSB) and its stimulated emission (SE) while the signal between 450 and 600 nm can be attributed to ^{1}Chl* photoinduced absorption (PA). In addition, some pump scattering can be observed at 630 nm.

We then looked at the LHCSR3 carotenoid activity region (450-600 nm). Spectra of all samples at different time delays can be seen in figure 4.8.

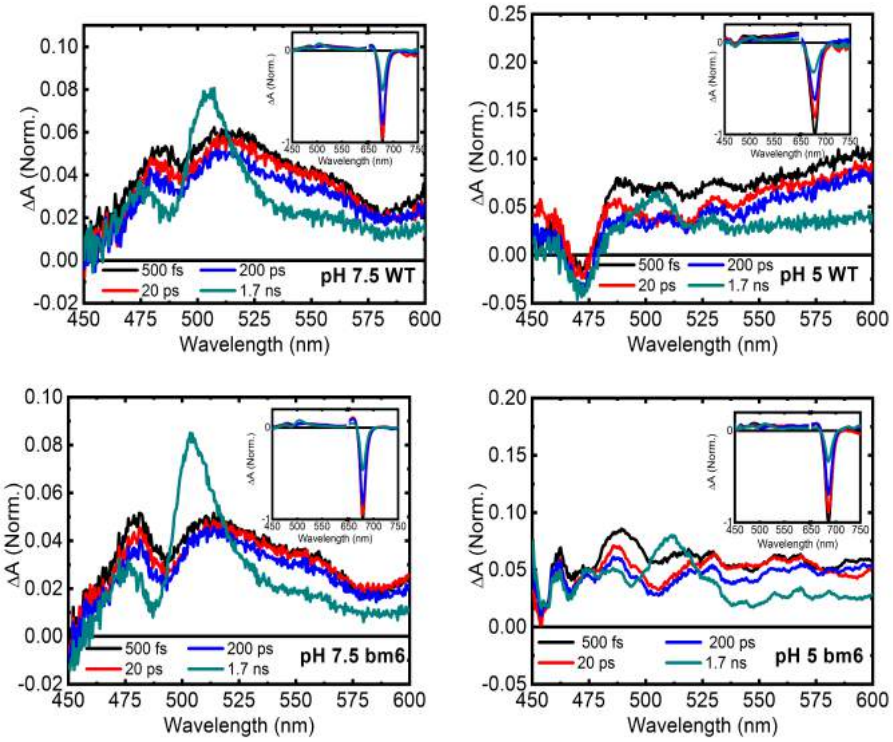

Figure 4.8: TA spectra of LHCSR3 WT and bm6 mutant between 450 and 600 nm. Spectra were obtained at different times after excitation at 630 nm for all samples. Inset: TA spectra for all samples in the 450-750 nm range at the different times after excitation, showing the Chl a GSB peak at ≈680 nm. All spectra are normalized to their respective Chl a GSB peak at 500 fs.

Spectra at early times in this region are characterized by two minima at ≈470 and ≈500 nm, being the 470 nm peak only visible at pH 5 conditions. The energy difference between these two peaks is ≈1360 cm^{-1}, which agrees with the energy gap between 0-0 and 0-1 vibrational bands of the carotenoid absorption spectra[111] and therefore, we can assign this wide band to a carotenoid bleaching. From figure 4.8, we can see that carotenoid GSB signal at 500 nm is more intense at pH 5 than at pH 7.5 for both the WT and the bm6 mutant. Nevertheless, the most evident spectral difference between pH 5 and pH 7.5 samples is the formation of a carotenoid triplet at ≈510 nm[120] at longer times. We see the signal at both pH conditions, however its intensity is stronger at pH 7.5 than at pH 5.

Focusing in the kinetics of our samples, we start with the Chl a GSB peaking around 680 nm. Kinetcs of this signal alongside with a detailed spectral analysis are shown in figure 4.9.

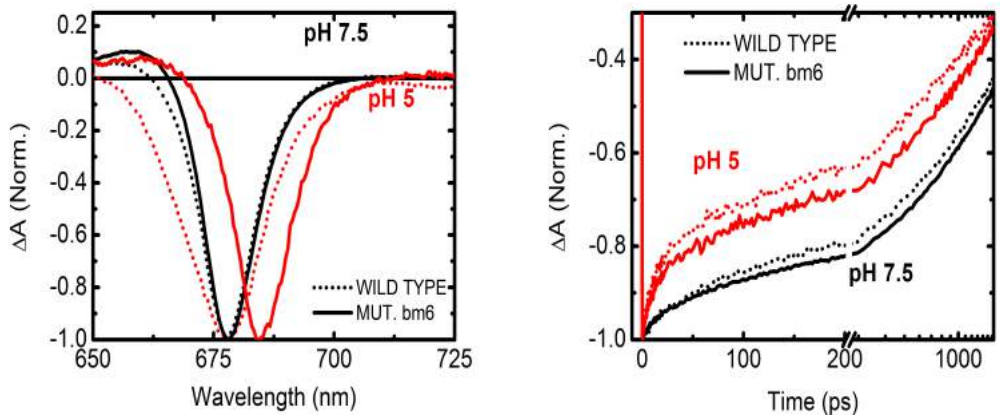

Figure 4.9: LHCSR3 WT/bm6 mutant Chl a GSB features: spectra *(left)* and kinetics *(right)* of all samples at ≈12°C (pH 5 samples shown in red; pH 7.5 samples shown in black).

Transient absorption kinetics at the Chl a peak (figure 4.9 right) show similar results than those obtained from TRF: pH constitutes the main quenching factor in chlorophyll GSB as we observe a faster decay at low pH and also mutant bm6 exhibits a longer lifetime than the wild type regardless the pH conditions. Regarding TA spectra (figure 4.9 left), at low pH, the mutant shows a red shift in its maximum and peaks at 684 nm as opposed to the 677 nm maximum found in the other samples. Also, the WT pH 5 sample shows a broader spectrum that is not seen in the other samples.

Peaks broadening and red shifting effects at low pH can be explained considering that low pH conditions induce protein aggregation.[121] To estimate samples' level of aggregation, we observed the intensity of the scattered light at the pump wavelength (630 nm) at 200 ps after excitation. Results are shown in figure 4.10:

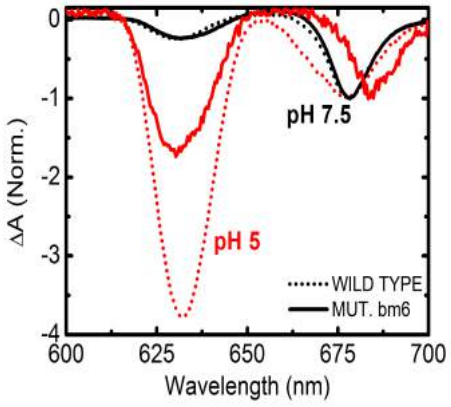

Figure 4.10: LHCSR3 TA normalized spectra at 200 ps showing the pump scattering at 630 nm (pH 5 samples shown in red; pH 7.5 samples shown in black). All spectra were normalized at its respective chlorophyll emission maximum.

From figure 4.10, we can see that the pump scattering is more relevant at pH 5 as opposed to pH 7.5 for the WT and especially for the bm6 mutant. Chlorophyll GSB peak broadening/shifting are thus produced by pH-induced protein aggregation.

In the previous chapter, we saw carotenoid bleaching and triplet formation between 480 and 575 nm so we focused on that specific spectral region. TA maps for all samples can be seen in figure 4.11.

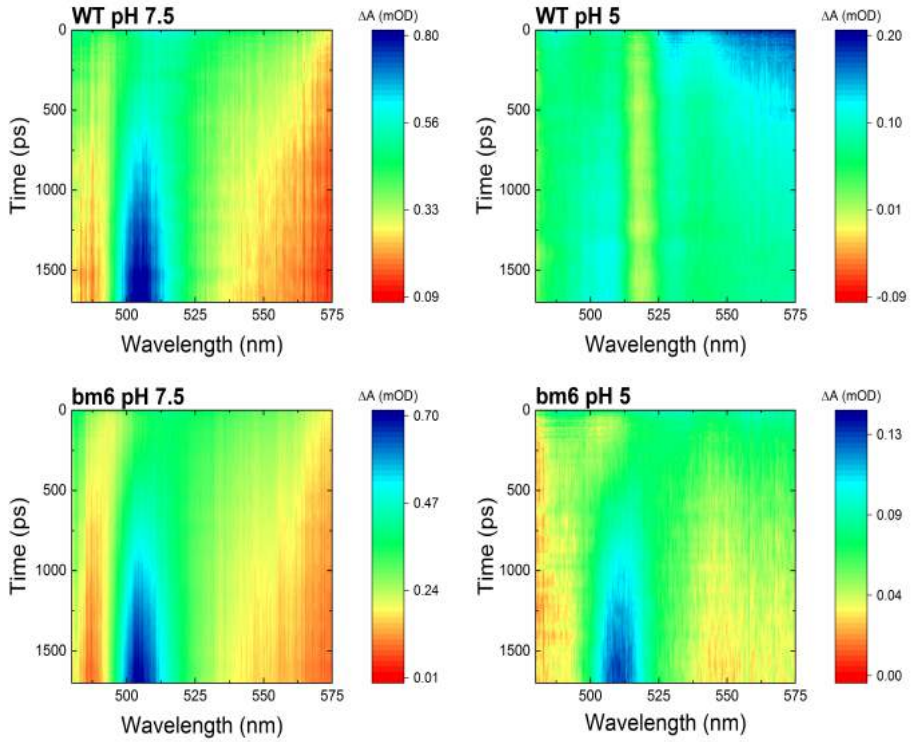

Figure 4.11: TA maps of LHCSR3 WT and bm6 mutant in the carotenoid activity region (480-575 nm) at different quenching conditions after excitation at 630 nm.

Figure 4.11 shows an overall positive ΔA signal all over the 480-575 nm range with a maximum at longer times around 510 nm for all samples. This signal (which is more prominent at pH 7.5) cannot come exclusively from the broad PA of ^{1}Chl* and therefore it is attributed to the absorption of the carotenoid excited triplet state.[95,104,111] It is also important to consider that the previously observed signal at 500 nm at early times and assigned to carotenoid GSB here is not so strong but it is still visible. Similarly to what we saw in the previous chapter, the fact that the chlorophylls and carotenoids couple immediately after excitation is a sign of an ultrafast electrochromic shift of the carotenoid S_2 state is happening.[103,104,112,113] Regarding carotenoid GSB, figure 4.12 shows the dynamics of all samples at 500 nm in the first 250 ps:

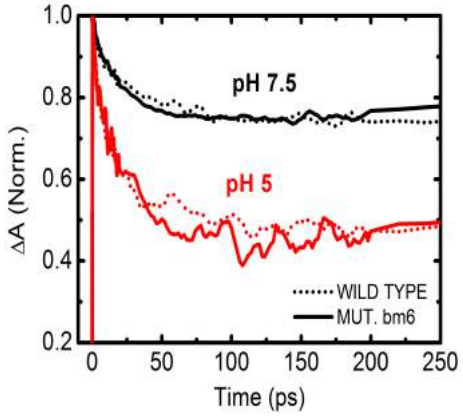

Figure 4.12: TA data of LHCSR3 after excitation at 630 nm. Normalized kinetics at 500 nm, showing the Car GSB (pH 5 samples shown in red; pH 7.5 samples shown in black). All kinetics were normalized at ≈500 fs after excitation.

In figure 4.12 we see the carotenoid GSB pH dependence: both the WT and the bm6 mutant have a stronger relative increase of carotenoid GSB at pH 5 respect to pH 7.5. Also, bm6 mutant and WT present nearly identical kinetics in this timescale. Another aspect to point out in this data is the fact that here we do not observe a change of sign in the overall ΔA signal in the first hundreds of ps, implying that now the Car GSB signal is not strong enough to overcome the Chl a PA and therefore, the signal at 500 nm remains positive. Figure 4.13 shows the kinetics at 510 nm (wavelength which is representative of carotenoid triplet formation) for all samples:

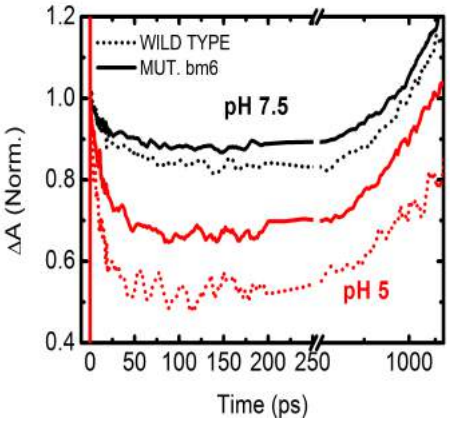

Figure 4.13: TA data of LHCSR3 after excitation at 630 nm. Normalized kinetics at 510 nm, showing the carotenoid triplet formation (pH 5 samples shown in red; pH 7.5 samples shown in black). All kinetics were normalized at ≈500 fs after excitation.

The broad ^{1}Chl* PA signal in the 450-600 nm region provokes that the signal at 510 is a mix between the Car GSB and the Car triplet formation. For that reason, at

early times we see the carotenoid bleaching signal following the same pH dependence we observed in figure 4.12: carotenoids bleach more at pH 5 than at pH 7.5. On the other hand, kinetics at longer times show that more carotenoid triplet is generated at pH 7.5 than at pH 5 conditions. Carotenoid triplet state is populated via ^{3}Chl*-^{3}Car* energy transfer after a chlorophyll intersystem crossing (ISC) from its excited singlet state so, the longer the chlorophyll remains in the singlet state, the more efficient the intersystem crossing will be. According to TRF and TA measurements, the lifetime of both WT and mutant bm6 is longer at pH 7.5 than at pH 5 (see figures 4.5 right and 4.9 right) and subsequently, more carotenoid triplet is formed at low pH.

Chlorophyll excited state quenching can also be explained considering an energy transfer from the ^{1}Chl* to the carotenoid S_1 state. As we saw in the previous chapter, this dissipation channel is not so prominent as it is usually weak and hard to detect. To monitor the carotenoid S_1 state population, we have to look at the Car $S_1 \rightarrow S_n$ transition appearing between the 530 and 580 nm.[104] As $S_1 \rightarrow S_n$ transition is very difficult to detect using pump-probe techniques (it is only visible when the S_1 state is highly populated[104]), we performed a double difference spectra by subtracting the spectrum at 500 fs from the spectrum at 5 ps to search for the signal. Results for all samples are shown in figure 4.14 together with their kinetics at 570 nm in the first 10 ps, when the ultrafast $S_1 \rightarrow S_n$ transition happened.

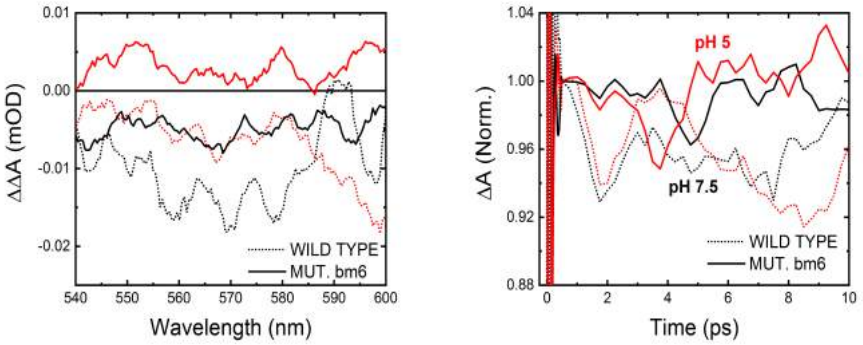

Figure 4.14: TA data of LHCSR3 after excitation at 630 nm. Normalized kinetics at 570 nm, where $S_1 \rightarrow S_n$ transition occurs (pH 5 samples shown in red; pH 7.5 samples shown in black). All kinetics were normalized at ≈500 fs after excitation.

After double spectra subtraction (figure 4.14 left), we see an overall negative weak signal, which is typical for a decaying signal. The negative signal seems to have a minimum at ≈570 nm so we studied the kinetics at that specific wavelength (figure 4.14 right). Here we do not see any significant PA at early times, so we do not have enough spectroscopic evidence to support the idea of a ^{1}Chl*$\rightarrow$ Car S_1 transition as a valuable candidate for ^{1}Chl* de-excitation. At the same time, it is possible that this transition is indeed occurring but we are not seeing it because its signal is lower that our technique sensitivity, so we cannot completely exclude the possibility of ^{1}Chl*$\rightarrow$ Car S_1 happening in our samples.

Transient absorption data in the visible (450-600 nm) was fitted with three time constants using a global analysis with Glotaran software[92] following the same protocol we presented in chapter 3. Very briefly, we chose an unidirectional and sequentially decaying model in which energy is transferred from one species to the following one according to the model $1 \rightarrow 2 \rightarrow 3$. Time constants obtained after global fitting alongside with their fitting errors are shown in table 4.3. Additionally, the decay-associated spectra for all samples are shown in figure 4.15.

	τ_1 (ps)	τ_2 (ps)	τ_3 (ps)
pH 7.5 WT	9.4 ± 0.3	128 ± 2	2325 ± 89
pH 5 WT	7.3 ± 0.5	45 ± 2	891 ± 16
pH 7.5 bm6	21.9 ± 0.5	172 ± 5	4515 ± 207
pH 5 bm6	12.9 ± 0.4	69 ± 2	1251 ± 32

Table 4.3: LHCSR3 WT/mutant bm6 global analysis fitting results for all samples in the 450-600 nm range.

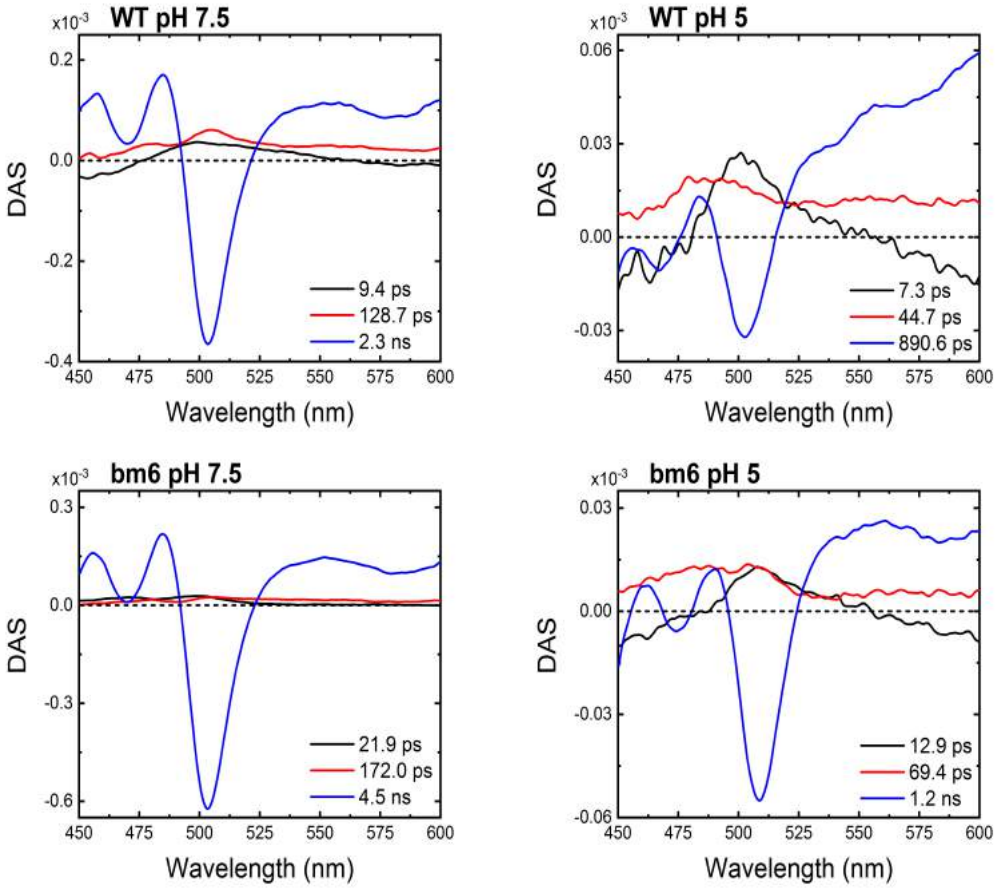

Figure 4.15: Decay-associated spectra in the visible of the time constants found after global analysis.

These results match very well with those obtained for the LHCSR3 wild type at high detergent conditions (see chapter 3, table 3.3 and figure 3.19). Similarly to what we saw in the previous chapter, we can assign the calculated time constants to a fast biexponential buildup of the carotenoid GSB happening in the first hundreds of ps (τ_1= 10-20 ps, τ_2= 50-170 ps) and the rise of the carotenoid triplet state occurring in a longer timescale (τ_3=900-4500 ps). Also, these results allow us to correlate the ^{1}Chl* lifetime shortening we saw both in TRF and TA (figures 4.7 (right) and 4.9 (right)) with the buildup of the Car GSB.

In chapter 3, we observed a carotenoid-chlorophyll charge transfer happening in the NIR region as the main ^{1}Chl* quenching mechanism so we performed measurements in the 850-1050 nm region, where carotenoid radical cations absorb.[104,106] Also, as radical cation formation happens in few ps, we limited our experimental time window to 200 ps. TA maps of all samples are shown in figure 4.16.

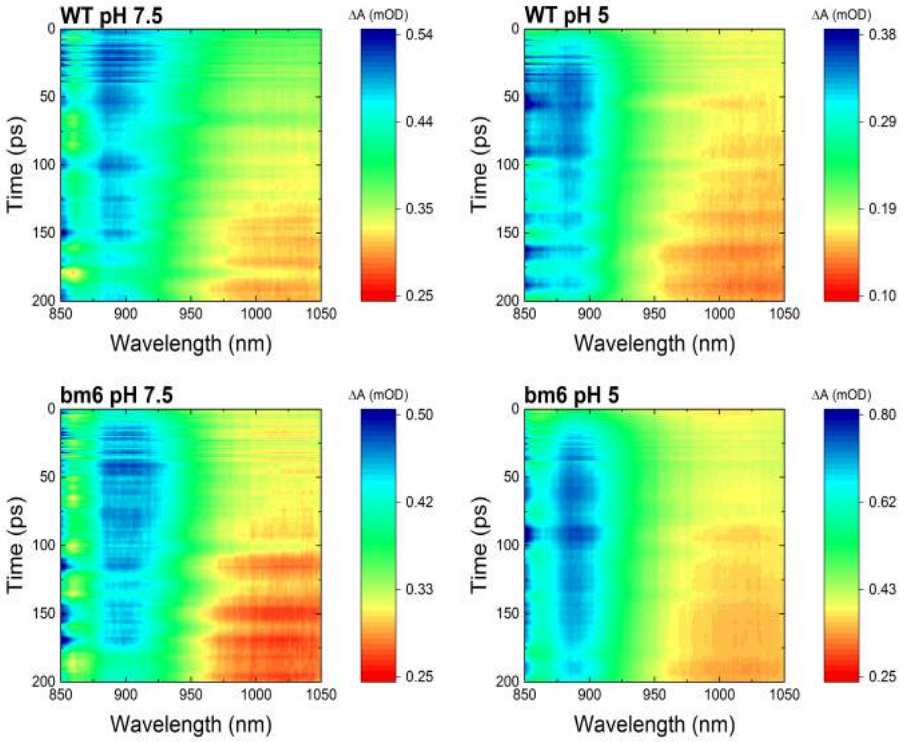

Figure 4.16: TA maps of LHCSR3 WT and bm6 mutant in the NIR region at different quenching conditions after excitation at 630 nm.

We see a positive broadband that extends all over our experimental window with a maximum between 850 and 900 nm that can be linked to a radical cation formation in all cases. Figure 4.17 shows the NIR spectra of each sample at different times after excitation.

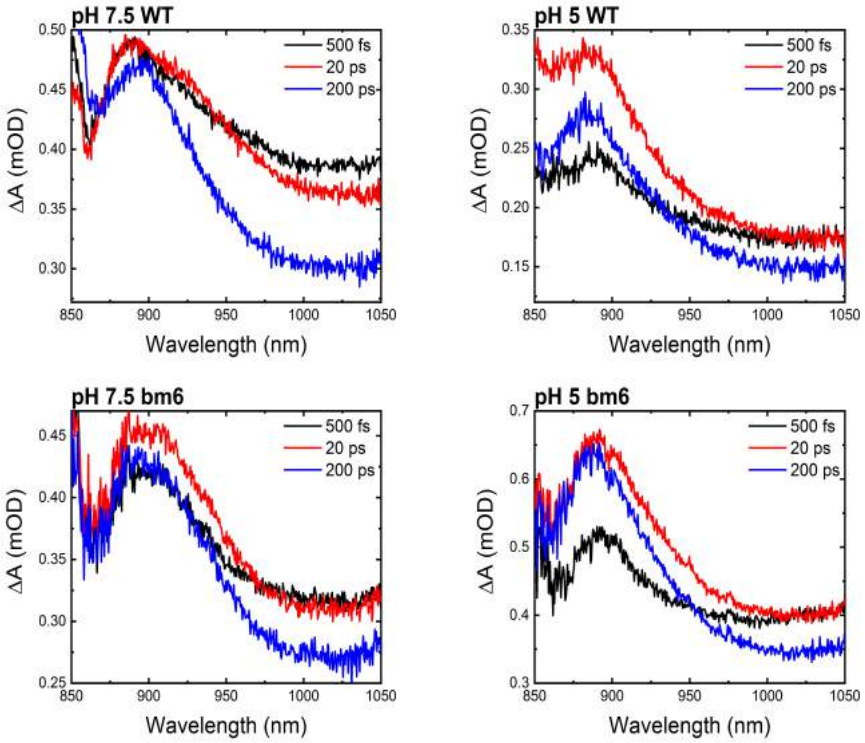

Figure 4.17: TA spectra of LHCSR3 WT and bm6 mutant at different times after excitation at 630 nm. *(Top left)*: pH 7.5 WT, *(Top right)*: pH 5 WT, *(Bottom left)*: pH 7.5 bm6, *(Bottom right)*: pH 5 bm6.

In all cases, we see an increase of the positive signal by comparing the spectra at 20 ps and 500 fs, which becomes more important at pH 5. Chlorophyll decays within this timescale, so we can correlate this signal with a ^{1}Chl* photoinduced absorption[101] and more specifically, with the formation of a carotenoid radical cation. Supporting this point, we have the particular case of WT pH 5 (figure 4.17 top right), in which we can see that the intensity of the signal decreases abruptly after 200 ps. This faster decay matches with the faster dynamics previously observed both in TRF and TA. In order to conclude which one is the carotenoid involved in the process, we performed a double difference spectrum. This operation is represented in figure 4.18:

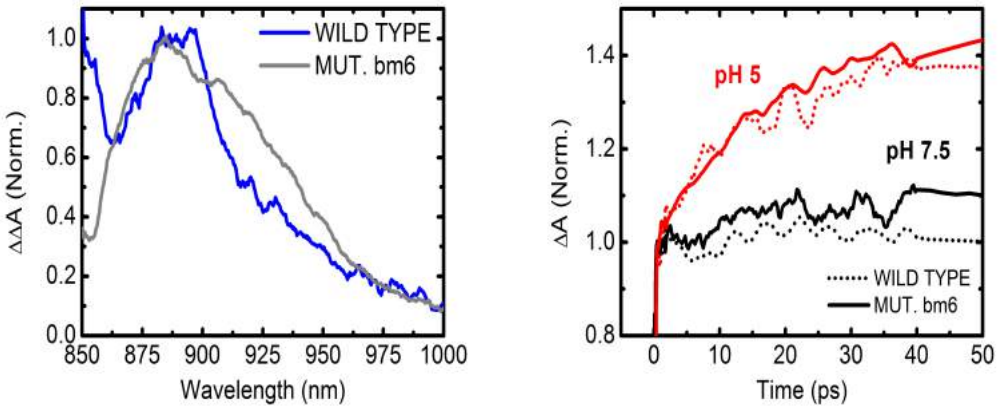

Figure 4.18: (Left) Normalized NIR double difference spectrum obtained by substraction of spectra at 500 fs from the spectrum at 20 ps in pH 5 samples. (Right) Carotenoid radical cation formation kinetics obtained at 880 nm (pH 5 samples shown in red; pH 7.5 samples shown in black). Normalization done at ≈500 fs after excitation.

After double difference subtraction (figure 4.18 left), we see a well defined peak appearing around 880 nm for both the wild type and the mutant bm6 samples. This result matches with the PA spectrum of lutein previously found in chapter 3, so we can assign the signal in the NIR to the formation of a lutein radical cation.[115] The formation of this radical cation is indeed pH dependent as we see the carotenoid radical cation formation in more extension at pH 5 as opposed to pH 7.5 (see figure 4.18 right). Also, it is important to notice that both wild type and bm6 show similar kinetics regardless the pH we consider.

Transient absorption data in the NIR (850-1050 nm) were fitted with two time constants using the same global analysis routine we used in the analysis of the visible TA data. Results are summarized in table 4.4 and the decay-associated spectra are shown in figure 4.19

	τ_1 (ps)	τ_2 (ps)
pH 7.5 WT	—	248 ± 9
pH 5 WT	22.5 ± 0.7	140 ± 10
pH 7.5 bm6	7.0 ± 0.3	—
pH 5 bm6	20.5 ± 0.2	469 ± 72

Table 4.4: LHCSR3 WT/mutant bm6 global analysis fitting results for all samples in the 850-1050 nm range

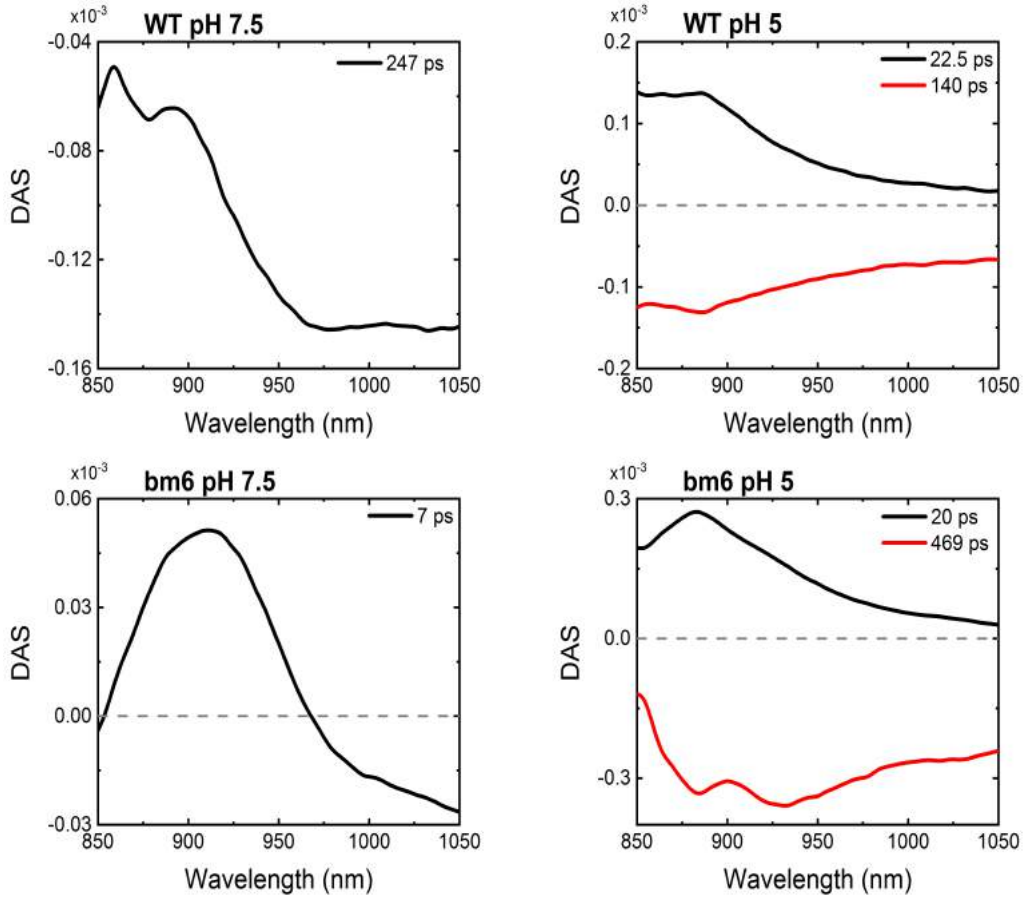

Figure 4.19: NIR Decay-associated spectra of the time constants found after global analysis.

We thus assign these time constants to a biexponential buildup of the carotenoid radical cation happening in the first hundreds of picoseconds (τ_1≈10-30 ps, τ_2≈100-500 ps). These results match reasonably well with the first two time constants found during the visible global analysis and assigned to a Car GSB signal (see table 4.3). Therefore, we can conclude that lutein plays a key role in ^{1}Chl* de-excitation. A pH-dependent charge transfer from the lutein to the excited chlorophyll constitutes the main quenching mechanism in both the LHCSR3 wild type and the bm6 mutant.

4.2 Discussion

In the previous chapter, we conclude that the main quenching mechanisms in the LHCSR3 protein of wild type *C. Reinhardtii* were the Car-Chl charge transfer, a non radiative protein-protein interaction and to a lesser extent, a ^{1}Chl*→Car S_1 energy transfer.

Here we report the case of a LHCSR3 mutant in which all the acid groups present in the C-terminus are substituted by bm6, a pH insensitive group. Previous works also explored the possibility of a pH insensitive LHCSR3 mutant either by subtraction[117] or substitution[77] of the C-terminus acid groups. After time-resolved fluorescence measurements, the authors did not see any significant differences between the overall lifetimes of the mutants at different pH. In our case, however, we observe an effect of the pH in the overall lifetime of both LHCSR3 WT and its bm6 mutant (figures 4.12 and 4.18 (right), respectively) as we see a clear quenching of the protein kinetics the lower the pH is. Also, we observed that the bm6 mutant showed a longer lifetime than the WT, regardless the pH value considered.

Regarding the quenching mechanisms of ^{1}Chl*, we saw huge similarities in the Chl-Car interactions between the WT and the bm6 mutant as we see similar spectra (figures 4.8 and 4.18) and kinetics (figures 4.13, 4.14 and 4.15 (right) and 4.19 (right)) both in the visible and the NIR. Furthermore, we did not observe the ^{1}Chl* → Car S_1 transition as no Car $S_1 \rightarrow S_n$ is observed in the 530-580 nm region. Due to carotenoid S_1 state short lived nature, it is not easy to identify if the carotenoid $S_1 \rightarrow S_n$ transition is happening or not, so we cannot exclude ^{1}Chl* → Car S_1 energy transfer as a possible quenching mechanism.

Finally, NIR TA studies revealed the formation of a lutein radical cation in all cases (with a predominant formation at low pH) that agrees with previous works performed on a similar protein, LHCSR1.[74] No kinetic differences are appreciated between the mutant and the wild type.

pH itself can cause aggregation[121] and thus it could explain the observed quenching. In fact, we saw in figure 4.10 that there is a strong pump scattering at pH 5 for both WT and mutant bm6. Even so, protein aggregation cannot explain why at pH 7.5, where the pump scattering is similar for both samples, bm6 lifetime is longer than the WT one. Therefore, there must be a carotenoid-free pathway that explains this lifetime difference.

A longer chlorophyll lifetime can be explained considering a non-aggregation related Chl-Chl interaction which is present both in the wild type and the bm6 mutant proteins. In this sense, we can hypothesize that this Chl-Chl interaction is stronger in the wild type than in the bm6 mutant and thus, the lifetime of the bm6 mutant is longer than the lifetime of the wild type.

To sum up, in this work we have studied the effects of C-terminal acid group suppression on *C. Reinhardtii* LHCSR3 at different pH values. In all cases, we found the formation of a lutein radical cation via Car-Chl charge transfer as the main quenching mechanism. However, mutant protein bm6 seems to manifest a Chl-Chl interaction that we cannot detect with the shown techniques and provokes an increment of the Chl bm6 mutant lifetime.

Bibliography

[1] Anastasios Melis. Solar energy conversion efficiencies in photosynthesis: Minimizing the chlorophyll antennae to maximize efficiency. *Plant Science*, 177(4):272–280, 2009.

[2] Z. Dubinsky, T. Berner, and S. Aaronson. Potential of large-scale algal culture for biomass and lipid production in arid lands. *Biotechnol. Bioeng. Symp.; (United States)*, 8, 1 1978.

[3] Ami Ben-Amotz and Mordhay Avron. The biotechnology of cultivating the halotolerant algadunaliella. *Trends in Biotechnology*, 8:121–126, 1990.

[4] Yuan-Kun Lee. Commercial production of microalgae in the asia-pacific rim. *Journal of Applied Phycology*, 9(5):403–411, 1997.

[5] Iris Lewandowski, Jonathan M. O. Scurlock, Eva Lindvall, and Myrsini Christou. The development and current status of perennial rhizomatous grasses as energy crops in the us and europe. *Biomass and Bioenergy*, 25(4):335–361, 2003.

[6] Emily A. Heaton, Frank G. Dohleman, and Stephen P. Long. Meeting us biofuel goals with less land: the potential of miscanthus. *Global Change Biology*, 14(9):2000–2014, Sep 2008.

[7] M. R. Schmer, K. P. Vogel, R. B. Mitchell, and R. K. Perrin. Net energy of cellulosic ethanol from switchgrass. *Proceedings of the National Academy of Sciences*, 105(2):464, Jan 2008.

[8] C. U. Ugwu, H. Aoyagi, and H. Uchiyama. Photobioreactors for mass cultivation of algae. *Bioresource Technology*, 99(10):4021–4028, 2008.

[9] Yusuf Chisti. Biodiesel from microalgae. *Biotechnology Advances*, 25(3):294–306, 2007.

[10] Otto Pulz. Photobioreactors: production systems for phototrophic microorganisms. *Applied microbiology and biotechnology*, 57(3):287–293, 2001.

[11] Barbara Demmig-Adams, Gyozo Garab, William Adams III, and U Govindjee. *Non-photochemical quenching and energy dissipation in plants, algae and cyanobacteria*, volume 40. Springer, 2014.

[12] L. Staehelin. Chloroplast structure and supramolecular organization of photosynthetic membranes. *Enclopedia of Plant Physiology, Vol. 19, Photosynthesis III*, 01 1986.

[13] S. P. Robinson and D. A. Walker. *Photosynthesis*, chapter 5 - Photosynthetic Carbon Reduction Cycle, pages 193–236. Academic Press, 1981.

[14] R. Hill and F. Bendall. Function of the two cytochrome components in chloroplasts: A working hypothesis. *Nature*, 186(4719):136–137, 1960.

[15] Robert E. Blankenship and Roger C. Prince. Excited-state redox potentials and the z scheme of photosynthesis. *Trends in Biochemical Sciences*, 10(10):382–383, 1985.

[16] Eduard Hurt and Günter Hauska. A cytochrome f/b6 complex of five polypeptides with plastoquinol-plastocyanin-oxidoreductase activity from spinach chloroplasts. *European journal of biochemistry*, 117(3):591–599, 1981.

[17] Parag R. Chitnis. Photosystem i: Function and physiology. *Annual Review of Plant Physiology and Plant Molecular Biology*, 52(1):593–626, Jun 2001.

[18] David Knaff. *Ferredoxin and Ferredoxin-Dependent Enzymes*, volume 4, pages 333–361. Kluwer Academics, 01 2004.

[19] Jan Pieter Abrahams, Andrew G. W. Leslie, René Lutter, and John E. Walker. Structure at 2.8 â resolution of f1-atpase from bovine heart mitochondria. *Nature*, 370(6491):621–628, 1994.

[20] R. E. McCarty, Y. Evron, and E. A. Johnson. The chloroplast atp synthase: A rotary enzyme? *Annual Review of Plant Physiology and Plant Molecular Biology*, 51(1):83–109, Jun 2000.

[21] Daniel I. Arnon. Ferredoxin and photosynthesis. *Science*, 149(3691):1460–1470, 1965.

[22] James A. Bassham, Andrew A. Benson, and Melvin Calvin. The path of carbon in photosynthesis: Viii. the rôle of malic acid. *Journal of Biological Chemistry*, 185(2):781–787, Aug 1950.

[23] Robert J. Porra Wolfhart Rüdiger Hugo Scheer (eds.) Hugo Scheer (auth.), Bernhard Grimm. *Chlorophylls and Bacteriochlorophylls: Biochemistry, Biophysics, Functions and Applications*. Advances in Photosynthesis and Respiration 25. Springer Netherlands, 1 edition, 2006.

[24] Mercedes Rubio, Björn O. Roos, Luis Serrano-Andrés, and Manuela Merchán. Theoretical study of the electronic spectrum of magnesium-porphyrin. *The Journal of Chemical Physics*, 110(15):7202–7209, Apr 1999.

[25] Martin Gouterman. Spectra of porphyrins. *Journal of Molecular Spectroscopy*, 6:138–163, 1961.

[26] Zhi-Qiang You, Chao-Ping Hsu, and Graham R Fleming. Triplet-triplet energy-transfer coupling: Theory and calculation. *The Journal of chemical physics*, 124(4):044506, 2006.

[27] Christian Triantaphylidès, Markus Krischke, Frank Alfons Hoeberichts, Brigitte Ksas, Gabriele Gresser, Michel Havaux, Frank Van Breusegem, and Martin Johannes Mueller. Singlet oxygen is the major reactive oxygen species involved in photooxidative damage to plants. *Plant Physiology*, 148(2):960, Oct 2008.

[28] Zhenfeng Liu, Hanchi Yan, Kebin Wang, Tingyun Kuang, Jiping Zhang, Lulu Gui, Xiaomin An, and Wenrui Chang. Crystal structure of spinach major light-harvesting complex at 2.72 å resolution. *Nature*, 428(6980):287–292, 2004.

[29] Patrick Jordan, Petra Fromme, Horst Tobias Witt, Olaf Klukas, Wolfram Saenger, and Norbert Krauß. Three-dimensional structure of cyanobacterial photosystem i at 2.5 å resolution. *Nature*, 411(6840):909–917, 2001.

[30] Harald PAULSEN, Bärbel FINKENZELLER, and Nicola KÜHLEIN. Pigments induce folding of light-harvesting chlorophyll a/b-binding protein. *European journal of biochemistry*, 215(3):809–816, 1993.

[31] F Gerald Plumley and Gregory W Schmidt. Reconstitution of chlorophyll a/b light-harvesting complexes: Xanthophyll-dependent assembly and energy transfer. *Proceedings of the National Academy of Sciences*, 84(1):146–150, 1987.

[32] Claudiu C. Gradinaru, Ivo H. M. van Stokkum, Andy A. Pascal, Rienk van Grondelle, and Herbert van Amerongen. Identifying the pathways of energy transfer between carotenoids and chlorophylls in lhcii and cp29. a multicolor, femtosecond pump-probe study. *The Journal of Physical Chemistry B*, 104(39):9330–9342, Oct 2000.

[33] M Mimuro and T Katoh. Carotenoids in photosynthesis: absorption, transfer and dissipation of light energy. *Pure and Applied Chemistry*, 63(1):123–130, 1991.

[34] Michel Havaux and Krishna K Niyogi. The violaxanthin cycle protects plants from photooxidative damage by more than one mechanism. *Proceedings of the National Academy of Sciences*, 96(15):8762–8767, 1999.

[35] Junko Yabuzaki. Carotenoids database: structures, chemical fingerprints and distribution among organisms. *Database : the journal of biological databases and curation*, 2017(1):bax004, Jan 2017.

[36] Roberto BASSI, Bernard PINEAU, Paola DAINESE, and Jürgen MARQUARDT. Carotenoid-binding proteins of photosystem ii. *European Journal of Biochemistry*, 212(2):297–303, Mar 1993.

[37] Stefano Caffarri, Roberta Croce, Jacques Breton, and Roberto Bassi. The major antenna complex of photosystem ii has a xanthophyll binding site not involved in light harvesting. *Journal of Biological Chemistry*, 276(38):35924–35933, 2001.

[38] Alexander V Ruban, Pamela J Lee, Mark Wentworth, Andrew J Young, and Peter Horton. Determination of the stoichiometry and strength of binding of xanthophylls to the photosystem ii light harvesting complexes. *Journal of Biological Chemistry*, 274(15):10458–10465, 1999.

[39] Nancy E. Holt, Graham R. Fleming, and Krishna K. Niyogi. Toward an understanding of the mechanism of nonphotochemical quenching in green plants. *Biochemistry*, 43(26):8281–8289, Jul 2004.

[40] Krishna K. Niyogi. Photoprotection revisited: Genetic and molecular approaches. *Annual Review of Plant Physiology and Plant Molecular Biology*, 50(1):333–359, Jun 1999.

[41] Xiaochun Qin, Xiong Pi, Wenda Wang, Guangye Han, Lixia Zhu, Mingmei Liu, Linpeng Cheng, Jian-Ren Shen, Tingyun Kuang, and Sen-Fang Sui. Structure of a green algal photosystem i in complex with a large number of light-harvesting complex i subunits. *Nature Plants*, 5(3):263–272, 2019.

[42] Shin-Ichiro Ozawa, Till Bald, Takahito Onishi, Huidan Xue, Takunori Matsumura, Ryota Kubo, Hiroko Takahashi, Michael Hippler, and Yuichiro Takahashi. Configuration of ten light-harvesting chlorophyll a/b complex i subunits in chlamydomonas reinhardtii photosystem i. *Plant Physiology*, 178(2):583, Oct 2018.

[43] Alexander Melkozernov and Robert Blankenship. Structural and functional organization of the peripheral light-harvesting system in photosystem i. *Photosynthesis research*, 85:33–50, 02 2005.

[44] Roberta Croce and Herbert van Amerongen. Light-harvesting in photosystem i. *Photosynthesis Research*, 116(2):153–166, 2013.

[45] Robert C. Jennings, Giuseppe Zucchelli, Roberta Croce, and Flavio M. Garlaschi. The photochemical trapping rate from red spectral states in psi-lhci is determined by thermal activation of energy transfer to bulk chlorophylls. *Biochimica et Biophysica Acta (BBA) - Bioenergetics*, 1557:91–98, 2003.

[46] J. Philip Thornber, John C. Stewart, Mark W. C. Hatton, and J. Leggett Bailey. Studies on the nature of chloroplast lamellae. ii. chemical composition and further physical properties of two chlorophyll-protein complexes*. *Biochemistry*, 6(7):2006–2014, Jul 1967.

[47] Roberto Bassi, Dorianna Sandonà, and Roberta Croce. Novel aspects of chlorophyll a/b-binding proteins. *Physiologia Plantarum*, 100(4):769–779, Aug 1997.

[48] Xin Sheng, Akimasa Watanabe, Anjie Li, Eunchul Kim, Chihong Song, Kazuyoshi Murata, Danfeng Song, Jun Minagawa, and Zhenfeng Liu. Structural insight into light harvesting for photosystem ii in green algae. *Nature Plants*, 5(12):1320–1330, 2019.

[49] Athina Zouni, Horst-Tobias Witt, Jan Kern, Petra Fromme, Norbert Krauss, Wolfram Saenger, and Peter Orth. Crystal structure of photosystem ii from synechococcus elongatus at 3.8 å resolution. *Nature*, 409(6821):739–743, 2001.

[50] Laura Girolomoni, Paola Ferrante, Silvia Berteotti, Giovanni Giuliano, Roberto Bassi, and Matteo Ballottari. The function of lhcbm4/6/8 antenna proteins in chlamydomonas reinhardtii. *Journal of experimental botany*, 68(3):627–641, Jan 2017.

[51] Sabrina Grewe, Matteo Ballottari, Marcelo Alcocer, Cosimo D'Andrea, Olga Blifernez-Klassen, Ben Hankamer, Jan H. Mussgnug, Roberto Bassi, and Olaf Kruse. Light-harvesting complex protein lhcbm9 is critical for photosystem ii activity and hydrogen production in chlamydomonas reinhardtii. *The Plant Cell*, 26(4):1598, Apr 2014.

[52] Hiroko Takahashi, Masakazu Iwai, Yuichiro Takahashi, and Jun Minagawa. Identification of the mobile light-harvesting complex ii polypeptides for state transitions in chlamydomonas reinhardtii. *Proceedings of the National Academy of Sciences of the United States of America*, 103(2):477, Jan 2006.

[53] Hiroko Takahashi, Akira Okamuro, Jun Minagawa, and Yuichiro Takahashi. Biochemical characterization of photosystem i-associated light-harvesting complexes i and ii isolated from state 2 cells of chlamydomonas reinhardtii. *Plant and Cell Physiology*, 55(8):1437–1449, May 2014.

[54] Paola Ferrante, Matteo Ballottari, Giulia Bonente, Giovanni Giuliano, and Roberto Bassi. Lhcbm1 and lhcbm2/7 polypeptides, components of major lhcii complex, have distinct functional roles in photosynthetic antenna system of chlamydomonas reinhardtii. *The Journal of biological chemistry*, 287(20):16276–16288, May 2012.

[55] Dafna Elrad, Krishna K. Niyogi, and Arthur R. Grossman. A major light-harvesting polypeptide of photosystem ii functions in thermal dissipation. *The Plant Cell*, 14(8):1801, Aug 2002.

[56] Ryutaro Tokutsu, Nobuyasu Kato, Khanh Huy Bui, Takashi Ishikawa, and Jun Minagawa. Revisiting the supramolecular organization of photosystem ii in chlamydomonas reinhardtii. *The Journal of biological chemistry*, 287(37):31574–31581, Sep 2012.

[57] Bartlomiej Drop, Mariam Webber-Birungi, Sathish K. N. Yadav, Alicja Filipowicz-Szymanska, Fabrizia Fusetti, Egbert J. Boekema, and Roberta Croce. Light-harvesting complex ii (lhcii) and its supramolecular organization in chlamydomonas reinhardtii. *Biochimica et Biophysica Acta (BBA) - Bioenergetics*, 1837(1):63–72, 2014.

[58] Eva-Mari Aro, Ivar Virgin, and Bertil Andersson. Photoinhibition of photosystem ii. inactivation, protein damage and turnover. *Biochimica et Biophysica Acta (BBA) - Bioenergetics*, 1143(2):113–134, 1993.

[59] Éva Hideg, Tamás Kálai, Kálmán Hideg, and Imre Vass. Photoinhibition of photosynthesis in vivo results in singlet oxygen production detection via nitroxide-induced fluorescence quenching in broad bean leaves. *Biochemistry*, 37(33):11405–11411, Aug 1998.

[60] Stephen B. Powles and Olle Björkman. Photoinhibition of photosynthesis: effect on chlorophyll fluorescence at 77k in intact leaves and in chloroplast membranes of nerium oleander. *Planta*, 156(2):97–107, 1982.

[61] G. H. Krause and E. Weis. Chlorophyll fluorescence and photosynthesis: The basics. *Annual Review of Plant Physiology and Plant Molecular Biology*, 42(1):313–349, Jun 1991.

[62] Christine H Foyer and Jeremy Harbinson. Relationships between antioxidant metabolism and carotenoids in the regulation of photosynthesis. In *The photochemistry of carotenoids*, pages 305–325. Springer, 1999.

[63] E. Formaggio, G. Cinque, and R. Bassi. Functional architecture of the major light-harvesting complex from higher plants. *Journal of molecular biology*, 314(5):1157–1166, 2001.

[64] Florence Tardy and Michel Havaux. Photosynthesis, chlorophyll fluorescence, light-harvesting system and photoinhibition resistance of a zeaxanthindashaccumulating mutant of arabidopsis thaliana. *Journal of Photochemistry and Photobiology B: Biology*, 34(1):87–94, 1996.

[65] J.-M. Briantais, C. Vernotte, M. Picaud, and G. H. Krause. A quantitative study of the slow decline of chlorophyll a fluorescence in isolated chloroplasts. *Biochimica et Biophysica Acta (BBA) - Bioenergetics*, 548(1), 1979.

[66] John F. Allen. Protein phosphorylation in regulation of photosynthesis. *Biochimica et Biophysica Acta (BBA) - Bioenergetics*, 1098(3):275–335, 1992.

[67] Giovanni Finazzi, Giles N. Johnson, Luca Dall'Osto, Francesca Zito, Giulia Bonente, Roberto Bassi, and Francis-André Wollman. Nonphotochemical quenching of chlorophyll fluorescence in chlamydomonas reinhardtii. *Biochemistry*, 45(5):1490–1498, Feb 2006.

[68] Maxim Y. Gorbunov, Zbigniew S. Kolber, Michael P. Lesser, and Paul G. Falkowski. Photosynthesis and photoprotection in symbiotic corals. *Limnology and Oceanography*, 46(1):75–85, Jan 2001.

[69] Graham Peers, Thuy B. Truong, Elisabeth Ostendorf, Andreas Busch, Dafna Elrad, Arthur R. Grossman, Michael Hippler, and Krishna K. Niyogi. An ancient light-harvesting protein is critical for the regulation of algal photosynthesis. *Nature*, 462(7272):518–521, 2009.

[70] Manuela Nilkens, Eugen Kress, Petar Lambrev, Yuliya Miloslavina, Marc Müller, Alfred R. Holzwarth, and Peter Jahns. Identification of a slowly inducible zeaxanthin-dependent component of non-photochemical quenching of chlorophyll fluorescence generated under steady-state conditions in arabidopsis. *Biochimica et Biophysica Acta (BBA) - Bioenergetics*, 1797(4):466–475, 2010.

[71] A. S. Verhoeven, W. W. Adams, and B. Demmig-Adams. Two forms of sustained xanthophyll cycle-dependent energy dissipation in overwintering euonymus kiautschovicus. *Plant, Cell & Environment*, 21(9):893–903, Sep 1998.

[72] Govindjee Papageorgiou, George C. Energy dissipation and photoinhibition: a continuum of photoprotection. In *Photoprotection, photoinhibition, gene regulation, and environment*, pages 1–44. Springer, 2008.

[73] Koh Seok-Chan Cohu Christopher M. Muller Onno Adams III William W Demmig-Adams, Barbara and Jared J Stewart. Non-photochemical fluorescence quenching in contrasting plant species and environments. In *Non-Photochemical Quenching and Energy Dissipation in Plants, Algae and Cyanobacteria*, pages 531–550. Springer, 2014.

[74] Alberta Pinnola, Matteo Ballottari, Ilaria Bargigia, Marcelo Alcocer, Cosimo D'Andrea, Giulio Cerullo, and Roberto Bassi. Functional modulation of lhcsr1 protein from physcomitrella patens by zeaxanthin binding and low ph. *Scientific Reports*, 7(1):11158, 2017.

[75] Xuepeng Wei, Xiaodong Su, Peng Cao, Xiuying Liu, Wenrui Chang, Mei Li, Xinzheng Zhang, and Zhenfeng Liu. Structure of spinach photosystem ii-lhcii supercomplex at 3.2 å resolution. *Nature*, 534(7605):69–74, 2016.

[76] Matteo Ballottari, Thuy B Truong, Eleonora De Re, Erika Erickson, Giulio R Stella, Graham R Fleming, Roberto Bassi, and Krishna K Niyogi. Identification of ph-sensing sites in the light harvesting complex stress-related 3 protein essential for triggering non-photochemical quenching in chlamydomonas reinhardtii. *Journal of Biological Chemistry*, 291(14):7334–7346, 2016.

[77] Nicoletta Liguori, Laura M. Roy, Milena Opacic, Grégory Durand, and Roberta Croce. Regulation of light harvesting in the green alga chlamydomonas reinhardtii:

The c-terminus of lhcsr is the knob of a dimmer switch. *Journal of the American Chemical Society*, 135(49):18339–18342, Dec 2013.

[78] Ryutaro Tokutsu and Jun Minagawa. Energy-dissipative supercomplex of photosystem ii associated with lhcsr3 in chlamydomonas reinhardtii. *Proceedings of the National Academy of Sciences of the United States of America*, 110(24):10016–10021, Jun 2013.

[79] Albert Einstein. Zur quantentheorie der strahlung. *Phys. Z.*, 18:121–128, 1917.

[80] Goro Nishimura and Mamoru Tamura. Simple setup for nanosecond time-resolved spectroscopic measurements by a digital storage oscilloscope. *Physics in medicine and biology*, 48:N283–90, Dec 2003.

[81] Desmond O'Connor. *Time-correlated single photon counting*. Academic Press, 2012.

[82] Wolfgang Becker. *Advanced time-correlated single photon counting techniques*, volume 81. Springer Science & Business Media, 2005.

[83] DJ Bradley, B Liddy, and WE Sleat. Direct linear measurement of ultrashort light pulses with a picosecond streak camera. *Optics Communications*, 2(8):391–395, 1971.

[84] M Ya Schelev, MC Richardson, and AJ Alcock. Image-converter streak camera with picosecond resolution. *Applied Physics Letters*, 18(8):354–357, 1971.

[85] David F Underwood, Tadd Kippeny, and Sandra J Rosenthal. Ultrafast carrier dynamics in cdse nanocrystals determined by femtosecond fluorescence upconversion spectroscopy. *The Journal of Physical Chemistry B*, 105(2):436–443, 2001.

[86] George-Na3240 Porter. Flash photolysis and spectroscopy. a new method for the study of free radical reactions. *Proceedings of the Royal Society of London. Series A. Mathematical and Physical Sciences*, 200(1061):284–300, 1950.

[87] George Porter and Mc R Topp. Nanosecond flash photolysis. *Proceedings of the Royal Society of London. A. Mathematical and Physical Sciences*, 315(1521):163–184, 1970.

[88] PA Van Hal, RAJ Janssen, Guglielmo Lanzani, G Cerullo, Margherita Zavelani-Rossi, and Sandro De Silvestri. Full temporal resolution of the two-step photoinduced energy–electron transfer in a fullerene–oligothiophene–fullerene triad using sub-10 fs pump–probe spectroscopy. *Chemical physics letters*, 345(1-2):33–38, 2001.

[89] Cristian Manzoni, Dario Polli, and Giulio Cerullo. Two-color pump-probe system broadly tunable over the visible and the near infrared with sub-30 fs temporal resolution. *Review of scientific instruments*, 77(2):023103, 2006.

[90] James Eells. A setting for global analysis. *Bull. Amer. Math. Soc.*, 72 ER(5):751–807, 1966.

[91] S. Smale. What is global analysis? *The American Mathematical Monthly*, 76(1):4–9, Jan 1969.

[92] Joris Snellenburg, Sergey Laptenok, Ralf Seger, Katharine Mullen, and Ivo van Stokkum. Glotaran: A java-based graphical user interface for the r package timp. *Journal of Statistical Software, Articles*, 49(3), 2012.

[93] Marc G. Müller, Petar Lambrev, Michael Reus, Emilie Wientjes, Roberta Croce, and Alfred R. Holzwarth. Singlet energy dissipation in the photosystem ii light-harvesting complex does not involve energy transfer to carotenoids. *ChemPhysChem*, 11(6):1289–1296, 2010.

[94] Md Wahadoszamen, Iris Margalit, Anjue Ara, Rienk van Grondelle, and Dror Noy. The role of charge-transfer states in energy transfer and dissipation within natural and artificial bacteriochlorophyll proteins. *Nature Communications*, 5, 2014.

[95] Tomás Polívka and Harry A. Frank. Molecular factors controlling photosynthetic light harvesting by carotenoids. *Accounts of Chemical Research*, 43(8):1125–1134, Aug 2010.

[96] Harry A. Frank, Agnes Cua, Veeradej Chynwat, Andrew Young, David Gosztola, and Michael R. Wasielewski. Photophysics of the carotenoids associated with the xanthophyll cycle in photosynthesis. *Photosynthesis Research*, 41(3):389–395, 1994.

[97] A.V. Ruban, R. Berera, C. Ilioaia, I.H.M. van Stokkum, J.T.M. Kennis, A.A. Pascal, H. van Amerongen, B. Robert, P. Horton, and R. van Grondelle. Identification of a mechanism of photoprotective energy dissipation in higher plants. *Nature*, 450(7169):575–578, 2007.

[98] H. Staleva and M. et al. Komenda, J.and Shukla. Mechanism of photoprotection in the cyanobacterial ancestor of plant antenna proteins. *Nat Chem Biol*, 11:287–291, 2015.

[99] Tomasz Niedzwiedzki, Dariusz M.and Tronina, Haijun Liu, Hristina Staleva, Josef Komenda, Roman Sobotka, Robert E. Blankenship, and Tomás Polívka. Carotenoid-induced non-photochemical quenching in the cyanobacterial chlorophyll synthase-hlic/d complex. *Biochimica et Biophysica Acta (BBA) - Bioenergetics*, 1857(9):1430–1439, 2016.

[100] N. Liguori, P. Xu, I. H. M. van Stokkum, B. van Oort, Y. Lu, D. Karcher, R. Bock, and R. Croce. Different carotenoid conformations have distinct functions in light-harvesting regulation in plants. *Nat Commun*, 1994(8), 2017.

[101] Nancy E. Holt, Donatas Zigmantas, Leonas Valkunas, Xiao-Ping Li, Krishna K. Niyogi, and Graham R. Fleming. Carotenoid cation formation and the regulation of photosynthetic light harvesting. *Science*, 307(5708):433, Jan 2005.

[102] Thomas J. Avenson, Tae Kyu Ahn, Donatas Zigmantas, Krishna K. Niyogi, Zhirong Li, Matteo Ballottari, Roberto Bassi, and Graham R. Fleming. Zeaxanthin radical cation formation in minor light-harvesting complexes of higher plant antenna. *Journal of Biological Chemistry*, pages 3550–3558, 2 2008.

[103] Stefan Bode, Claudia C Quentmeier, Pen-Nan Liao, Nour Hafi, Tiago Barros, Laura Wilk, Florian Bittner, and Peter J Walla. On the regulation of photosynthesis by excitonic interactions between carotenoids and chlorophylls. *Proceedings of the National Academy of Sciences*, 106(30):12311–12316, 2009.

[104] Alberta Pinnola, Hristina Staleva-Musto, Stefano Capaldi, Matteo Ballottari, Roberto Bassi, and Tomáš Polívka. Electron transfer between carotenoid and chlorophyll contributes to quenching in the lhcsr1 protein from physcomitrella patens. *Biochimica et Biophysica Acta (BBA)-Bioenergetics*, 1857(12):1870–1878, 2016.

[105] Soomin Park, Collin J Steen, Dagmar Lyska, Alexandra L Fischer, Benjamin Endelman, Masakazu Iwai, Krishna K Niyogi, and Graham R Fleming. Chlorophyll–carotenoid excitation energy transfer and charge transfer in nannochloropsis oceanica for the regulation of photosynthesis. *Proceedings of the National Academy of Sciences*, 116(9):3385–3390, 2019.

[106] Giulia Bonente, Matteo Ballottari, Thuy B Truong, Tomas Morosinotto, Tae K Ahn, Graham R Fleming, Krishna K Niyogi, and Roberto Bassi. Analysis of lhcsr3, a protein essential for feedback de-excitation in the green alga chlamydomonas reinhardtii. *PLoS biology*, 9(1):e1000577, 2011.

[107] Kapil Amarnath, Julia Zaks, Samuel D Park, Krishna K Niyogi, and Graham R Fleming. Fluorescence lifetime snapshots reveal two rapidly reversible mechanisms of photoprotection in live cells of chlamydomonas reinhardtii. *Proceedings of the National Academy of Sciences*, 109(22):8405–8410, 2012.

[108] Eunchul Kim, Seiji Akimoto, Ryutaro Tokutsu, Makio Yokono, and Jun Minagawa. Fluorescence lifetime analyses reveal how the high light–responsive protein lhcsr3 transforms psii light-harvesting complexes into an energy-dissipative state. *Journal of Biological Chemistry*, 292(46):18951–18960, 2017.

[109] Elisabetta Giuffra, Daniela Cugini, Roberta Croce, and Roberto Bassi. Reconstitution and pigment-binding properties of recombinant cp29. *European journal of biochemistry*, 238(1):112–120, 1996.

[110] Bart van Oort, Laura M. Roy, Pengqi Xu, Yinghong Lu, Daniel Karcher, Ralph Bock, and Roberta Croce. Revisiting the role of xanthophylls in nonphotochemical quenching. *The Journal of Physical Chemistry Letters*, 9(2):346–352, Jan 2018.

[111] Tomás Polívka and Villy Sundström. Ultrafast dynamics of carotenoid excited states-from solution to natural and artificial systems. *Chemical Reviews*, 104(4):2021–2072, Apr 2004.

[112] J. L. Herek, M. Wendling, Z. He, T. Polívka, G. Garcia-Asua, R. J. Cogdell, C. N. Hunter, R. van Grondelle, V. Sundström, and T. Pullerits. Ultrafast carotenoid band shifts: Experiment and theory. *The Journal of Physical Chemistry B*, 108(29):10398–10403, Jul 2004.

[113] Elisabet Romero, Ivo H. M. van Stokkum, Jan P. Dekker, and Rienk van Grondelle. Ultrafast carotenoid band shifts correlated with chlz excited states in the photosystem ii reaction center: are the carotenoids involved in energy transfer? *Physical Chemistry Chemical Physics*, 13(13):5573–5575, 2011.

[114] Tomás Polívka, Tõnu Pullerits, Harry A. Frank, Richard J. Cogdell, and Villy Sundström. Ultrafast formation of a carotenoid radical in lh2 antenna complexes of purple bacteria. *The Journal of Physical Chemistry B*, 108(39):15398–15407, Sep 2004.

[115] Sergiu Amarie, Jörg Standfuss, Tiago Barros, Werner Kühlbrandt, Andreas Dreuw, and Josef Wachtveitl. Carotenoid radical cations as a probe for the molecular mechanism of nonphotochemical quenching in oxygenic photosynthesis. *The Journal of Physical Chemistry B*, 111(13):3481–3487, Apr 2007.

[116] Christoph-Peter Holleboom, Daniel Alexander Gacek, Pen-Nan Liao, Marco Negretti, Roberta Croce, and Peter Jomo Walla. Carotenoid-chlorophyll coupling and fluorescence quenching in aggregated minor psii proteins cp24 and cp29. *Photosynthesis Research*, 124(2):171–180, 2015.

[117] Matteo Ballottari, Julien Girardon, Nico Betterle, Tomas Morosinotto, and Roberto Bassi. Identification of the chromophores involved in aggregation-dependent energy quenching of the monomeric photosystem ii antenna protein lhcb5. *The Journal of biological chemistry*, 285(36):28309–28321, Sep 2010.

[118] Yuliya Miloslavina, Antje Wehner, Petar H. Lambrev, Emilie Wientjes, Michael Reus, Gyozo Garab, Roberta Croce, and Alfred R. Holzwarth. Far-red fluorescence: A direct spectroscopic marker for lhcii oligomer formation in non-photochemical quenching. *FEBS Letters*, 582(25-26):3625–3631, Oct 2008.

[119] Emine Dinc, Lijin Tian, Laura M. Roy, Robyn Roth, Ursula Goodenough, and Roberta Croce. Lhcsr1 induces a fast and reversible ph-dependent fluorescence quenching in lhcii in chlamydomonas reinhardtii cells. *Proceedings of the National Academy of Sciences of the United States of America*, 113(27):7673–7678, Jul 2016.

[120] Milena Mozzo, Luca Dall'Osto, Rainer Hienerwadel, Roberto Bassi, and Roberta Croce. Photoprotection in the antenna complexes of photosystem ii role of individual xanthophylls in chlorophyll triplet quenching. *Journal of Biological Chemistry*, 283(10):6184–6192, 2008.

[121] Gabriel de la Cruz Valbuena, Franco Valduga de Almeida Camargo, Rocio Borrego-Varillas, Federico Perozeni, Cosimo D'Andrea, Matteo Ballottari, and Giulio Cerullo. Molecular mechanisms of non-photochemical quenching in the lhcsr3 protein of chlamydomonas reinhardtii. *The Journal of Physical Chemistry Letters*, 10, May 2019.